Transparent Conductive Oxide (TCO) bilayer designs for thin film Si-based solar cells

Anastasios Dimitriadis

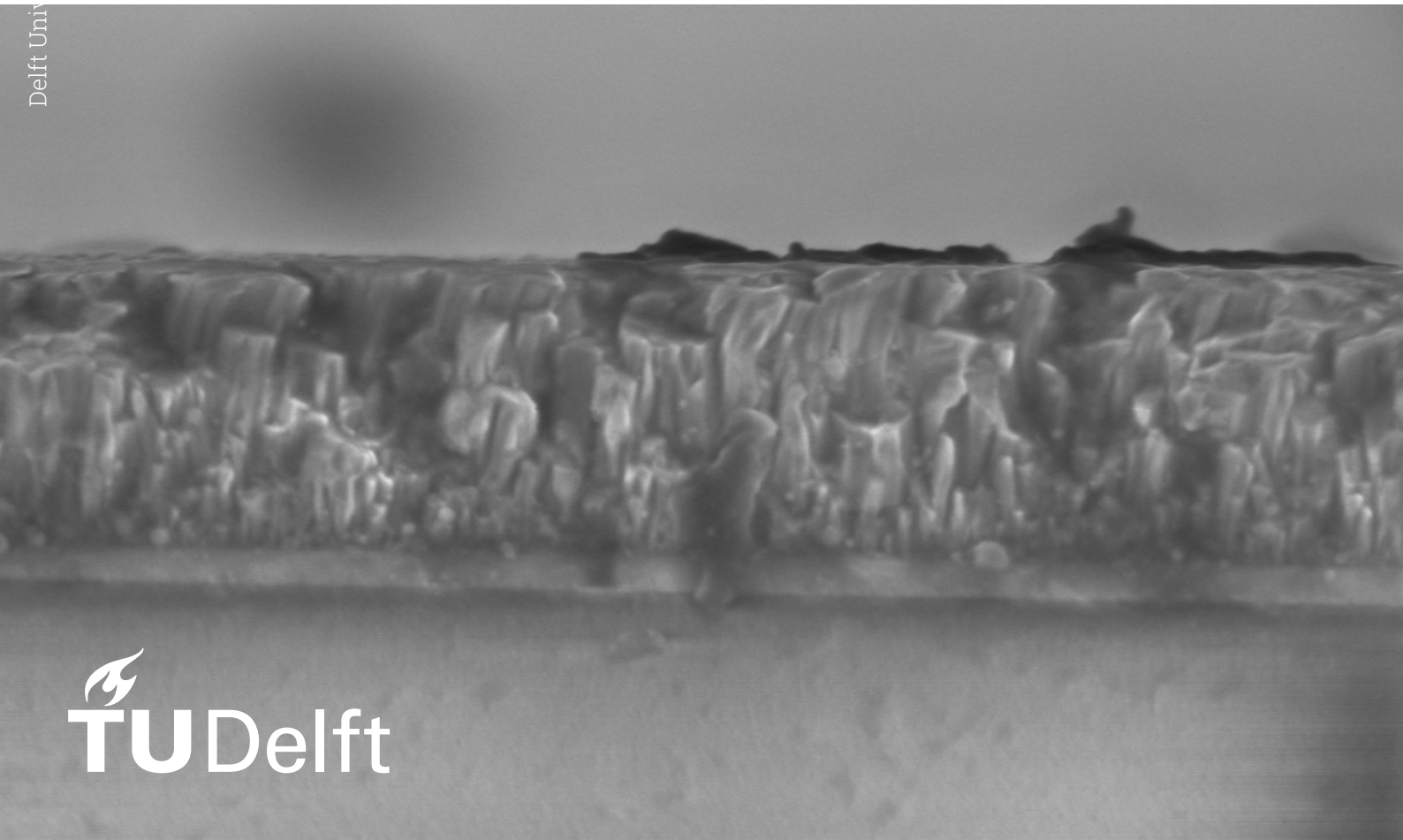

TU Delft

Transparent Conductive Oxide (TCO) bilayer designs for thin film Si-based solar cells

by

Anastasios Dimitriadis

to obtain the degree of Master of Science

at the Delft University of Technology,

to be defended publicly on Monday September 30th, 2024 at 15:30 AM.

Faculty: Electrical Engineering, Mathematics and Computer Science, Delft

Student Number:	5853842	
Thesis committee:	Prof.dr.ir. A.(Arno) H.M.Smets	Professor - PVMD group
	Dr.ir. R. (Rudi) Santbergen	Assistant Professor - PVMD group
	Dr.ir. F. (Fabio) Munoz	Assistant Professor – High Voltage
Daily supervisors:	F. (Federica) Saitta	
	Dr. P.(Paula) Perez Rodriguez	
Project Duration:	December 10, 2023 - September 30, 2024	

TU Delft

Abstract

Photovoltaic solar energy is one of the most powerful renewable sources, playing a key role in transitioning the global energy sector from fossil fuels to zero-carbon emissions. The second generation of photovoltaic technology, such as thin-film silicon-based devices, offers potential for significant performance improvements. Among the layers that can be optimized, the front contact, composed of transparent conductive oxide (TCO) materials, is crucial. As the first layer to encounter incident light, TCO has to meet the high transparency requirement. Additionally, it has to offer high conductivity to transport carriers from the absorber layers to the metal contact. However, there is a trade-off between transparency and conductivity—improving one often compromises the other. Instead of seeking a single layer that balances these properties, an alternative approach involves the use of bilayers. Bilayers consist of two TCOs: one optimized for transparency and the other for conductivity.

This thesis study focus on the design of bilayer configurations using two distinct materials, one optimized for transparency and the other for conductivity. Those designs aim to overcome the limitations of single-layer TCOs and achieve superior performance. Indium Cerium Oxide (ICO) and Hydrogenated Indium Oxide (IOH) were selected as conductive materials due to their excellent electrical properties, while intrinsic Zinc Oxide (i-ZnO), known for its high transparency, was used as the transparent layer. Tin Oxide (SnOx), a promising alternative, was also explored and integrated into bilayer configurations. All depositions were performed using Radio Frequency magnetron sputtering.

The design process began by optimizing deposition conditions for each material. For ICO, power and process pressure were the examined variables, while for IOH, power and partial water pressure were studied. For SnOx, power and gas composition during deposition were evaluated.

After determining the optimal deposition parameters based on opto-electrical properties examination, the following bilayer combinations were produced: IOH/i-ZnO, ICO/i-ZnO, and IOH/SnOx. In these bilayer depositions, the conductive material (IOH or ICO) was deposited first, followed by the transparent layer (i-ZnO or SnOx).

The bilayer configurations exhibited superior opto-electrical properties compared to single layers. Specifically, the bilayers maintained high transparency with carrier densities of 1-2$\times 10^{19}$ cm^{-3}, minimizing parasitic absorption in the near-infrared region of the solar spectrum. Mobility values of 50-60 cm^2/Vs ensured excellent lateral conductivity. These results demonstrated that bilayers preserve the best attribute of each composed material and the combination is a superior option for silicon-based solar cells.

The initial depositions were conducted on flat glass substrates. Since silicon-based solar cells use textured substrates, the same bilayer configurations were also deposited on textured surfaces. The results showed that mobility values remained consistent at 50-60 cm^2/Vs, though free carrier density was increased to 7-9$\times 10^{19}$ cm^{-3} . However, those bilayers still outperformed single layers, and with further optimization, the issue of reduced free carrier density can be addressed.

Acknowledgements

”Success is not final, failure is not fatal: It is the courage to continue that counts.”
— Winston Churchill

When I first came to the Netherlands to start my MSc at TU Delft, I never imagined that I would achieve what I have. It has been a challenging journey for me but every obstacle in the way has pushed me beyond my limits and helped me discover new aspects of myself. Each experience has shaped who I am today, and I am truly proud of the person I have become. For all these, I have to thank wholeheartedly the people in my life that were always there for me and helped me through the way.

Federica Saitta, you were the person that helped me the most throughout this project. Working with you truly helped me develop myself and I will always be grateful for that. Your willingness to share your knowledge and your patience, even when I made mistakes, are unique qualities, and I deeply appreciate them.

Dr. Paula Perez Rodriguez, whenever I needed help, you were always there to listen and guide me through the problem. Your calmness and the way you helped me believe in myself gave me an incredible boost. I am truly grateful for that, and I hope I can be act like that in my future.

Dr. Govind Padmakumar, you were one of the kindest people I have met this year. Your help, even when you were in a rush, was so valuable, and I cannot express my gratitude enough. From my part I hope to have contributed to even a fraction of your research.

Prof. dr. ir. Arno Smets, your theories and your knowledge thought me so many things in this project. I am grateful for the opportunity you gave me to work in the group and for all your support during my research. From my part I hope to have contributed to even a fraction of your research.

To all my friends, the time spent with you was one of the most valuable parts of this journey. To my friends from my hometown, even with the distance between us, we shared unforgettable memories. To the new friends I made these years, our memorable Mondays and the cherished moments we spent together were exactly what I was hoping to find when I first arrived here.

To my mother and my father, none of this would have been possible without you. You have been there since day one. Your unconditional support has always helped me keep going. I hope I have made you feel as proud as I am of you.

To Maria-Dafni, every time you stood by me and help me continue. During all those years, we shared all the possible emotions and all of them made me become a better person.

Lastly, to my brother. You are special. Together we shared all my achievements, concerns, and challenges. Thank you for being there every step of the way.

Anastasios Dimitriadis
Delft, September 2024

Contents

List of Figures

List of Tables

1

Introduction

1.1. Solar Energy

One of the most significant and pressing challenges in our planet is global warming. Human activities are estimated to have caused around 1.0°C of global warming above pre-industrial levels and it is likely to reach 1.5°C between 2030 and 2050 if it continues to increase at the current rate [1]. Green House Gas emissions are responsible for this climate change, with fossil fuels contributing more than 60% as it can be seen in Figure 1.1. There has been a continuous increase in Carbon emissions from energy combustion and industries since the industrialization in the mid-18th century [2].In order to try and mitigate the global mean surface temperature (GMST), different scenarios have been provided to reduce the greenhouse gas emissions. Each scenario stresses on the necessity of clean and renewable energy sources.

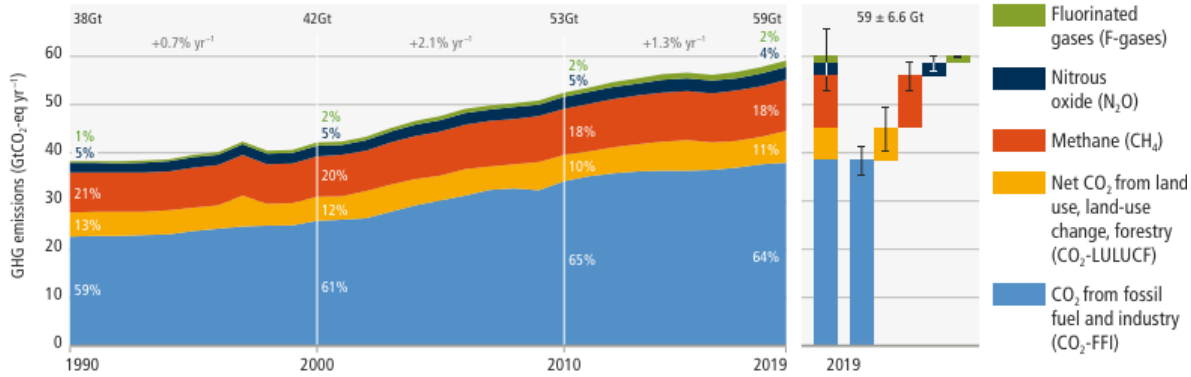

Figure 1.1: Man-made emissions provided by International Panel for Climate Change (IPCC) [1]

Solar energy is the most abundant renewable energy source in the planet and there are many ways of harnessing it [1]. Such methods are Concentrating Solar Power (CSP), Solar Heating and Cooling (SHC) and Photovoltaics (PV) [3].To take advantage of solar energy, it must first be converted into electrical energy using the photovoltaic effect. This effect describes the working principle of solar cells. Interconnected solar cells makes a PV module. Multiple PV modules make a solar panel suitable for diverse installations (rooftop, solar parks,etc) enabling large-scale generation of renewable electricity. This technology is rapidly evolving, especially the last decade reaching the contributions of other energy sources, like nuclear and wind as it can be also seen from the Figure 1.2

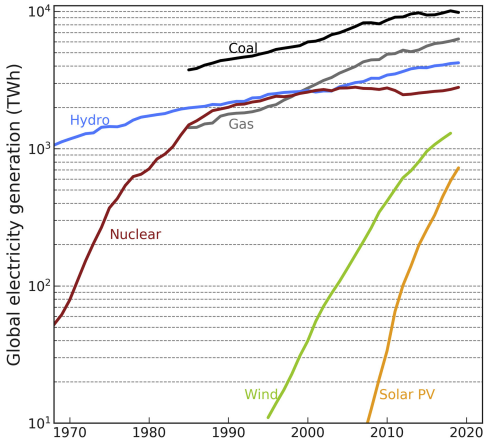

Figure 1.2: Different sources' contributions in total energy [4]

In 2022, solar photovoltaic (PV) generation increased by a record 270 TWh, representing a 26% growth, bringing total global solar PV generation to nearly 1300 TWh. This marks the largest absolute generation increase of any renewable energy source in 2022, surpassing wind for the first time [5]. This growth is particularly important because it aligns with the levels projected in the Net Zero Emissions by 2050 Scenario. However, to maintain this trend, annual capacity additions must nearly triple compared to 2022 levels. This acceleration is expected to further boost capacity growth in the coming years, leaving significant room for advancements across all photovoltaic technologies.

1.2. Research motivation

1.2.1. Thin film technology

Today, the world's solar market is dominated by crystalline silicon modules with a high market share, around 90% as reported by ISE [6], and high efficiencies of 26.81% [7]. However, their major drawbacks are the high production costs and the long payback time. Thus, new alternative technologies have been investigated, such as thin-film technology.

Figure 1.3: Hyet thin film power foil [8]

One of the main advantages of this technology is the potential thickness reduction, since the active layer of thin films is in the range of hundreds nanometers up to few micrometers. Requiring less material and being able to be deposited using low-cost processes, like sputtering or chemical vapor deposition (CVD), make them cost-effective [9]. Another key advantage of thin films is the flexibility. Thin film solar cells can be fabricated on flexible substrates, allowing integration into various surfaces, including curved surfaces and wearable devices. This means the efficient utilisation of the available area, leading to higher gains of electricity. Furthermore, PV modules based on c-Si solar cells are much heavier than the thin-film PV modules. Thus, thin-film modules are suitable for applications such as rooftops with

weight constraints. Adding to this, their flexibility made them suitable for installations onto uneven surfaces or facade installations. Examples like this can be seen in Figures 1.4 and 1.5.

Figure 1.4: Thin-film application on Vopak terminal [10]

Figure 1.5: Rooftop application [4]

In thin-film solar cell technology, some direct bandgap materials that are commonly used are amorphous silicon (a-Si), copper indium gallium selenide (CIGS), and cadmium telluride (CdTe). The current efficiency limits for these materials are 13.6% for α-Si [11], 22.1% for CdTe [12], and 22.9% for CIGS [13]. For comparison, a typical PV c-Si solar cell has an efficiency of 26.8% [14], making thin-film technology competitive with mainstream solar cells. Given these advancements, thin-film technology holds significant potential for further growth and optimization.

1.2.2. TCO Importance

Figure1.6 shows the cross-section structure of an a-Si:H/nc-Si:H tandem solar cell, in superstrate configuration. When light interacts with the solar cell, photons with an energy greater than the material's bandgap will have a certain chance to be absorbed within the material and will proceed to generate an electron-hole pair. These excited electron-holes pairs are separated by the electric field in the p-i-n junction, where electrons are directed to the n-layer and holes to the p-layer, generating electric current to power up electric devices.

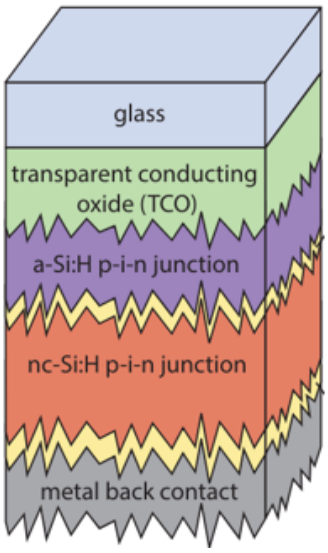

Figure 1.6: Cross-section of a solar cell [15]

A layer that is present in every solar cell configuration is the Transparent Conducting Oxide (TCO) layer, which acts as a window layer to the incoming sunlight. The key characteristic of TCO's is that it can combine optical transparency and electrical conductivity. For PV application, TCO's are used as front as a back reflector. At the front contact, the TCO should have a high transparency in order to allow maximum light to reach the active layer of the cell. Furthermore, TCO's should also exhibit high

electrical conductivity to efficiently transport the charge carriers, generated in the p-i-n junction, to the metal contact. Therefore, high conductivity is critically important to minimise electrical losses.

1.3. The goal of this report

Currently, indium tin oxide (ITO) is employed as front contact TCO, due to its favorable trade-off between optical and electrical requirements. However, meeting high conductivity and high transparency in one single TCO layer is challenging. Therefore, instead of seeking the material with the best balance, previous work has demonstrated the potential of TCOs bilayer structure as an alternative. In this approach, one layer meets the high conductivity and the another layer serves the optical purpose.

The research questions guiding this project are:

1) Which materials are the most competitive in terms of optical and electrical performance?

2) Can a bilayer configuration overcome the performance limitations of single layer TCOs?

3) Can these improvements be successfully transferred to a textured bilayer configuration?

To address these questions, the project begins by investigating and optimizing different individual materials to determine their peak performance. The bilayer approach involves combining two distinct TCO materials—one selected for its high transparency and the other for its superior conductivity. The aim is to surpass the opto-electrical performance of single-layer TCOs.

To enhance the light management for the solar device, textured glass substrates are commonly used. Thus, the next phase will involve transferring these bilayer configurations to textured glass, evaluating whether the improved opto-electrical properties observed on flat substrates are maintained when applied to textured glass.

1.4. Structure of the report

Chapter 2 will focus on the theoretical background of the optical and electrical properties of transparent conductive oxides (TCOs), exploring the inherent trade-offs between these properties. This discussion will help to clarify the limitations of TCOs.

Chapter 3 will present an in-depth review of the laboratory equipment used throughout the project, and the experimental methods.

Chapter 4 will provide a comprehensive analysis of the different TCO materials investigated in this project, detailing their opto-electrical properties as obtained from various experimental series.

Chapter 5 will introduce the bilayer configurations formed by combining the best-performing single layers from the previous chapter. Additionally, this chapter will examine the comparison between flat and textured glass substrates for bilayer configurations.

Chapter 6 will present the project's conclusions and will offer recommendations for future research, outlining potential improvements to the project.

2

Theory

2.1. Introduction in TCO

Transparent conducting oxide (TCO) materials are commonly implemented as front contact in the solar cell devices. Most of the existing TCO materials are n-type semiconductors. In n-type, defects, such as oxygen vacancies, and impurities donate electrons to the conduction band providing in this way charge carriers for the flow of electric current [16]. Indium oxide (In_2O_3), tin oxide (SnO_x), zinc oxide (ZnO), cadmium oxide (CdO), and gallium oxide (Ga_2O_3) are the most representative used materials.

Among these n-type oxides, CdO is one of the first investigated TCO, but due to the toxicity of Cd and the relatively narrow bandgap of 2.3 eV, its not used lately. Regarding Ga_2O_3 is extensively investigated in power electronics [17] but not yet in PV applications despite its large Eg-4.8 eV. SnO_x-, ZnO- and In_2O_3- based TCOs have have been largely investigated due to appropriate characteristics, namely optical bandgap, above 3 eV, and low resistivity, around or below 10^{-3} Ω cm [18].

2.2. Solar cell principle

The working principle of solar cells is based on the photovoltaic effect, which involves the generation of a potential difference at the junction of two distinct materials when exposed to electromagnetic radiation. This is related to the photoelectric effect, where light is absorbed by a material to emit electrons. Photons carry energy that is described by the following equation 2.1:

$$E = h\nu = \frac{hc}{\lambda} \tag{2.1}$$

where h is Panck's constant-6.63×10^{-34} m^2 kg/s, ν is the frequency of light, c is the speed of light and λ is the wavelength. When a semiconductor is exposed to light, an absorbed photon is able to excite an electron from the valence band to the conduction band. This will happen only if the incoming photon energy is enough to satisfy equation 2.2.

$$h\nu = E_f - E_i \tag{2.2}$$

where E_f is the higher energy level and E_i the initial energy level. When an electron is excited to the higher energy state, it leaves a void behind. This void called hole and it is a positively charged elementary particle.

The generation of the electron-hole pair when a photon is absorbed by a semiconductor is described in Figure 2.1. The energy difference between the two bands is called Energy bandgap (Eg).

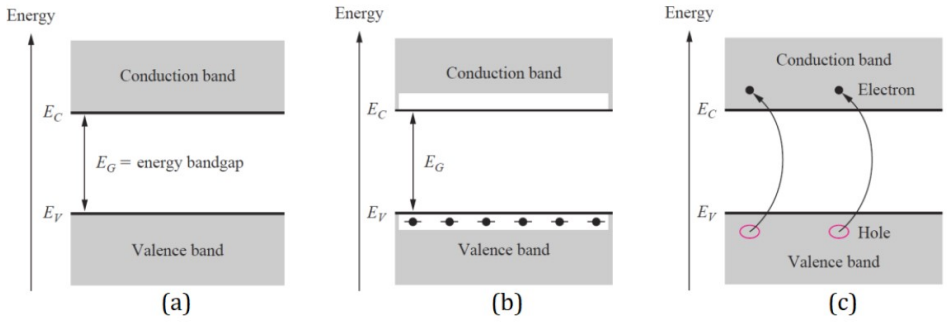

Figure 2.1: Energy band model for a semiconductor with bandgap Eg(a); Semiconductor at 0 K with filled valence band and empty conduction band(b); Electron-hole pair generation by excitation across energy bandgap (c)[19]

2.3. Energy Bandgap

Specifically for the energy bandgap, a distinction can be made between direct and indirect. The difference between the two can be easily explained by the use of the following diagrams in Figure 2.2.

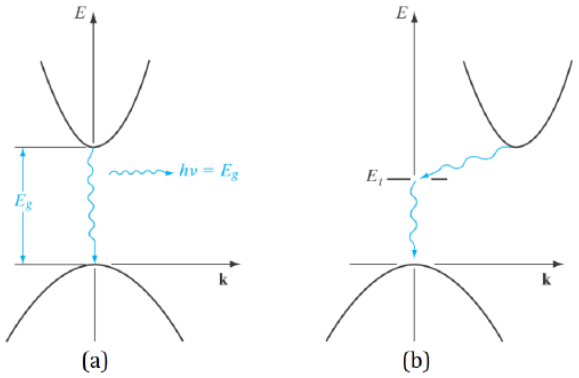

Figure 2.2: Direct bandgap (a) . Indirect bandgap (b). [20]

Vertical axis refers to the energy state, where the horizontal axis represents the charge carrier momentum. Figure 2.2a shows a direct bandgap, meaning that the maximum of the valence band and minimum of the conduction band are aligned with each other. For this case, the excitation of an electron from the valence band to the conduction band requires only the energy provided by the absorbed photon. Figure 2.2b shows an indirect bandgap where the maximum and minimum of the valence and conduction bands respectively are not aligned with each other. In this case, an electron requires not only the energy from the absorbed photon for the vertical movement but also a momentum transfer for the horizontal movement in order to be excited to the conduction band. For the momentum transfer that is required, vibrations of the crystal lattice are the ones that are responsible. These crystal lattice vibrations can be described both as waves or particles and are defined as phonons. Acquiring a phonon by the electron makes possible the change in momentum. Most of the materials used in this project are direct materials. The identification of the used materials is important for optical characterisation.

2.4. Optics

One of the main design rules for PV technologies is light management. Regarding optical interactions at interfaces, the nature of the interaction is determined by the relative size of the surface features compared to the wavelength of the incident light. Specifically, when the surface features are smaller than the light's wavelength, the interaction is referred to as macroscopic. When the surface features are significantly larger than the wavelength, the interaction is then referred as microscopic. In our case, macroscopic nature of the optical interaction is important and it is presented in the following Figure 2.3:

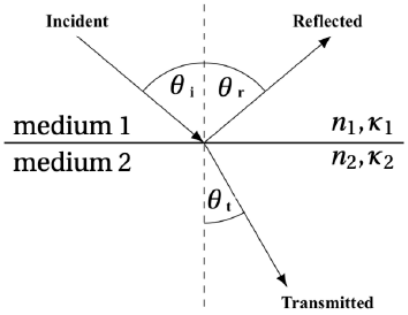

Figure 2.3: Interaction of light at interface [21]

When an electromagnetic wave, such as light, encounters the boundary between two different media, a percentage of the wave is reflected, while the remaining part is refracted into the second medium. According to the law of reflection, the light component that will bounce back, will go along a path that is created in such a way that the reflection angle is equal to that of the incidence angle as it can be seen in Figure 2.3.

Considering refraction, the interaction is described by using the Snell law [21] given by equation 2.3. It has to be mentioned that the refractive indices are considered to be characterized only by the real component, while the imaginary part is neglected since at the interface no absorption occurs, thus the imaginary part, which consists of the extinction coefficient κ,is not considered.

$$n_1 \sin\theta_i = n_2 \sin\theta_t \tag{2.3}$$

where n_1 and n_2 representing the refractive indices of the two media, θ_i and θ_t refer to the incident and the refraction angles of the light. Note that the angles are measured with respect to the normal to the surface at the point of incidence.

The intensities of the of the light components that are reflected (r) and transmitted (t) are provided by Fresnel equations, given by equations 2.4 and 2.5 respectively.

$$r_p = \frac{n_2\cos\theta_i - n_1\cos\theta_t}{n_2\cos\theta_i + n_1\cos\theta_t}, r_s = \frac{n_1\cos\theta_i - n_2\cos\theta_t}{n_1\cos\theta_i + n_2\cos\theta_t} \tag{2.4}$$

$$t_s = \frac{2n_1\cos\theta_i}{n_1\cos\theta_i + n_2\cos\theta_t}, t_p = \frac{2n_1\cos\theta_i}{n_2\cos\theta_i + n_1\cos\theta_t} \tag{2.5}$$

In those equations p indicates the component of light that is polarised along the path of propagation, where s indicates the polarised component that is normal to the path of propagation.

Following those equations, the total intensity of light that is reflected (R) and transmitted (T) are calculated by equations 2.6, 2.7 respectively.

$$R = \frac{1}{2}\left(r_s^2 + r_p^2\right) \tag{2.6}$$

$$T = 1 - R = \frac{n_2\cos\theta_t}{2n_1\cos\theta_i}\left(t_s^2 + t_p^2\right) \tag{2.7}$$

In all the previous equations, a special case has to be mentioned, the total internal reflection (TIR). Specifically, when light travels from an optically lighter medium to an optically denser medium, where n_1<n_2, there is a particular angle of incidence, called the critical angle, beyond which all the light will be reflected into the first medium. This is provided by the equation 2.8:

$$\theta_i = \sin^{-1}\left(\frac{n_2}{n_1}\sin\theta_t\right) \tag{2.8}$$

Equations 2.4 and 2.5 provide accurate relations when light is travelling between two non-absorptive media. When applying those equations for absorptive media, it is important to modify the refractive index, adding an imaginary part as in equation 2.9.

$$\tilde{n} = n + i\kappa \tag{2.9}$$

There, the imaginary part κ known as extinction coefficient, is characterised by equation 2.10

$$\kappa = \frac{\alpha\lambda}{4\pi} \tag{2.10}$$

where α is the absorption coefficient and λ the wavelength in vacuum. For absorptive media, the refractive index in equations 2.4 and 2.5 need to be replaced with the complex refractive index [21].

2.4.1. Tauc plot method

Tauc plot method is a graphical method used to determine the energy bandgap of a material, mostly in semiconductors and amorphous materials [22]. It is based on the "Tauc relation", which links the absorption coefficient (α) of the examined material with the energy of the incident photons ($h\nu$). The relation connecting these two is provided by equation 2.11.

$$(\alpha h\nu)^n = A(h\nu - E_g) \tag{2.11}$$

where, α is the absorption coefficient, h is Planck's constant, ν is the frequency, E_g is the energy bandgap, A is a material property and n is a constant that depends on the nature of the electronic transition. Specifically, if $n = 2$, we refer to direct bandgap material and if $n = \frac{1}{2}$, the material is connected with indirect transitions. To calculate the absorption, equation 2.12 was used.

$$1 = A + R + T \tag{2.12}$$

In order to plot the graph, $(\alpha h\nu)^n$ versus $h\nu$, there are some key points. Firstly, the absorption, determined by spectroscopic measurements, is multiplied with $h\nu$. Based on the type of electronic transition -direct or indirect- as it mentioned before, the $(\alpha h\nu)^n$ is calculated and then plotted versus $h\nu$. Then, the linear region is identified and extrapolated to the x-axis. This interception determines the energy bandgap. An example is presented in Figure 2.4.

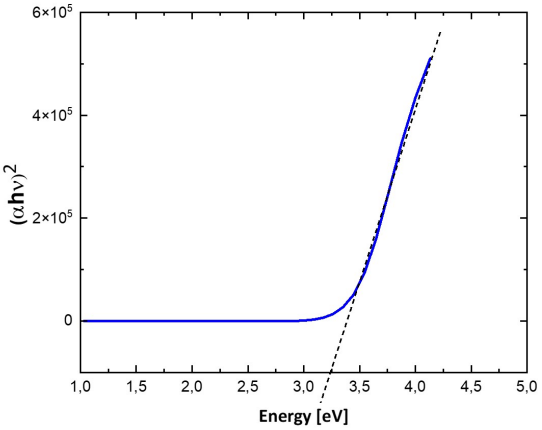

Figure 2.4: Tauc plot for a direct energy bandgap material.

2.4.2. Light management

Light utilization can be improved by ensuring that the design of the solar cell is in such a way that the optical losses are minimized. This can be done by using Anti- Reflective Coating (ARC), which uses the concept of refractive index grading and constructive-destructive interference to decrease the amount of light reflected from the front side of the solar cell [21]. Another method that can optimize light management is to introduce surface texturing at the interface, thereby enhancing the trapping of the light in the solar cell. In this project, only the second method will be utilised.

Texturing effects

The interaction with light and the textured surface is considered to be macroscopic, meaning that the typical length of the surface features is larger than the typical wavelength of light. Hence the Fresnel/Snell equations that was previously explained can describe the scattering of light. The aforementioned light trapping can be visually seen in Figure 2.5. There, the light that is perpendicularly incident on a textured surface could be reflected to another part of this surface, which can then also transmitted into the second medium. This leads to lower reflection losses since more light will enter wanted surface.

A second advantage of a textured surface is that it increases the path length of light within the material. After light surpasses the TCO layer, it travels through the absorb layer until it get absorbed or pass through the solar cell completely. Increasing the path length of the electron, increase the chance to be absorbed and generate electrons. The geometrical reason for the increased path is illustrated in Figure 2.6.

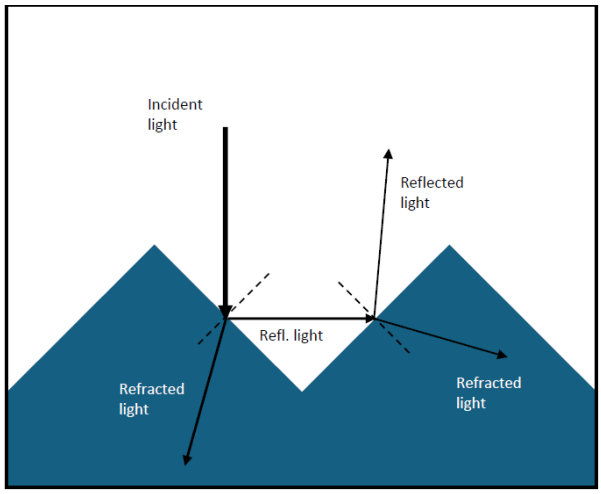

Figure 2.5: Interaction of light at a textured interface

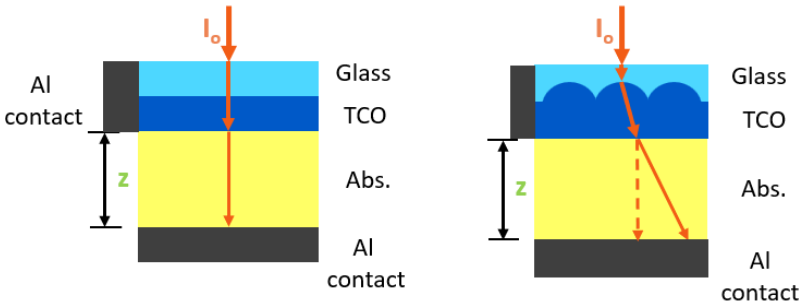

Figure 2.6: Difference between flat (left side) and textured (right side) TCO. I_0 refers to the incident light.

2.5. Opto-electrical trade off

Conductivity is one of the important requirements of a TCO since it prevent excess ohmic losses during lateral charge transport to the metal contact.

Lateral conductivity (σ) is described by 2.13:

$$\sigma = N \cdot e \cdot \mu \tag{2.13}$$

where N is the carrier concentration, e is the elementary charge given by 1.602×10^{-19}C, and μ is the mobility of the charge carriers.

Carrier mobility (μ) is a key metric in semiconductor performance. It represents the ability of carriers to move through the host lattice, and more specifically, how quickly the carriers can travel through the material in an electric field. Mobility is represented by equation 2.14:

$$\mu = \frac{e \cdot \tau}{m^*} \tag{2.14}$$

where e is the elementary charge, τ is the relaxation time, and m^* is the effective mass of the charge carriers. Specifically in an n-type semiconductor, the effective mass ($m*$) describes the mass that one electron appear to have when moving within the lattice.

Based on equation 2.13, in order to improve σ, an increase in both mobility (μ) and free carriers (N) seems highly beneficial. However, it essential to move away from the approach, which focus on increasing the carrier density (N) since it is self-limiting. Specifically, by increasing the carrier density, the carrier relaxation time will also suffer reduction since more scattering will occur by introducing more dopant sites,and this will affect the mobility. Hence, obtaining the highest possible conductivity value is a trade-off between free carriers (N) and mobility (μ), which are related by a rule of [23]:

$$\mu \propto N^{-2/3} \tag{2.15}$$

According to this rule, conductivity cannot continuously improve, leading to an upper limit.

Another trade-off take place and limits the performance of the TCO. A typical image of transmission, reflection and absorption spectra of a TCO material can be seen in Figure 2.7.

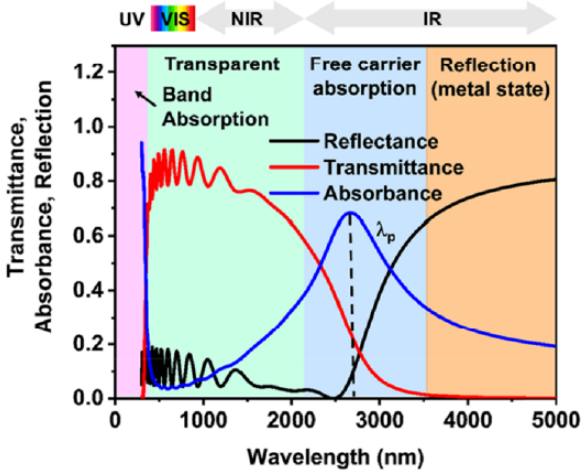

Figure 2.7: Reflection, transmission and absorption (R,T,A) spectra of a metal oxide [24]

The spectra can be separated into three zones [25]. Starting from the short wavelengths-below 400 nm-transmission is very low since absorption of photons with energies higher than the bandgap occurs. For higher wavelengths, where photon energies are below the bandgap, transmission is very high. Going into higher wavelengths- into the near-infrared region (NIR)- absorption occurs again .Specifically, intra-band transitions occurs within the conduction band, leading to optical absorption [26]. This absorption

is well-known as free carriers absorption (FCA) which is modelled by Drude oscillator. The absorption coefficient (α_{FCA}) is given by 2.16:

$$\alpha_{FCA} = \frac{\lambda^2 e^3 N}{4\pi^2 \epsilon_0 c^3 n (m_e^*)^2 \mu_{\text{opt}}} \tag{2.16}$$

where, N is the free carriers concentration, λ is the photon wavelength, e is elementary charge, ϵ_0 is the vacuum permittivity, c is the speed of light in vacuum, n is the refractive index, m_e^* is the effective electron mass and μ_{opt} is the optical mobility. As it can be easily seen in this equation, there is a direct proportionality between absorption coefficient and free carrier concentration, meaning that the higher the carrier concentration of the TCO layer, the more FCA effect occurs in the NIR wavelength range. This explains why increasing N is not the optimal way.

When a conductor is irradiated with light, due to its electromagnetic wave nature, the carriers of the conductor follow the oscillation of these waves, moving with the same frequency. However, there is a characteristic threshold plasma frequency ω_p which is determined by equation 2.17. This can also be translated to a wavelength value λ_p, by equation 2.18 [26]. When the conductor is irradiated by light with frequency higher than its plasma frequency, the carriers of the TCO material cannot catch up with this fast electric oscillation and the light is transmitted through it without interacting. As it can be seen from the equations, increasing the free carrier concentration means increasing the threshold values, thus leading to more photons oscillating with the film and less transmitted through.

$$\omega_p^2 = \frac{Ne \cdot e^2}{\epsilon_0 \cdot m_e^*} \tag{2.17}$$

$$\lambda_p = \frac{2\pi c}{\sqrt{\frac{e^2 N_e}{\epsilon_0 m_e^*}}} \tag{2.18}$$

2.5.1. Scattering mechanisms

Taking into account the previous information, increasing mobility is the correct way in order to increase the conductivity of the TCOs. It has been both theoretically [27] and experimentally [28] found that to provide high-μ TCO films, a larger τ rather than a smaller m* need to be achieved. The overall relaxation time is determined by the total scattering contribution by grain boundaries (GBs), charged centres such as ionized impurities, phonons (lattice vibrations) and stacking faults/dislocations [28]. Based on this, the formula of relaxation time is given as:

$$\frac{1}{\tau_{\text{total}}} = \frac{1}{\tau_{\text{phonon}}} + \frac{1}{\tau_{\text{cc}}} + \frac{1}{\tau_{\text{GB}}} \tag{2.19}$$

where τ_{phonon} is the relaxation time due to polar phonon scattering, τ_{cc} is the relaxation time due to charge carrier scattering which is also known as ionized impurity scattering, and τ_{GB} is the relaxation time due to grain boundary scattering [29]. All the scattering from dislocations and neutral impurities are negligible [30]. By implementing 2.14 the total mobility formula [31], that is also measured by our equipment, is:

$$\frac{1}{\mu_{\text{total}}} = \frac{1}{\mu_{\text{phonon}}} + \frac{1}{\mu_{\text{cc}}} + \frac{1}{\mu_{\text{GB}}} \tag{2.20}$$

Below, a brief explanation of each mechanism is given.

- **Phonon scattering:**

  In both single crystals and polycrystalline materials, phonon scattering occurs due to interactions with the vibrational modes of the crystal lattice, known as phonons. At temperatures higher than 0 K, generated phonons can cause the carriers to scatter. The mobility caused by this mechanism can be estimated from temperature dependent mobility values [32], and it is more significant as temperature increases, since phonon scattering become dominant [31].

- **Ionized impurity scattering:**

  Also known as charged center scattering, is especially relevant in degenerate TCOs doped with oxygen vacancies and impurity atoms. In the crystalline structure, at every position where electrons become freely mobile, an ionized impurity is left behind in its spot which is able to scatter charge carriers. In a doped material, like most of the materials that are used in TCO, this form of scattering is the dominant scattering mechanism. This mobility was calculated by Brooks-Herring-Dingle (B-H-D) theory which taking into account degeneracy, and using both degeneracy and non-parabolicity of the conduction band [33].

  Specifically about Brooks-Herring-Dingle, it is a theoretical model that describes the scattering of all charge carriers (electrons or holes) by ionized impurities. According to this theory, scattering rate increases with the increase of free carriers. This means that the higher the free carriers, the higher the scattering centers and the higher the decrease in mobility [34]. Using the aforementioned methods, a relationship between free carriers (N) and ionized mobility (μ_{II}) can be visually seen in Figure 2.8.

- **Grain boundaries scattering:**

  Polycrystalline TCO films are composed of crystallites joined together by grain boundaries which are regions between different orientations of neighboring crystallites [34]. These interfaces between crystallites are prone to act as defect sources. They operate as carrier traps and creating potential barriers which can prevent carrier transportation. According to researches that have been done [35] [36], by increasing the free carriers, the increase of free carriers (electrons or holes) can neutralize the electric field and in this way reducing the potential barrier (screening effect), leading to easier transportation of electrons and increase in mobility.

  It is also worth mentioning that, the influence of the grain boundary scattering becomes critically important for those samples whose grain sizes are comparable with mean free path of the electrons[31]. For good-quality TCO samples, with high carrier concentrations and large crystallite sizes, the mean free path of free electrons is usually much smaller than the crystallite size of the films. The samples with such small grain sizes and very low mobility are also not practically useful transparent conducting films, therefore this constriction does not apply to our case. In Figure 2.8, a relationship between free carriers (N) and grain boundaries mobility (μ_{GB}) can be visually seen. This curve is based on the behaviour of undoped ZnO films and impurity-doped ZnO films [37].

Adding those scattering mechanisms, the total limitation of TCO materials is shown in 2.8. The effects of this limit and the techniques to bypass this will be discussed in experimental results.

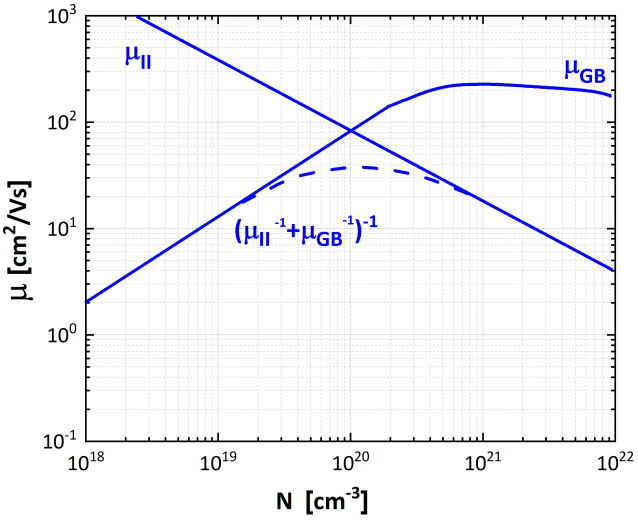

Figure 2.8: Relation of μ_{GB} and μ_i with free carriers (N) [33]

3

Experimental Setup

Deposition of TCO films can be done with a variety of different techniques. In this work, magnetron sputtering will be used. An explanation of this technique will be provided in section 3.1. For the characterisation of the examined TCO films, different equipment w used to measure the opto-electrical properties. A brief introduction to the use of it will be presented in sections 3.2 and 3.3.

3.1. Magnetron Sputtering

Sputter deposition is a widely used technique to deposit thin films on substrates. It is a physical vapour deposition (PVD) technique, based on ion bombardment of a source material, the target. The bombardment is usually done by using an ionized noble gas This results in a vapor due to a purely physical process, the sputtering of the target material. A schematic overview of the equipment is presented in Figure 3.1.

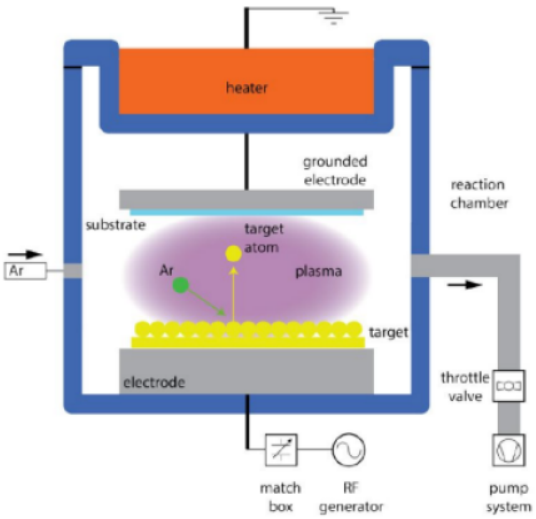

Figure 3.1: RF magnetron sputtering schematic overview [38].

The whole process happens in a vacuum chamber which is evacuated applying pressure with a magnitude of 10^7 mbar in order to avoid contamination. A plasma glow discharge is applied between two parallel plates, in this case anode is the substrade and the cathode is the sputtering target. Then, the working gas is fluxed into the chamber, obtaining an appropriate equilibrium pressure (around 1-10 Pa). The most commonly used gas is Argon due to its ability to produce high sputtering yield [32]. Adding to this, inert Argon gas does not react with the target material, making it suitable for sputtering processes. By applying intense electric field (E), plasma glow is ignited, since the free electrons are accelerated.

This is enhanced by applying a DC or RF (AC) bias depending on the target material (DC is used for conductive materials and RF for both conductive and non-conductive materials). During collisions with the plasma, argon ions gain energy and help with the sputtering process. The magnets that are applied behind the target ensures that most of the sputtered material's kinetic energy will be transferred to the substrate, thus producing high-quality uniform TCO films even at high deposition rate [39].

All the experiments were performed with RF-magnetron sputtering tool from Polyteknic AS, and before every deposition the target was pre-sputtered for 5 minutes to remove any contaminants and eliminate any differential sputtering effects.

3.2. Optical Characterisation

For the optical characterisation of all the TCO properties, spectroscometry is the most commonly used method. For this process, spectroscopic ellipsometry and Lambda Spectroscometry was used. Furthermore, insight about the the thickness of the films can be found with the help of the miniRT equipment. Each different instrument will be briefly presented.

3.2.1. Spectroscopic Ellipsometry (SE)

The equipment used for the project is spectroscopic ellipsometry (SE) M-2000DI system (J.A. Woollam Co., Inc.). SE measurement can provide multiple film parameters such as surface roughness (t_s), refractive index (n), extinction coefficient (k), absorption coefficient (α) and also the optical band gap (Eg),which is extracted based on the SE-fitted α curve [40]. A schematic representation of the aforementioned equipment is presented in Figure 3.3.

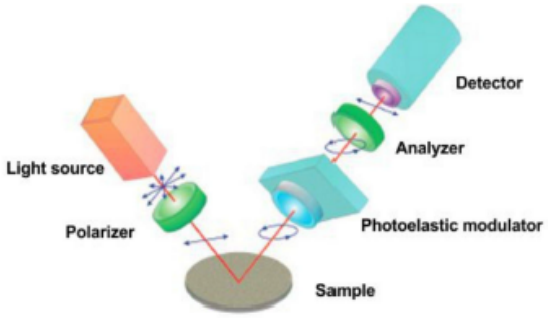

Figure 3.2: Working principle of SE. [19]. Light travels from the light source into the polarizer and then interact with the sample. The new waves go through the Photoelastic modulator before analyzed and detected from the existing setup.

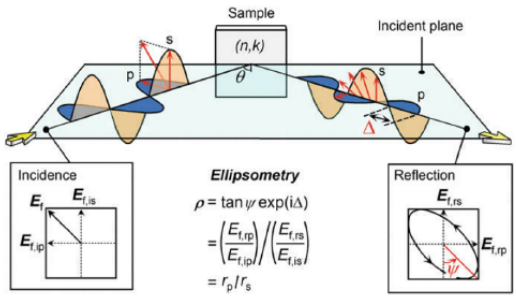

Figure 3.3: Overview of Spectroscopic ellipsometry (SE) [41]. The wave vectors and the ratios of the two polarized light coefficients and also the phase difference Δ and the amplitude ratio Ψ are presented.

The base principle of SE is a reflection-type optical measurement, which enforces the polarization change in the light state upon reflection to determine the samples' optical properties. A phase shift (Δ) between the polarization components of the reflected light, parallel (p) and perpendicular (s) to the plane of light incidence happens in the interface of the sample. Since the absolute values of the reflection coefficients r_p and r_s are not equal (red arrows in the figure), linearly polarized light is converted into elliptically polarized light after reflection. Using the amplitude ratio Ψ and the phase difference Δ, a mathematic fitting that provides the ratio of the two polarization coefficients is extracted. The measured spectra exhibit peaks and valleys,known as interference features, which are due to constructive and destructive interference when the light recombines. The number and the phase of interference features are mostly dependant to film thickness (t) and refractive index (n). More inside on this can be found in Chapter 4 where different graphs for explaining the optical properties of the materials will be examined.

When taking a measurement, it is important to prevent backside reflections. For this reason, it is recommended to use a tape in the backside of the glass substrates [42] and the incidence angle range is 55°-70°.

3.2.2. Lambda spectroscometry

Transmittance (T) and Reflectance (R) spectra of each sample were obtained by using an optical spectrometer, PerkinElmer Lambda 1050 system. An schematic diagram of this spectrometer is represented in Figure 3.4.

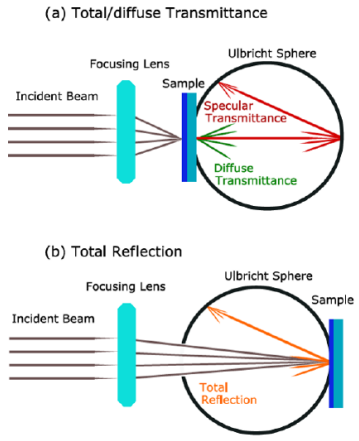

Figure 3.4: Lambda schematic overview [43]

In general the principle of spectrometry can be described as follows. Light is produced by a source including a range between 300-2200 nm, covering that way the ultraviolet, visible, and near infrared spectrum (UV-Vis-NIR). Specifically, the light is produced by a deuterium lamp responsible for the UV light beam and a halogen Wolfram lamp for the Vis-NIR light. Both lamps should b warmed up for 30 minutes to perform with the correct intensity. Then, through a lens the light is transmitted as a straight beam which then pass through a prism and it is divided into several wavelengths. A selector transmits each time only the desired wavelength and after passing through the sample the absorbed photons are detected. This process continues until the whole examined spectrum is covered/ To include also the light scattering, which makes the measurements more accurate, an integrating sphere is used.

In our measurements, the wavelength range of interest is 300-1200 nm with a scanning step of 10 nm, since it basically covers all the usable fraction of solar spectrum that is needed. Furhtermore, using Kirchhoff's law 3.1and the data of transmittance and reflectance values, the absorbance can be calculated.

$$1 = A + R + T \tag{3.1}$$

3.2.3. miniRT

The equipment utilized in the ESP laboratory for measuring the thickness of film samples is an advanced Eta-optic mini RT setup. This specialized apparatus is designed to accurately assess film thickness by analyzing transmittance and reflectance data. These data points are acquired involving optical modeling, which is connected with the setup.

In practice, when transmittance and reflectance spectra are measured, the data is then fitted to the optical model. This process involves manual adjustments of parameters like film thickness, plasma frequency, and oscillator resonance frequency. The goal of these adjustments is to achieve the most optimal fit, characterized by a minimal deviation between the experimental measurements and the theoretical model predictions.

For further enhancement in accuracy and efficiency, an automated optimization procedure is employed. This procedure systematically varies the material properties within the model, refining the fit until there is strong relation between the experimental measured data and the calculated spectra. This approach also ensures a high degree of precision in determining the material properties and thickness of the films under investigation.

3.3. Electrical characterization

Regarding electrical characterization, key parameters such as mobility, free carrier concentration, and sheet resistance needed to be determined. These parameters are usually obtained through Hall effect measurements and Four-Point Probe measurements. Beside that, Scanning Electron Microscopy (SEM) is employed to provide additional insights into the samples' characteristics, such as thickness and compositional analysis. The following section will briefly describe the aforementioned equipment and their respective roles in the characterization process.

3.3.1. Hall effect

Electrical parameters of TCO films, such as carrier concentration (N) and mobility (μ), are measured from Hall measurements, since they can be extracted with the help of Hall effect.

Working principle of Hall is based on Lorentz force, a force to an electric charge which moves along an electric field when a magnetic field is present. This force can be calculated by the following equation 3.2,

$$F = q(E + vB) \tag{3.2}$$

where, F is the force experienced by a charged particle, q is the charge of the particle, E is the electric field, v is particle's velocity and B is the magnetic field. A schematic diagram of Hall measurement can be seen in Figure 3.5

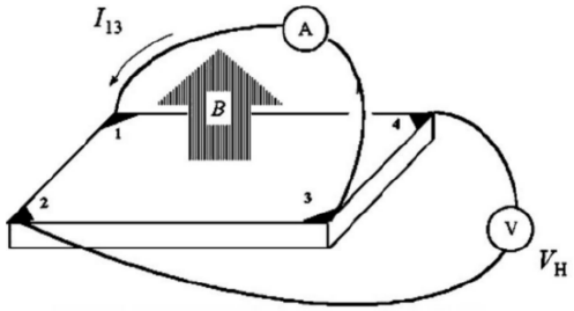

Figure 3.5: Hall schematic overview [44]

When a magnetic field is applied, carriers of the semiconductor tend to shift to one side causing a potential, V_H, which can be measured across the two corners of the film. Furthermore, a current I is applied in the other two opposite corners , as it is presented in the above Figure 3.5. After obtaining this two values, sheet resistance R_{sh} can be determined by the setup and using equations 3.3 and 3.4 free carriers and mobility are determined.

$$N = \frac{r}{qR_H} = \frac{r \cdot I \cdot B}{q \cdot V_H \cdot t} \tag{3.3}$$

$$\mu = \frac{\sigma}{|N|q} = \frac{V_H}{R_{sh} \cdot I \cdot B \cdot t} \tag{3.4}$$

where, t is the determined thickness of the sample. Symbol r represents the Hall scattering factor, which express the energy-dependence of the carrier scattering rate and the typical values are between 1 and 2. In our the Hall measurements r=1. The units of μ is determined as cm^2/Vs.

Last but not least, one can claim that using Hall setup resistivity of the sample (ρ) is possible to be measured by using this method. However,since the 4PP gives a more direct and accurate measurement of the resistivity, Hall equipment was strictly used for mobility and free carrier concentration values.

3.3.2. Four point probe (4PP)

Sheet resistance R_{sh}, an important electrical property of the TCO film, can be identified using the four-point probe (4PP) method. A schematic overview of this is presented in Figure 3.6.

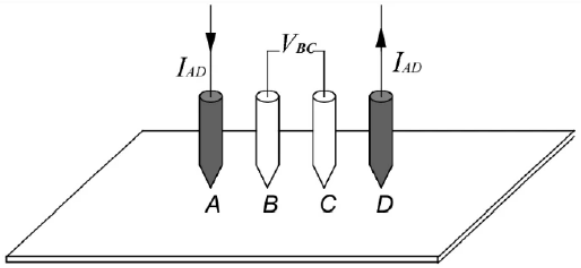

Figure 3.6: 4 point probe schematic overview [45]

Two probes (A and D) are responsible for current carrying where the other two (B and C) are measuring the voltage. After both current and voltage measurements, sheet resistance can be calculated by equation 3.5,

$$R_{sh} = \frac{U}{I} \cdot CF \tag{3.5}$$

where CF is the correction factor determined by samples' dimensions. The measured unit of R_sh is Ω/sq. More details about this method can be found in [46].

3.4. Other material characterisation

Apart from the opto-electrical measurements, we also carried out various material characterizations on the TCO samples, to better understand the TCO properties. Specifically, the crystalline nature of the films was studied with the X-ray diffraction (XRD) technique and surface morphology scanning was carried out using Scanning Electron Microscopy (SEM).

3.4.1. XRD

X-ray diffraction (XRD) analysis is a method of analysing the crystallographic structure of a material by irradiation with incident X-rays, which are generated by directing a high energy electron beam to the target, followed by measuring the intensities and scattering angles after interaction with the aforementioned target. Some common applications are the identification of materials based on their diffraction pattern, phase identification and deviation of the actual structure from the ideal one (owing to internal stresses and defects).

The fundamental theoretical principle behind these measurements is the Bragg's law. The Bragg's Law equation is given by:

$$n\lambda = 2d\sin\theta \tag{3.6}$$

which relates the wavelength of the X-rays (λ), the spacing between the diffraction planes (d), and the angle of incidence (θ). The symbol "n" represents the order of reflection and it is different for each material. After the X-rays encounter the crystal lattice, they are scatter by the atoms into the crystal. There, constructive and destructive interference occurs.Constructive interference occurs when two or more waves overlap in such a way that their amplitudes add together, resulting in a wave of greater amplitude where destructive happens when their amplitudes subtract from each other, resulting in a wave of reduced or zero amplitude. For the first one to occur, the waves must be in phase and for the second one out of phase. In a pollycrystalline material, the possible crystal orientations may be detected by changing θ. The visual result of a constructive interference are high intensities of the reflected x-rays at precise angles, which also give a good indication of the preferred crystal orientation and the degree of crystallinity [47].

3.4.2. Scanning Electron Microscopy (SEM)

A widely applied thin film characterisation technique is the scanning electron microscopy (SEM). SEM can provide valuable insights about the surface morphology, the microstructure and accurate calculations about the thickness and the roughness of the examined material, and helping in this way on its optimisation. A schematic SEM setup is illustrated in Figure 3.7.

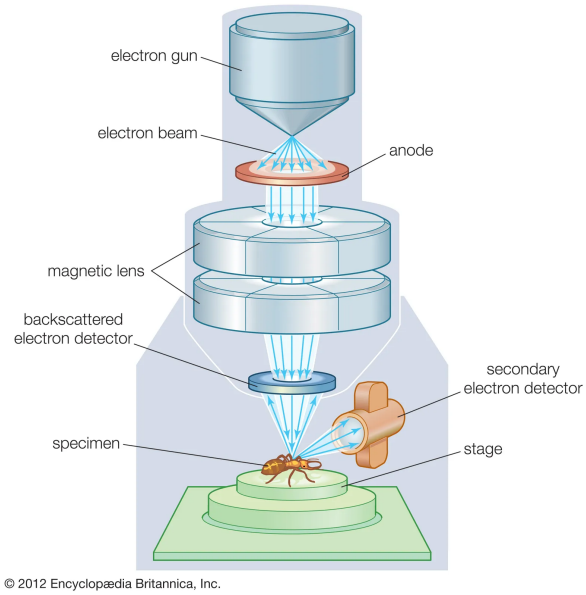

Figure 3.7: Overview of SEM [48]

Additionally, x-rays, photons and heat may also be generated. Scanning electrons are low energy electrons, emitted from surface depth sample atoms as a result of inelastic collisions with primary electrons, thus contain more detailed surface information. BSE's are inelastically scattered electrons with essentially the same energy as incident electrons and provide information about the composition in multi-phase samples. The probability backscattering increases with increasing atomic number of the sample [15]. A field-emission scanning electron microscope (FE-SEM) Hitachi Regulus 8230 was used for characterisation of thin films in the research.

SEM operates by using a focused beam of electrons,with energy from a few thousand up to 50 keV, are utilised to create highly detailed images of a sample. Firstly an electron gun, emits a stream of high-energy electrons, which are then directed and concentrated into a fine point using a series of electromagnetic lenses, specifically the condenser and objective lenses. This finely focused electron beam is then scanned across the sample's surface in a precise grid-like pattern using scanning coils that control the movement of the beam.

When the electron beam interacts with the sample, different interactions occur, leading to different types of signals, such as secondary electrons and backscattered electrons. Additionally, x-rays, photons and heat may also be generated. Secondary electrons(SE), are low energy electrons, emitted from surface depth sample atoms as a result of inelastic collisions with primary electrons, thus contain more detailed surface information. Backscattered electrons(BSE), which are electrons that are reflected back from the sample, provide compositional contrast because their signal intensity varies with the atomic number of the elements in the sample. This allows for differentiation between areas with different elemental compositions.

All these interactions and signal detection occur within a high-vacuum environment, which is essential to prevent the electrons from scattering due to collisions with air molecules. Furthermore, vacuum environment ensures that the electron beam remains focused and the signals generated from the sample are clear [48].

3.5. Experiment variables

The performance of the sputtered films is heavily dependent on the deposition parameters. In this section an overview of the key parameters will be presented.

- **Power**

  Power [W], has a significant role in determining the rate of material deposition. Specifically, when high power is used the deposition time is reduced but the high power of the bombardment might lead to a not uniformed deposition of the material. On the other hand, low power prolongs the deposition process and may reduce the efficiency. Thus, an optimal power has to be found.

- **Process Pressure (p.p)**

  Process pressure [mbar] is the overall pressure within the sputtering chamber.

- **Gas**

  Inert gas has the ability to not react chemically with the target material, the substrate, or the deposited film which is crucial for maintaining the purity and the desired chemical composition of the thin film. The gas can change depending on deposition but it is usually Argon (Ar). The atomic mass of argon (40 a.u.) is well-suited for the sputtering [32]. The efficiency of sputtering heavily relies on the momentum transfer from the gas ions to the the target material's atoms. Higher masses provide the ability to transfer more of that energy to the material leading to higher yields. Lastly, being abundant, non-toxic and non-flammable is very important in laboratory and industrial environment.

- **Deposition rate (d.rate)**

  Thickness is a property that is has to be carefully selected. Based on deposition rate [nm/s], it is possible to achieve the expected thickness. Using a testing sample before any deposition is mandatory in order to calculate this parameter.

- **Partial Water Pressure (p.water)**

  Hydrogenation is the addition of hydrogen atoms into the material's structure. Hydrogen atoms helps in the passivation of the defects in the material's structure improving its properties. Water vapor present during deposition is the source of those atoms. Having the appropriate control can lead to the desired doping levels [49].

- **Temperature**

  Temperature [°C] is one of the most important properties during deposition. Temperature during the deposition differs from the actual temperature that the substrate has, due to the gap between the heater and the substrate. The relation between the two temperatures is expressed by equation 3.7:

  $$T_s = 0.611 \times T_h - 26.8 \tag{3.7}$$

  where T_s is the substrate temperature and T_h is the heater temperature. In the experimental part, deposition temperature values refer to heater temperatures.

- **Post Deposition Annealing treatment (PDA)**

  The available equipment only had the capability to vary the temperature for certain materials. To tackle this, the post deposition annealing treatment (PDA) was used. It is a technique in which the samples are placed in an ambient environment with high temperature in order to increase the substrate temperature, affecting their morphology. Solid phase crystallisation by post deposition annealing (PDA) has been known to enhance electrical properties for TCO's since it decrease the defects of the material's structure. PDA treatment can be done by varying the time of the treatment or the temperature. In this thesis, temperature was kept constant at 200°C, based on previous works optimisations [19], [50].

4

Investigated Materials

In this section a brief overview of the single layers used in this project is presented, followed by the experimental results that was acquired and a brief discussion over them.

4.1. Indium Oxide

Indium oxide (In_2O_3) is commonly used for TCOs. It is one of the few materials that can be easily doped to high concentrations (up to 10^{21} cm^{-3}) while maintaining good transparency, covering in that way the requirements for good opto-electronic properties. Indium oxide has a cubic structure with a melting point temperature of 1910˚C and may be amorphous or crystalline depending on the deposition conditions. Regading its crystalline form, In_2O_3 may exist either in the meta-stable rhombohedral -or the stable cubic bixbyite (BCC) structure as it can be seen in Figure 4.1.

In the second structure (BCC), the unit cell contains 80 atoms, 48 of which are oxygen. As for the indium atoms, there are two distinct sites, In1 and In2. In BCC structure the bandgap reaches values of around 2.9 eV [44].

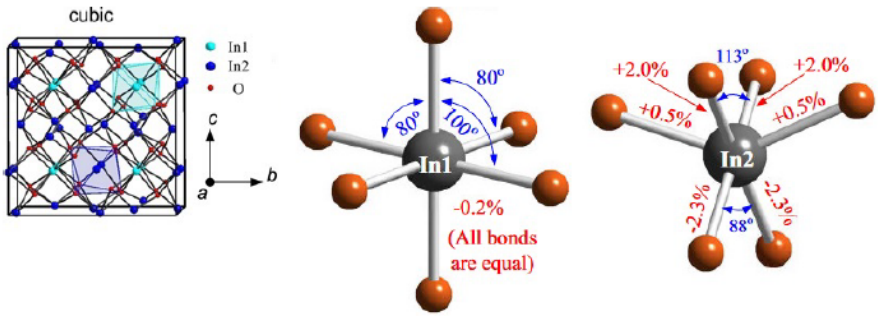

Figure 4.1: Structure of BCC In_2O_3 and the two possible coordinations In1 and In2 [51]

As it mentioned, Indium oxide is a material that it can be easily doped. Using that characteristic, materials like Cerium (C), tin (Sn) and hydrogen (H) was used and analysed in next chapters in order to boost its opto-electrical properties.

4.1.1. Tin doped Indium Oxide (ITO)

As it has been said in TCO introduction 2.1, Indium tin oxide (ITO) is one of the most commonly used front contact material for solar cells. ITO is well-known for having a high optical transparency, specifically above 80% for visible light, and also a low electrical resistivity, around $5 \times 10^{-4}\,\Omega$ cm [52]. In the PVMD group, a 75 nm-thick ITO layer presents a mobility of 25 cm^2/Vs and resistivity of $5.7 \times 10^{-4}\,\Omega \cdot$cm.

ITO is a crucial material that will serve as a reference point for comparison with other materials, both

in single-layer and bi-layer configurations. In our experiment, a preliminary investigation of indium tin oxide (ITO) was conducted, with the primary aim of verifying previously established parameters rather than optimizing them.

Experiment results

Two deposition temperatures were explored, room temperature and 206°C. Power was kept constant and the value was selected at 130 W based on previous researches [19]. The complete plan can be found in Appendix A.1.

In Table 4.1, the thickness of the deposited samples at different temperatures are presented.

T [°C]	Thickness [nm]
25	234.3
206	142

Table 4.1: Thickness for ITO samples at different temperatures.

The expected thickness for those samples was 150 nm. The first experiment conducted at room temperature, providing a sample with thickness of 234 nm, almost 100 nm higher than the expected one. Even though the deposition rate (0.79 nm/s) acquired after the experiment was significantly close to the aimed one (0.85 nm/s), the results made clear that temperature plays a critical role in the thickness of the sample. Regarding the higher temperature, the thickness -142 nm- was much closer to the aimed one, marking the accuracy of the deposition rate at these conditions.

Regarding the optical properties of the ITO samples, Figure 4.2 represents reflectance and transmittance curves. Sample deposited at room temperature has an increased gain in transmittance at UV region. Table 4.2 presents the average values of transmittance and reflectance. The spectrum used for these calculations begins from the point where the transmittance starts to reach significant values. The high value in transmittance, especially at room temperature verifies the good optical properties of the material. Even though not all of the parameters are optimized, especially the thickness of the sample deposited at room temperature, the transmittance value is aligned with the literature values-around 89% [53].

T°C	T[%]	R[%]
25	84.4±3.5	13.5±2.7
206	78.8±5.4	15.1±4.1

Table 4.2: Transmittance and Reflectance values for ITO samples at different temperatures.

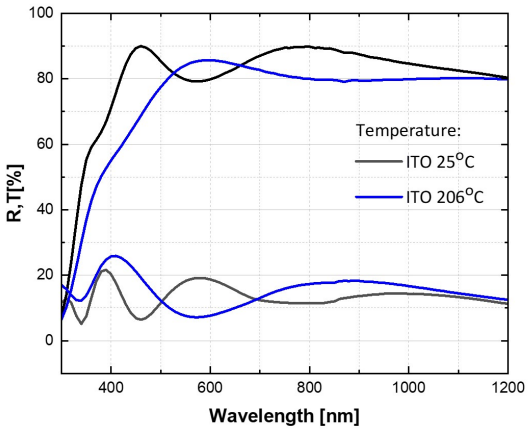

Figure 4.2: Reflectance and transmittance of ITO samples deposited at room temperature and at 206°C

When it comes to the comparison between those two deposition temperatures, room temperature depositions seems to favor ITO. The average transmittance of sample at this temperature is significantly higher than the the other. Furthermore, in Figure 4.2 it is clear that the sample deposited at room temperature is also highly transparent at the 400-500 nm in contrast to the other.

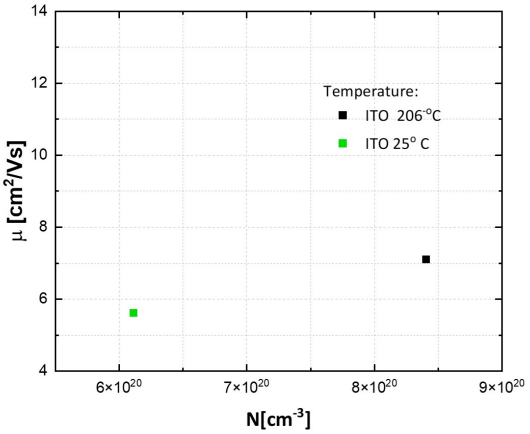

Figure 4.3: Mobility vs free carrier concentration of ITO samples deposited at room temperature and at 206°C.

Figure 4.3 represents the mobility and the free carrier concentration of ITO. Both samples have similar mobility - 7 m^2/Vs and 8 cm^2/Vs -and free carriers with magnitude of 10^{20} cm^{-3}. Compared to the values measured by former research- 25 cm^2/Vs [19]-electrical properties are under-performing, which means that more optimisation need to be done. As for the free carrier concentration, same magnitude with both the measurements mentioned before are obtained also in this research.

Despite the good opto-electrical trade-off that ITO provides, it exhibits significant limitations due to free carrier absorption in the near-infrared (NIR) region of the solar spectrum, which is associated with the high concentration of free carriers in those thin films. Thus, an investigation of alternative materials that can mitigate these losses while maintaining the desirable properties of TCOs is required.

4.1.2. Cerium doped Indium Oxide (ICO)

Another material that is being currently explored is Cerium-doped indium oxide (ICO). An advantage of ICO can be found in its wide bandgap of more than 3.6 eV [54].ICO can reach high mobility values. With RF magnetron sputtering, values of 71 cm^2/Vs for depositions with a substrate temperature of 160°C and 50 cm^2/Vs with room temperature have been reported [55]. Resistivity of $5.74 \times 10^{-4}\,\Omega \cdot$cm and a high average transmittance of 83.5% ranging from 400 nm to 1200 nm have been also found it the same researches.

In this project, different deposition powers and process pressures have been investigated to determine the optimal parameters for high opto-electrical properties.

Experiment results

Power

Deposition power will be the first parameter that will be varied. The exact plan can be found in Appendix B.1. In the performed experiment, a power range between 60-200 W has been investigated.

Thickness

Since the deposition rate increases with power, the deposition time has been adjusted accordingly to achieve the similar thickness in all samples. The aimed thickness was 100 nm. Calculations can be found in Appendix B.3.

The miniRT equipment was used to verify the thickness of each different sample and the results are presented in Table 4.3.

Power [W]	Sample	thickness [nm]	fit deviation
ICO (P=60W)	Left	92.4	0.0008131
	Middle	95.2	0.0009928
	Right	91.4	0.0007598
ICO (P=100W)	Left	90.8	0.0009133
	Middle	95.8	0.0007559
	Right	84.4	0.0009912
ICO (P=150W)	Left	93.7	0.0010664
	Middle	101.9	0.0005391
	Right	84.8	0.0009131
ICO (P=200W)	Left	91.1	0.0006627
	Middle	103.1	0.0004603
	Right	82.4	0.0008990

Table 4.3: Thickness and fit deviation of ICO samples in power series experiment.

Three samples were prepared for each power level. The middle sample consistently exhibits an increased thickness compared to the other two samples. This phenomenon can be explained by taking into consideration Figure 4.4, which illustrates the positioning of the samples within the sample holders that are placed inside the deposition chamber.

The distribution of the sputtered material across the sample holder is not homogeneous. Specifically, the target is circular, which results in a higher concentration of sputtered material in the middle of the sample holders. This leads to greater thickness in this sample.

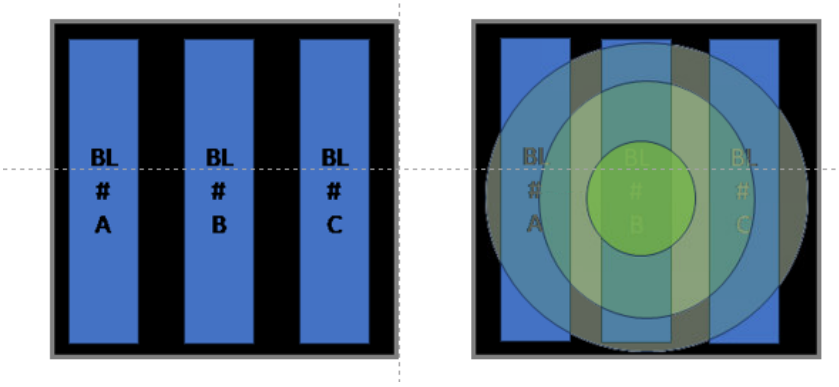

Figure 4.4: Left: Sample position in the holder for deposition. Right: Sputtering distribution based on available equipment target.

Regarding the middle sample, in every power the thickness is well aligned with the expected one. To assess the reliability of the thickness data, fit deviation is used. All values are below 0.001, indicating a high level of precision.

Optical Characterisation

Using Lambda equipment, transmittance and reflectance of the films throughout 300-1200 nm wavelength spectrum are acquired. The curves of samples with different deposition power are presented in Figure 4.5. In this figure, only the samples corresponding to the lowest -60W- and the highest power setting -200W- are presented. This choice has been made since samples in intermediate power levels, exhibit behaviors that are fall within the range established by these two extremes. The complete graph, with data from all power levels, can be found in Appendix B.1.

The data presented in Figure 4.4 illustrates that, the behavior of both samples aligns with the trends presented in 2.7. ICO curve shows fewer fringes in the UV spectrum , indicating reduced destructive and constructive interference at that wavelength, which contributes to a smoother curve across the spectrum. The average values and the fluctuations across the entire wavelength spectrum are detailed in Table 4.4.

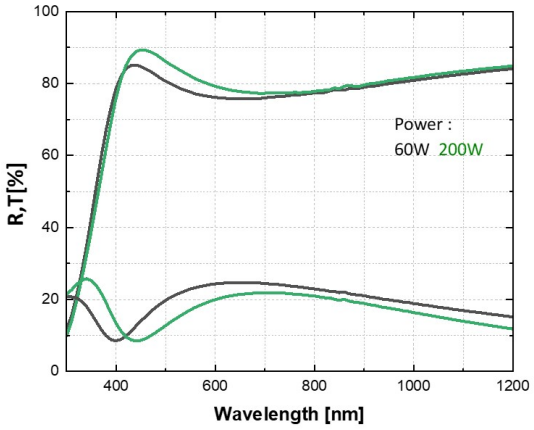

Figure 4.5: Reflectance and transmittance of ICO samples deposited at 60W and 200W in as deposited conditions

Power [W]	Avg T [%]	Avg R [%]
60	79.59 $\pm$ 2.9	20.29 $\pm$ 3.6
200	81.38 $\pm$ 3.4	17.00 $\pm$ 3.9

Table 4.4: Average reflectance (R) and transmittance(T) across 400-1200 nm.

Again, the average transmittance is determined by integrating the total transmittance and reflectance across the effective light spectrum - 400 to 1200 nm. The values obtained for both samples at different deposition powers were consistent with the literature-approximately 83%.

By examining the different deposition powers, the data from the graph and table indicate that higher power results in slightly better transmittance between 400-700 nm. After this range, the transmittance curves for both materials overlap, meaning similar results.

Another optical property that is examined is the energy bandgap. It is calculates by Tauc plot method, as described in 2.4.1. The energy bandgap was also measured by spectroscopic ellipsometry equipment. The results are presented in Table 4.5. The Tauc plots can be found in Appendix B.4. The minimal deviation observed between Eg values derived from both methods verifies the precision of the values.

Power [W]	Eg [eV] (as deposited)		Eg [eV] (annealed)	
	from Tauc plot	from SE	from Tauc plot	from SE
60	3.21	3.26	3.31	3.4
200	3.17	3.27	3.31	3.33

Table 4.5: Energy bandgap values for power series experiment, in as-deposited and annealed conditions, from Tauc plot and SE.

In as-deposited conditions, values for both power levels do not fully align with the literature- around 3.6 eV reported. A way to narrow the deviation is by improving the crystallinity of the material.

Crystallinity plays a crucial role in reducing defects such as grain boundaries, dislocations, and amorphous regions. These defects are critical because they can introduce localized states within the band gap, leading to sub-band gap absorption. By minimizing these defects, the material can exhibit a cleaner and more well-defined band gap. One effective approach to enhancing crystallinity is PDA treatment. Elevating the substrate temperature can significantly improve crystallinity by promoting better atomic ordering within the material.

Figure 4.6 represents the reflectance and transmittance measurements before and after annealing. It can be seen that there is a slight gain in transmittance curve in both powers across the whole wavelength while reflectance losses are maintained the same. According to the Tauc plot method, this

implies an increase in the energy bandgap. This is verified by Table 4.5. This highlights the significance of temperature in enhancing material properties, since the deviation from the literature values is significantly reduced. Specifically in deposition at 60 W, the values observed in Table 4.5 are closer to the literature - indicating that this power provides better samples.

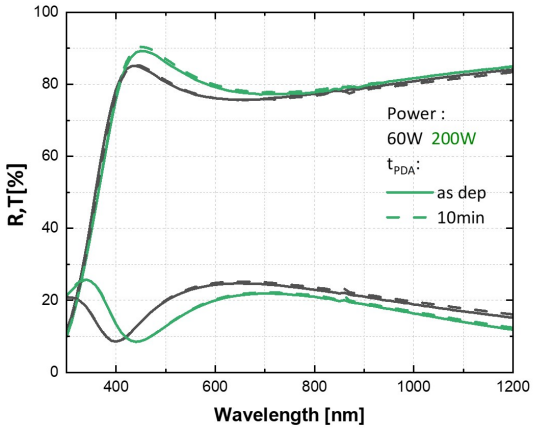

Figure 4.6: Reflectance and Transmittance of ICO samples deposited at 60W and 200W in as deposited and annealed conditions.

Electrical Characterisation

For the electrical characterization of the deposited films, mobility and free carrier concentration are examined and presented in Figures 4.8 and 4.7. For the same reason explained in optical characterisation, in those figures only the higher and lower power samples are represented and the complete figures can be found in Appendix B.5 and B.6.

In as deposited conditions, films at higher power have lower mobility and increased free carriers. Despite higher power can theoretically enhance film quality by increasing the frequency of collisions within the plasma, it is also increases the number of collisions with the film surface. This phenomenon can lead to film damage during formation, leading to an increased defect density. Additionally, maintaining the film thickness constant, using higher deposition powers requires a reduction in deposition time. This shorter deposition time may result in insufficient crystallization, causing the films to become more amorphous under these conditions [56]. Compared to the literature values- 50 cm^2/Vs- this project's values fell relatively lower at 22-33 cm^2/Vs range. As for the free carriers, both powers are aligned with the same magnitude as in literature-10^{20} cm^{-3}.

X-axis represents the PDA time steps. It is observed an increased slope until 10 minutes mark, indicating the critical effect that temperature has in the performance of the sample. After 10 minutes the electrical properties fall down rapidly, indicating that the optimal annealing time step is at 10 minutes. The analysis of free carriers over time reveals that at the 10-minute mark, the concentration of free carriers meats its lowest value.

XRD

To further validate the crystallinity assumption, X-Ray Diffraction (XRD) measurements were conducted both before and after the annealing process.

As detailed in Section 3.4.1, XRD is a method that can help in validating the degree of crystallinity in materials. The results of these XRD measurements are illustrated in Figure 4.9. On this graph, y-axis represents the intensity, which correlates with the preferred orientation of the crystalline planes within the material and the x-axis corresponds to the angle θ, which after using Bragg's Law, helps with the identification of specific crystallographic orientations in the sample.

From those XRD results, it is easily observed that the material exhibits two distinct peaks after annealing process. These peaks indicate the emergence of preferred orientations in the crystalline structure,

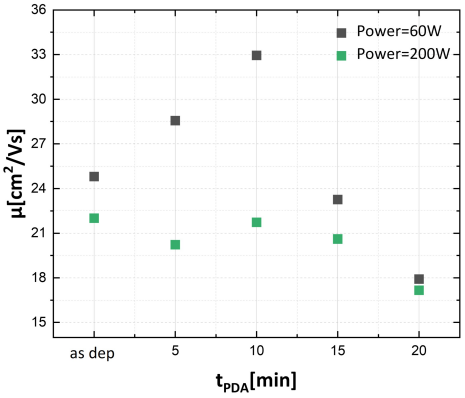

Figure 4.7: Mobility values of ICO samples deposited at 60W and 200W versus PDA time.

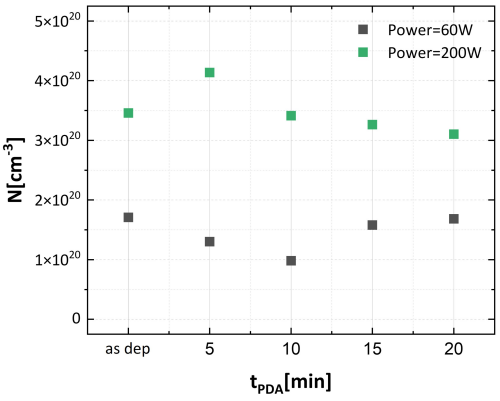

Figure 4.8: Free carriers concentration of ICO samples deposited at 60W and 200W versus PDA time.

which were absent in the as-deposited, amorphous state of the material. The presence of these peaks post-annealing confirms that the material transition from an amorphous to a more crystalline state. That supports the assumption that the reduction in free carriers at 10 minutes corresponds to a significant improvement in the crystallinity.

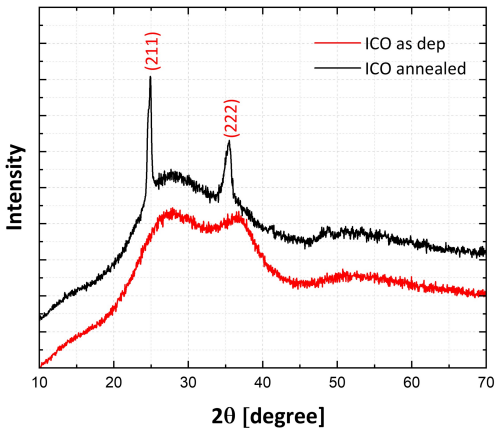

Figure 4.9: XRD measurements for ICO sample deposited at 60W in as deposited and after 10 minutes PDA treatment

Process Pressure

Process pressure was the other parameter varied during the experimental process. In previous experiment, process pressure was kept constant at 3e-3 mbar. A second experiment was conducted in which this property was varied. The range explored during this experiment was from 3e-3 mbar to 6e-3 mbar. During this experimental series, film thickness was kept constant at 100 nm, where power level was set at 60 W, as it offered the better trade-off between opto-electrical properties. The detailed experimental plan can be found in Appendix B.2.

Thickness

Table 4.6 illustrates the effect of this parameter in the samples' thickness. Thickness differs from the value that was aimed for, supporting the case that every different deposition cannot present the exactly similar results. An explanation about the increase of thickness when the pressure decrease is that at higher pressures, the collisions between sputtered particles are increased. This leading to less deposited particles, thus decreasing the thickness in the same time [57]. Thus, a small change in the deposition time, for each different process pressure applied, has to be made in further experiments.

p.p [mbar]	Thickness [nm]	Fit Deviation
3e-3	124.8	0.0011
4e-3	116.9	0.0016
5e-3	119.3	0.0016
6e-3	112.4	0.0017

Table 4.6: Thickness and fit deviation of ICO samples in p.p experimental series

Optical Characterisation

Reflectance and transmittance curves are presented in Figures 4.10 and 4.11. Regarding the curves' behaviours, a slight decrease in UV region can be observed in the sample processed at 3e-3 mbar. This is attributed to the slight increased thickness of the examined sample compared to the others.

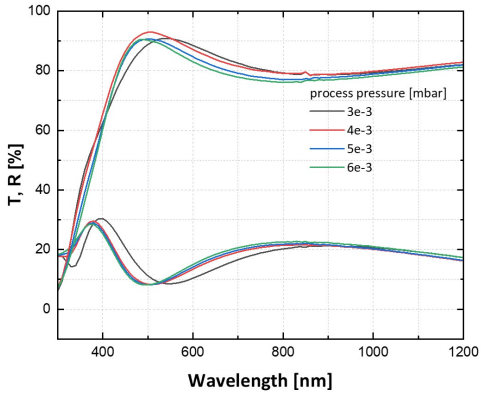

Figure 4.10: Reflectance and transmittance of ICO samples for p.p experimental series in as deposited conditions.

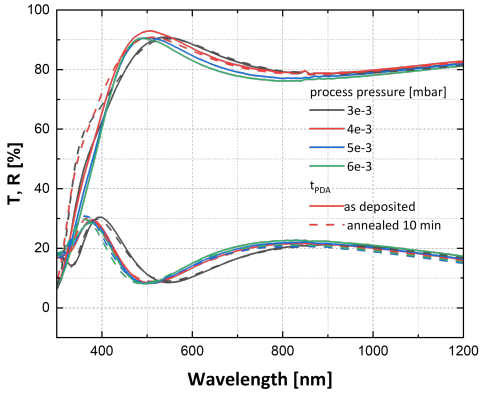

Figure 4.11: Reflectance and transmittance of ICO samples p.p experimental series in as deposited and annealed conditions.

Furthermore, Table 4.7 illustrates the average transmittance values in the active wavelength range. In as deposited conditions, there is no significant deviation between different process pressures, leading to a conclusion that this parameter does not affect transmittance. Taking into account the values after PDA treatment, there is a slight increase in all different process pressures, indicating the positive effect of this treatment.

For energy bandgap, the values measured using the Tauc plot model and spectroscopic ellipsometry equipment are presented in Table 4.8.

p.p [mbar]	Avg T [%] (as deposited)	Avg T [%] (annealed)
3e-3	81.9 ± 4.5	81.9 ± 4.2
4e-3	82.7 ± 4.6	82.1 ± 3.9
5e-3	81.1 ± 4.4	82.6 ± 3.8
6e-3	80.2 ± 4.4	81.9 ± 4.1

Table 4.7: Average transmittance(T) across 400-1200 nm in as deposited and annealed conditions

p.p [mbar]	Eg [eV] (as deposited)		Eg [eV] (annealed)	
	from Tauc plot	from SE	from Tauc plot	from SE
3e-3	3.21	3.28	3.41	3.39
4e-3	3.26	3.23	3.49	3.47
5e-3	3.21	3.24	3.52	3.49
6e-3	3.22	3.22	3.51	3.49

Table 4.8: Eg values in as deposited and annealed conditions, by Tauc plot method and SE for p.p experimental series.

By comparing the values of sample processed at 3e-3 mbar with those obtained in the power series experiment, it is evident that the values in both as-deposited and annealed conditions are consistent, highlighting the reliability and accuracy of both measurement methods.

Samples in as-deposited conditions exhibit no significant fluctuation in energy bandgap values across the different pressures. However, PDA treatment reveals a trend. With increased pressure, the energy bandgap increase, approaching more closely the literature reported values, 3.5 to 3.6 eV.

Electrical Characterisation

Mobility and free carrier concentration results are demonstrated in Figures 4.12 and 4.13.

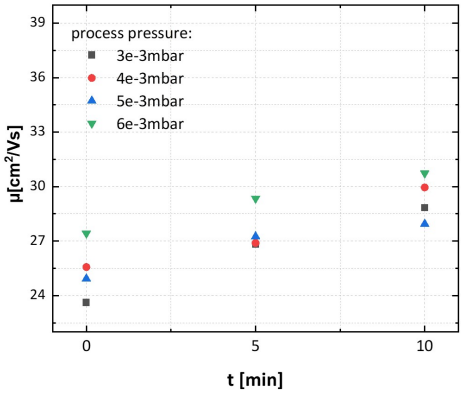

Figure 4.12: Mobility vs PDA time of ICO samples for p.p experimental series.

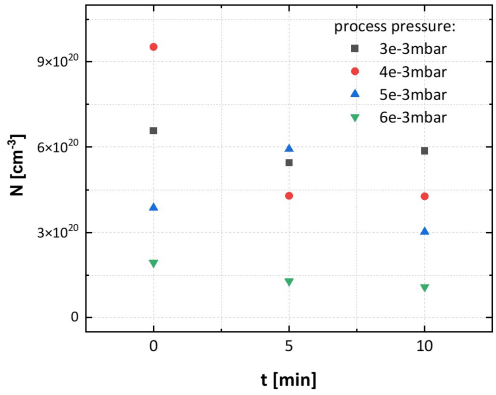

Figure 4.13: Free carriers concentration vs PDA time of ICO samples for p.p experimental series.

The data indicates that mobility reaches higher values at 10 minutes of PDA. This supports the conclusion made from the power series experiment, that 10 minutes is the optimal PDA time.

Examining the effect of varying process pressures, there is no significant deviation in mobility values in each different time step, suggesting that it does not have a strong influence.

Conclusion

Considering both the electrical and optical properties of the samples, it can be concluded that the optimal deposition power for this material is 60W, since highest mobility values were measured, which is crucial for enhancing the electrical conductivity of the material. Other properties as energy bandgap and average transmittance did not affected by the increase of power. Regarding the process pressure,

the experimental results did not reveal a clear trend across the range of pressures tested. The lack of a clear trend in mobility and other attributes indicates that further investigation is necessary.

4.1.3. Hydrogen Doped Indium Oxide (IOH)

Another doped indium oxide material that has been extensively explored is hydrogen-doped indium oxide (IOH). The primary advantage of IOH lies in its favourable electrical properties, which have been reported. Specifically, IOH exhibits mobilities up to 100 cm^2/Vs when deposited using magnetron sputtering. Additionally, IOH demonstrates a wide energy bandgap, typically ranging from 3.4 eV to 3.8 eV. This material also exhibits free carriers concentration in the order of 10 $^{19}cm^{-3}$ to 10 $^{20}cm^{-3}$ and an average transmittance of approximately 85% in the visible spectrum [58].

Experiment results

In this project, the impact of two variables will be explored: power and partial water pressure. Regarding power, as highlighted in the literature [58], values below 200 W tend to give better results in both optical and electrical properties. Therefore, power levels ranging from 150 W to 200 W will be employed in this study. As for the partial water pressure, a baseline value of 3e-5 mbar will be used. To further investigate the role of water pressure, this value will be doubled in the experiments to observe its influence on the material's characteristics. The complete plan can be found in Appendix C.1.

Thinckness

First, the impact on the material thickness must be evaluated. The target thickness for the deposition, consistent with other materials in this study, was set at 100 nm. As shown in Table 4.9, this target was successfully met in most cases. Specifically, with regard to water pressure, it was observed that lower values provided slightly reduced thicknesses compared to 6e-5 mbar, which produced results closely aligned with the intended thickness.

As the applied power increases, the thickness of the deposited material appears to decrease. This phenomenon can be attributed to the more intense sputtering that occurs at higher power levels. The increased energy causes the sputtered material to strike the substrate with higher force, potentially leading to damage and a reduction in the material thickness. In contrast, lower power levels result in a more uniform and controlled sputtering process and ensures greater accuracy in the deposition rate.

Power [W]	p. water [mbar]	Thickness [nm]
150	3e-5	92.6
180	3e-5	89.3
200	3e-5	87.5
150	6e-5	102.3
180	6e-5	99.7
200	6e-5	93.1

Table 4.9: Thickness of IOH samples in power series and partial water pressure experiments.

Optical Characterisation

Transmittance and reflectance curves of the samples deposited at varied powers, in 3e-5 mbar and 6e-5 mbar are presented in Figures 4.14 and 4.15 respectively.

In both depositions with varying partial water pressures, the lower power levels yield slightly better performance, as indicated by a greater gain in the UV region. This is also supported by Table 4.10 were the average transmittance values are presented.

PDA treatment improved the curves in UV region. Similar to the case of ICO, the PDA treatment enhances material's crystallinity. The positive effect of this treatment is further reflected in the average values, detailed in Table 4.11. There, an increase of 1-1.5% in average transmittance was observed compared to the as deposited conditions.

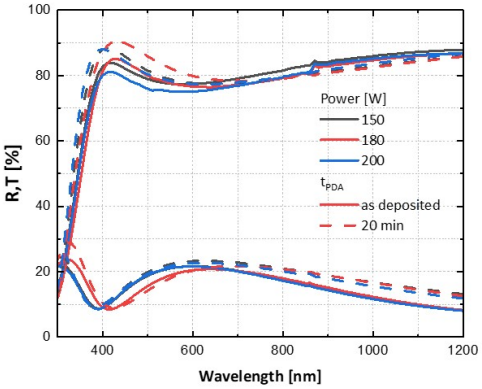

Figure 4.14: Reflectance and transmittance of IOH samples for power experimental series with p.water = 3*10^{-5} mbar

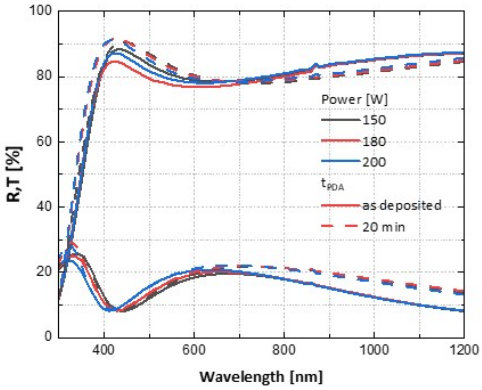

Figure 4.15: Reflectance and transmittance of IOH samples for power experimental series with p.water = 6*10^{-5} mbar

Power [W]	p. water [mbar]	avg T [%] (as dep)	avg R [%] (as dep)
150	3e-5	82.58±3.6	15.35±4.5
180	3e-5	81.54±3.6	14.87±4.3
200	3e-5	80.82±4.2	14.23±4.6
150	6e-5	82.97±3.2	14.23±3.9
180	6e-5	81.85±3.6	14.57±4.1
200	6e-5	80.78±3.3	14.87±4.3

Table 4.10: Transmittance and reflectance values of IOH sampls at power and partial water pressure experiment series, in as deposited conditions.

Regarding energy bandgap, the values of each different deposition combination are presented in Tables 4.12 and 4.13.

In almost every combination, SE values were consistently 0.5 eV higher than those obtained from the Tauc plots. SE values reached as high as 4 eV, which exceeds the values typically reported in the literature. Due to this discrepancy, more emphasis will be placed on the values obtained from the Tauc plot method. The plots used to calculate the energy bandgap for each material can be found in Appendix C.1 and C.4.

In the as-deposited condition, the energy bandgap ranges from 3.3 to 3.4 eV. This suggests that neither power nor water pressure has a significant effect on the energy bandgap under these conditions.

However, after the application of the post-deposition annealing (PDA) treatment, all combinations exhibit an increase in the energy bandgap by approximately 0.2-0.3 eV. highlighting the critical role of crystallinity in determining the material's properties.

Power [W]	p. water [mbar]	avg T [%] (with PDA)	avg R [%] (with PDA)
150	3e-5	82.55±3.1	17.63±3.6
180	3e-5	82.41±3.4	17.15±3.7
200	3e-5	81.72±3.2	17.79±3.7
150	6e-5	82.90±3.5	17.46±3.8
180	6e-5	82.24±3.6	17.74±3.7
200	6e-5	82.31±3.4	17.67±3.6

Table 4.11: Transmittance and reflectance values of IOH sampls at power and partial water pressure experiment series, in annealed conditions.

Power [W]	SE		Tauc plot	
	as dep	$t_{PDA} = 20$ min	as dep	$t_{PDA} = 20$ min
150	3.419	3.978	3.31	3.63
180	3.428	4.000	3.34	3.65
200	3.248	3.987	3.27	3.59

Table 4.12: Eg [eV] values from SE and Tauc plot at p.water=3e-5 mbar.

Electrical Characterisation

In Figures 4.16, 4.17 4.18, 4.19 results for mobility and for free carriers concentration are presented. Firstly examining the mobility values, in all depositions, there is a noticeable increase in mobility by 5-9 cm^2/Vs when applying PDA treatment. In terms of power, its variations do not appear to significantly affect mobility. The values remain clustered within the same range under both as-deposited and PDA-treated conditions. Similarly, the partial water pressure does not seem to have an impact on mobility. In both cases, the mobility values cluster to a range of 23-25 cm^2/Vs for the as-deposited samples and 28-31 cm^2/Vs after PDA treatment. Although these values are comparable to those observed for ICO materials, when compared to the literature-reported values—around 100 cm^2/Vs—they fall significantly short.

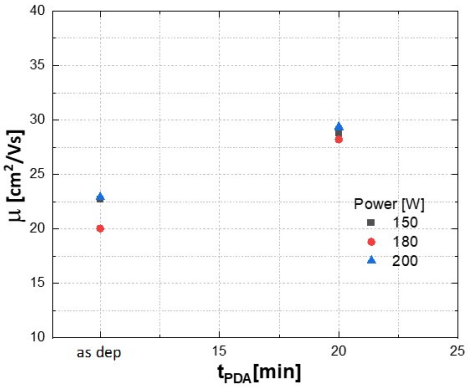

Figure 4.16: Mobility vs PDA time of IOH samples for power experimental series with p.water = 3*10^{-5} mbar.

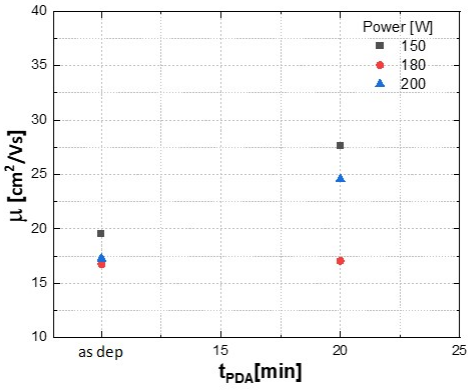

Figure 4.17: Mobility vs PDA time of IOH samples for power experimental series with p.water = 6*10^{-5} mbar.

Regarding the free carriers concentration, PDA treatment has a significant impact, as the values decrease by an order of magnitude compared to the as-deposited conditions. Similar to the mobility results, power does not appear to play a critical role, as all values remain closely clustered together at each respective time step.

Power [W]	SE		Tauc plot	
	as dep	$t_{PDA} = 20$ min	as dep	$t_{PDA} = 20$ min
150	3.985	3.981	3.36	3.62
180	4.007	3.976	3.43	3.65
200	4.016	3.984	3.33	3.64

Table 4.13: Eg [eV] values from SE and Tauc plot at p.water=6e-5 mbar.

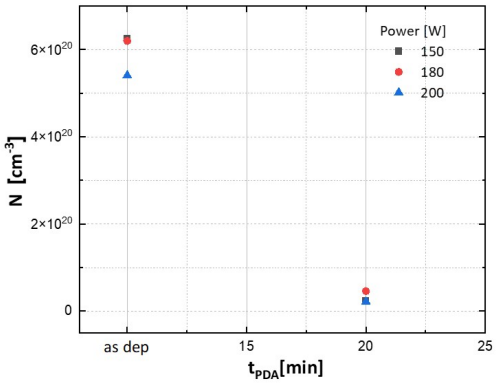

Figure 4.18: Free carriers concentration vs PDA time of IOH samples for power experimental series with p.water = 3*10^{-5} mbar.

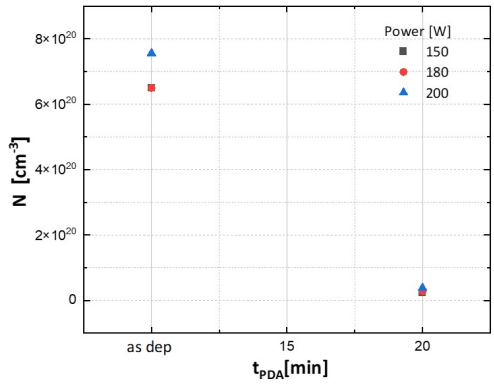

Figure 4.19: Free carriers concentration vs PDA time of IOH samples for power experimental series with p.water = 6*10^{-5} mbar.

4.2. Intrinsic Zinc Oxide (i-ZnO)

Zinc oxide (ZnO) is a semiconductor with a direct bandgap that ranges from 3.1 eV to 3.44 eV, and it is known for its excellent optical properties, with an average transmittance of 88-90% [59]. In terms of electrical properties, sputtered intrinsic ZnO (i-ZnO) typically exhibits relatively low mobility, ranging from 1 to 10 cm^2/Vs. As an undoped material, the charge carrier concentration of i-ZnO is generally in the order of 10^{18} cm^{-3} [60].

In this project, no direct investigations have been conducted on single i-ZnO. However, i-ZnO is used in bilayer configurations due to its excellent optical properties. The deposition parameters that will be used in the bilayer configurations are presented in Table 4.14, where the properties of those samples based on previous research [19], are presented in Table 4.15.

P [W]	T [°C]	d.r. [nm/sec]	p.p [mbar]
200	200	0.15	2e-3
200	400	0.15	2e-3

Table 4.14: Deposition parameters of i-ZnO.

Properties	Values with T = 200°C	Values with T = 400°C
Mobility (μ)	0.7 cm^2/Vs	1.3 cm^2/Vs
Free carriers (N)	10^{18} cm^{-3}	10^{18} cm^{-3}
Energy bandgap (Eg)	3.1 eV	3.15 eV
Avg. Transmittance (T)	85%	84%

Table 4.15: i-ZnO properties

4.3. Tin Oxide (SnOx)

SnOx is a semiconductor with a wide band gap of 3.8 eV. Due to this, it can be a good candidate for replacing i-ZnO as the transparent layer in TCOs, since this attribute allows this material to be highly transparent in the visible spectrum. Chemical and thermal stability are also two factors that should be taken into account. SnOx has the ability to remain stable under a wide range of different conditions including high temperatures and exposure to chemicals which make it suitable for for long-term use in outdoor and harsh environments,like solar cells [61].

Experiment results

In this project, temperature and power were the first varied parameters and after determining the optimal values, different gas flows, regarding mostly the oxygen role in the deposition, were varied.

Power-Temperature

Deposition Power range was between 100-250W and deposition temperature was set at 200°C and at 400°C for each different power. The gas used for this experimental series was pure argon (99% Ar) with 20 sccm flow. For the deposition rate, calculations based on previous researches [62] were conducted to achieve a thickness of 500 nm. Due to the wide power range, this experimental series was conducted in two parts, one for powers ranging from 150-250W and one for powers between 100-130W. The detailed plan can be found in Appendix D.1.

Thinckness

Thickness of the deposited samples are shown in Tables 4.16 and 4.17.

Power [W]	Thickness [nm]
150	342.5
180	414.2
200	459.7
250	504.9
100	548.6
130	501.6

Table 4.16: Thickness measurements for SnOx samples deposited at 200°C.

Power [W]	Thickness [nm]
150	336.1
180	389.6
200	435.8
250	505.4
100	505.6
130	480.4

Table 4.17: Thickness measurements for SnOx samples deposited at 400°C.

Temperature does not have a significant impact on the thickness of the deposited films, since under same power thickness results are similar. On the other hand, the deposition power plays a crucial role. At higher power levels -200 to 250 W- the thickness approaches the target value of 500 nm, while at lower power levels -150 to 180W- the thickness is reduced. As previously mentioned, the depositions at 100 W and 130 W were conducted separately. Due to the sub-optimal thickness observed at

lower power levels, adjustments were made to achieve the desired 500 nm thickness. Following these modifications, the thickness values obtained at 100 W and 130 W aligned with the expected results.

Optical Characterisation

Reflectance and Transmittance measurements results are shown in Figures 4.20 and 4.21.

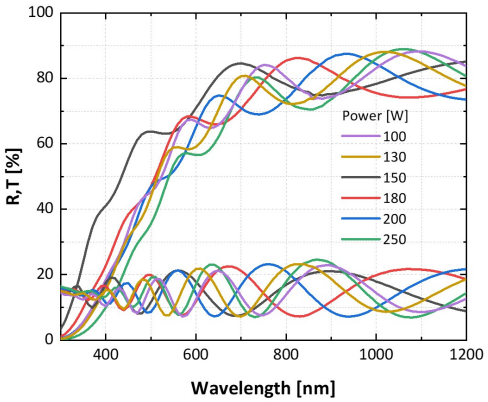

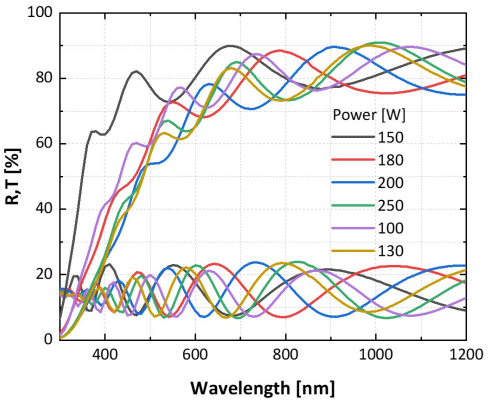

Figure 4.20: Reflectance and transmittance of SnOx samples for power experimental series at 200°C deposition temperature. **Figure 4.21:** Reflectance andtransmittance of SnOx samples for power experimental series at 400°C deposition temperature.

As observed from the figures, the optical behavior of samples deposited at different power levels is generally consistent, with the exception of the sample deposited at 150 W. Specifically, all samples begin to absorb light at wavelengths below 400 nm. Beyond this threshold, samples deposited at lower powers exhibit a higher transmittance gain. Thickness of the samples varied with higher deposition powers resulted in thicker samples. The slight increase in transmittance observed in samples deposited at lower temperatures may be attributed to their thinner profile, which allows light to pass through easier. However, the transmittance profile of all the aforementioned samples was aligned to those in other researches [62].

Samples deposited at 150 W tend to have a different behaviour. Across both deposition temperatures, but particularly at 400°C, these samples exhibited a significantly higher gain in transmittance compared to the others. It is important to note that this experiment was the first of tests involving SnOx, requiring the installation of a new target. It is assumed that residual water droplets left inside the chamber during installation could have influenced the sample's behavior. Consequently, this unexpected result suggests the necessity of conducting a new series focused on examining the effects of different gases, to better understand the observed deviation in transmittance.

The energy bandgap of the examined materials was calculated by the Tauc plot method. The results are shown in Tables 4.18 and 4.19. The Tauc plots from which those results were acquired can be found in Appendix 4.18.

Power [W]	Eg [eV]
150	3.01
180	2.5
200	2.2
250	2.03
100	2.3
130	2.23

Table 4.18: Energy bandgap values for SnOx samples deposited at 200°C.

At 200°C, the bandgap values were within the range of 2 to 2.5 eV, where at 400°C, the bandgap expanded to a range of 2.3 to 3 eV. This highlights the influence of temperature, as higher values

Power [W]	Eg [eV]
150	3.47
180	2.73
200	2.36
250	2.46
100	2.95
130	2.50

Table 4.19: Energy bandgap values for SnOx samples deposited at 400°C.

promote greater crystallization, leading to increased the values [62]. Despite this increase, the acquired values remained lower than those reported in the literature[63] -3.8 eV.

Electrical Characterisation

Mobility and free carriers concentration data are shown in Figures 4.22 and 4.23.

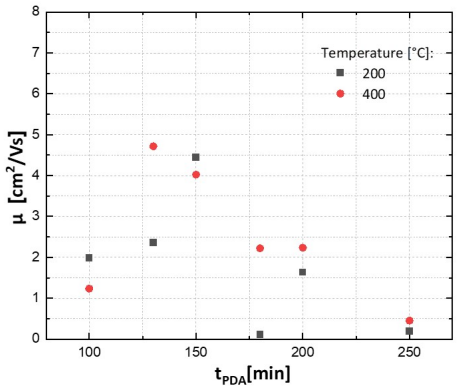

Figure 4.22: Mobility vs power of SnOx samples

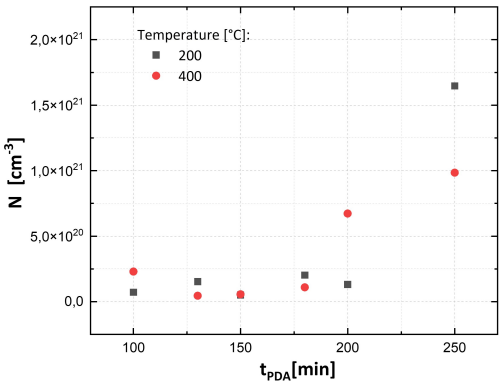

Figure 4.23: Free carriers concentration vs power of SnOx samples

The mobility values observed in this study ranged between 1 and 10 cm^2/Vs, which aligns other reports [62]. In mobility there was no significant difference between the two different deposition temperatures at each power level. It was observed that mobility peaks at power levels between 130 and 150 W, after which it declines and stabilizes within the range of 1 to 2 cm^2/Vs. For the free carriers concentration, the magnitude ranges from 10^{19} to 10^{20} cm^{-3}. Specifically with rising power the concentration increased, meaning that lower power is better for the electrical properties.

Different gasses

In most studies involving SnOx, the films have been deposited using O_2/Ar gas [64] [65]. Based on these results, 3 different gases were tested, pure Ar (99% Ar), a combination of pure Ar (99% Ar) with O_2/Ar and only O_2/Ar. In both three scenarios the total flow was maintained at 20 sccm. Since 400°C depositions provided better results, it was chosen and kept this values during the experiments. Same for power, since it provides better results at lower values, a smaller range between 130-170W was chosen. All the other parameters were kept as in the previous experimental series. The complete deposition plan can be found in Appendix D.2.

Thickness

The thickness of the new deposited samples is shown in Table 4.20. Thickness of all the samples are aligned with the value that was expected (500 nm) leading to the conclusion that the deposition rates used for each gas was correct.

Power [W]	Thickness [nm]	Former gas
130	485.0	99% Ar
150	480.2	99% Ar
170	475.8	99% Ar
130	525.4	Ar - O_2
150	494.3	Ar - O_2
170	487.0	Ar - O_2
130	492.1	99% Ar / Ar - O_2
150	466.6	99% Ar / Ar - O_2
170	478.1	99% Ar / Ar - O_2

Table 4.20: Thickness measurements for SnOx samples for power series and different gasses experiments.

Optical Characterisation

The initial aspect that must be examined is the transmittance curve of the samples across all gas compositions. The transmittance curves for the samples deposited under pure argon (99% Ar) are presented in Figure 4.24.

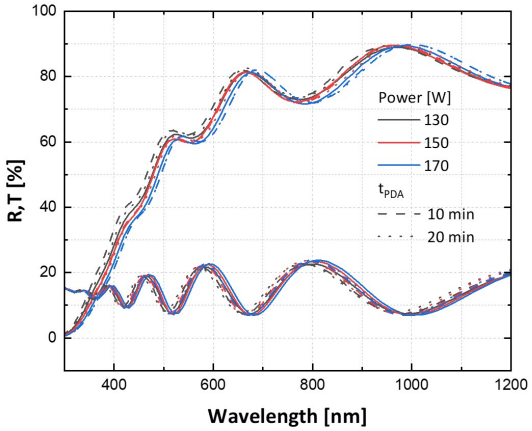

Figure 4.24: Reflectance and transmittance of SnOx samples deposited at varied powers using pure argon gas

All samples deposited using this gas exhibit behavior consistent with that observed in the first deposition series. The previously noted extra gain in the UV region is absent, indicating that the odd behavior of the sample deposited at 150 W was not attributed to the power level, but due to other reasons.

To investigate whether oxygen is responsible for this behavior, transmittance curves for the samples deposited using the other two gas mixtures -both including portion of oxygen- are presented in Figures 4.25 and 4.26.

In those figures, the gain in the UV region significantly increases when oxygen is introduced during deposition. In fact, the behavior of the odd sample from the first deposition series closely aligns with these curves, supporting the hypothesis that the presence of water residues in the chamber during the first deposition have influenced the observed results.

Increasing the oxygen flow during deposition can significantly enhance the optical properties of the samples. A higher oxygen flow ensures that the stoichiometric balance of the SnOx film is maintained, minimizing the occurrence of non-stoichiometric regions that could act as scattering centers. Furthermore, better stoichiometry reduce the oxygen vacancies. Oxygen vacancies in SnOx serve as donor defects that introduce free electrons into the conduction band, which can absorb and scatter light, thereby hurting material's transparency. The stoichiometric balance leads to a more uniform and transparent film, improving the overall optical quality of the material.

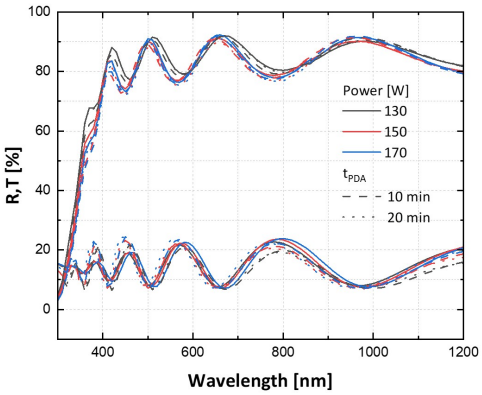

Figure 4.25: Reflectance and transmittance of SnOx samples deposited at varied powers using gas combination of pure argon and argon-oxygen

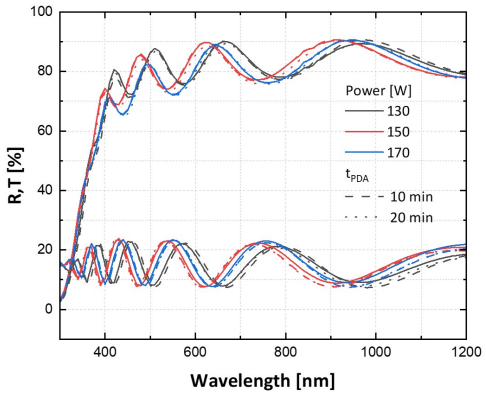

Figure 4.26: Reflectance and transmittance of SnOx samples deposited at varied powers using argon-oxygen gas

Figures 4.25 and 4.26 also show that power levels used in this series generally provide good transparency. Power of 130 W is the best-performing one, as it demonstrates a higher gain in transparency in all gas compositions. Comparing the two gas mixtures, the best results were obtained with the combination of pure argon and argon-oxygen gases. As previously mentioned, higher oxygen levels reduce the number of free carriers by filling more vacancies. However, this experiment revealed that there is a limited portion of oxygen that should be introduced. This underscores the importance of carefully controlling the oxygen flow to achieve the desired optical properties.

The energy bandgap results are presented in Figure 4.27. In previous researches it has been reported that there is a systematic increase in the band gap with decreasing sputtering power. Furthermore, based on the previous data, 130 W seems to be the optimal deposition power. Thus, figure presents only samples deposited at this power.

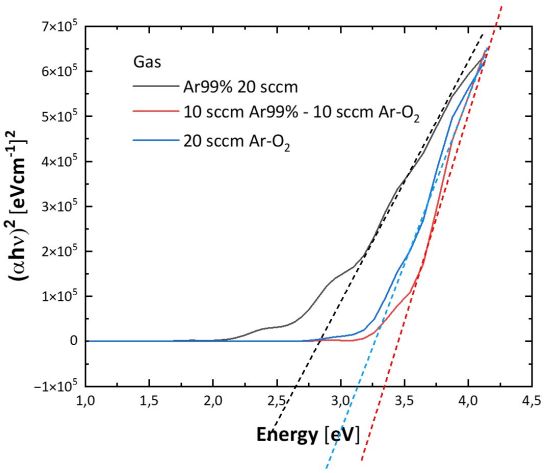

Figure 4.27: Energy bandgap of SnOx samples deposited at 130 W using different gases.

The introduction of oxygen during deposition leads to an increase in the energy bandgap, rising from approximately 2.65 eV to 3.4 eV. Furthermore, favorable results are achieved when the gas mixture includes both pure argon and an argon-oxygen. This underscores the importance of precisely controlling the oxygen flow to optimize the material properties.

The role of oxygen in this context can be attributed to its ability to reduce vacancies and defects within the material. Oxygen vacancies and other defects are known to introduce states within the bandgap,

which can lower the effective bandgap by providing intermediate energy levels for electronic transitions. By increasing the oxygen flow, these defect states are diminished, resulting in a cleaner band structure and a higher bandgap. In other studies, the extrapolation of Tauc plots has provided bandgaps ranging from 3.4 eV to 3.6 eV [62]. Project's results with a maximum of 3.4 eV are in excellent agreement with those researches.

Electrical Characterisation

Mobility values and free carriers concentration results of those depositions are presented in Figure 4.28.

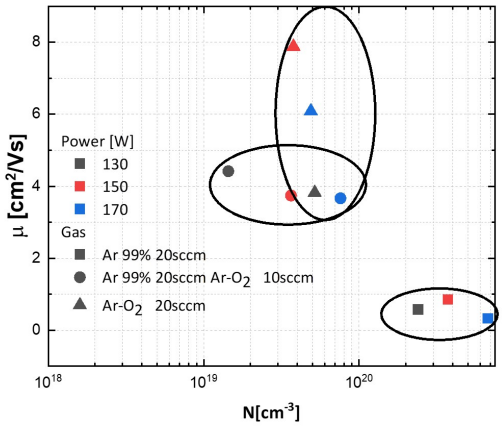

Figure 4.28: Mobility vs free carrier concentration using different powers and gasses.

Again the addition of oxygen during deposition significantly enhances those properties. Free carriers concentration decreased by an order of magnitude, from 10^{20} to 10^{19} cm^{-3}. As for mobility, it increased from 1 cm^2/Vs to 4-8 cm^2/Vs when oxygen is used in the gas configurations.

In terms of power, when argon-oxygen were used, power variations had a slight impact on mobility, with the highest mobility of 8 cm^2/Vs observed at 150 W. In the other two cases, variations did not significantly affect mobility but they did influence free carriers concentration. Lower power levels associated with fewer free carriers.

XRD

In Figures 4.24, 4.25 and 4.26 a dashed line is appeared in every curve. Those lines represents the curves after 10 minutes of PDA treatment. All of those curves did not differ from the as deposited curves, meaning that this treatment does not affect the samples. To verify that, XRD measurements are taken. Figure 4.29 represents the SnOx sample deposited using the combination of pure argon and argon-oxygen gases.

As evidenced by the figure, there is no significant difference between the as-deposited and annealed conditions of the SnOx material. In both states, the SnOx samples exhibit three distinct diffraction peaks, which represent the preferred crystallographic orientations. Those peaks are clear under both conditions, indicating a high degree of crystallinity.

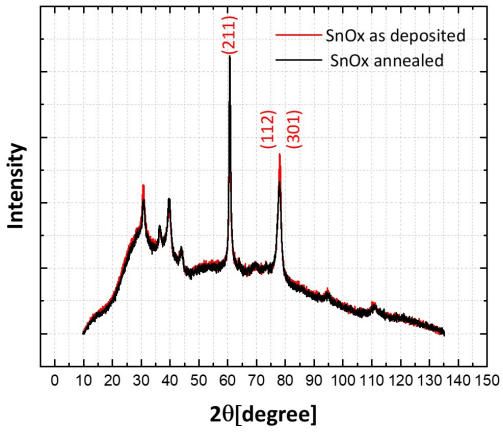

Figure 4.29: XRD of SnOx sample deposited at 130 W using the gas combination of pure argon and argon-oxygen

4.4. Materials Summary

In this section, a summary of the opto-electrical characteristics of the materials discussed above will be provided. Only the complete set of properties from the best-performing sample in each case will be presented, ensuring that values from different experimental series are not mixed.

Regarding optical properties, the average transmittance and energy bandgap are presented in Table 4.21.

	ITO	ICO	IOH	i-ZnO	SnOx
Avg T [%]	84-85	80-82	81-82	83-84	82-83
Eg [eV]	3.3-3.4	3.4-3.5	3.6-3.65	3.1-3.15	3.3-3.4

Table 4.21: Comparison of average transmittance and energy bandgap values for different TCO materials.

All the materials exhibit similar average transmittance, highlighting their strong optical properties. However, it is important to note that SnOx and i-ZnO samples have significantly greater thicknesses—ranging from 500 to 1000 nm, compared to the 100 nm thickness of the other materials. Given that their transmittance remains comparable despite the increased thickness, these materials demonstrate superior performance in their role as transparent conductors.

In terms of energy bandgaps, IOH overperforms among the first three materials. Meanwhile, SnOx surpasses i-ZnO, suggesting its considerable potential as a substitute for i-ZnO in certain applications.

While average transmittance is an important factor, it is essential to consider additional properties, such as the absorption factor at higher wavelengths. This is linked to the free carriers concentration as described by equation 2.16. Therefore, a comprehensive evaluation of the electrical properties must also be considered to fully assess the performance of these materials.

In Figure 4.30, the mobility versus free carriers concentration plot for the examined TCO is presented. In this figure, the blue curves of the scattering mechanisms described in chapter 2.5.1 are also presented, in order to help explaining the limitations of the single layers.

One primary objective of TCO is to achieve the highest possible mobility, in order to achieve high conductivity. However, it is also important to maintain its transparency. According to equation 2.16, a reduction in free carrier concentration leads to a lower absorption coefficient, resulting in less light absorption and increased transparency.

Based on these, the optimal performance for TCOs is represented by being in the top left corner of Figure 4.30, where the balance between high mobility and low free carriers concentration yields the most desirable combination.

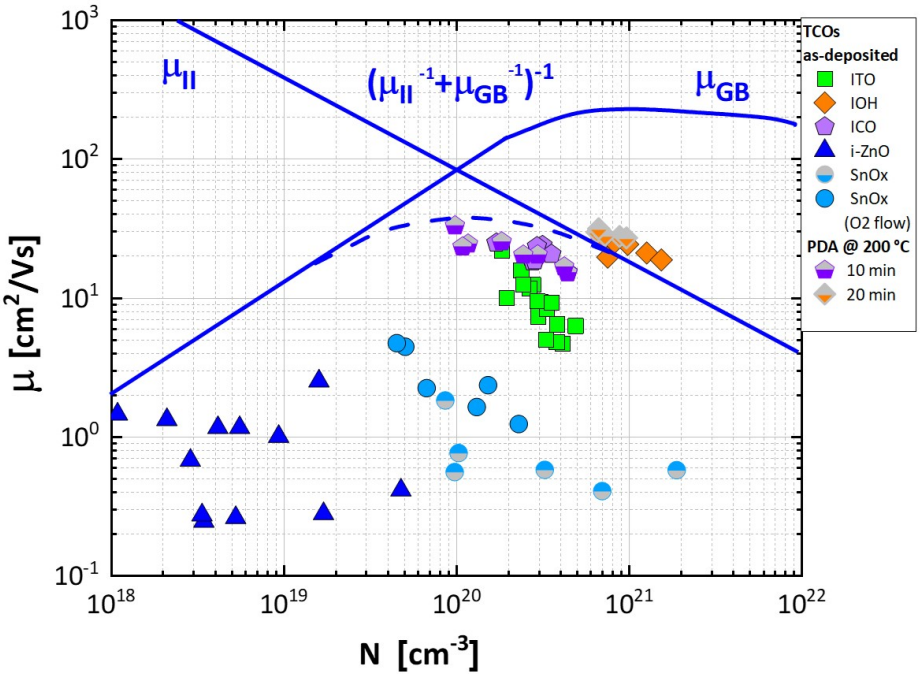

Figure 4.30: Mobility vs free carriers concentration for single TCOs

The doped indium oxide materials (IOH, ICO, and ITO) achieve superior mobility. However, this advantage in mobility comes at the cost as these materials are characterized by significantly higher carriers concentrations. ICO and IOH achieve greater mobility than ITO. Regarding IOH, the limitation by ionized impurities can be clear from the graph.

In contrast, i-ZnO demonstrates better performance in terms of free carriers concentration, which is an order of magnitude lower than that of the other materials. However, its mobility lags behind the indium oxide-based materials.

SnOx material, occupies an intermediate position between these two clusters, achieving balanced performance in both mobility and free carrier concentration. When oxygen gas is present during depositions, the overall performance of SnOx is enhanced.

Regarding PDA treatment, when it is applied to the doped indium oxide materials their performance is enhanced, underling its effectiveness.

The graph clearly illustrates that scattering mechanisms impose limitations on mobility across the spectrum. In materials with lower free carriers concentrations, reduced mobility is observed, while in the higher mobility category, the accompanying increase in free carriers concentration further highlights the trade-off between these two critical properties.

The objective of the upcoming bilayer configurations is to determine whether the combination of a highly transparent material, with a highly conductive one can overcome the limitations and be placed in in the top left corner of the performance graph.

5

Bilayer configuration

In this section, the bilayer configurations will be analyzed. Bilayers were fabricated using the optimal deposition parameters identified in the previous chapter. IOH and ICO were employed as the conductive materials, while i-ZnO and SnOx were used as the transparent layers. In each configuration, the conductive material was deposited first, followed by the deposition of the transparent layer. As demonstrated in the previous chapter, PDA treatment significantly enhances many of the materials' properties. Consequently, this procedure was also applied to the bilayers. The bilayer samples were subjected to post-deposition annealing treatment in ambient environment for 140 minutes at 200°C. The annealing time and temperature were optimized by previous research [19]. The last step is to compare the opto-electrical properties of the bilayers deposited on flat glass substrates, with those on textured glass. Identical depositions were conducted on the textured substrates for the correct comparison.

5.1. Flat glass substrates

5.1.1. ICO-ZnO

The first configuration will is ICO with i-ZnO. The parameters that are varied are the thickness of the ICO, ranging from 50nm to 150nm, and the deposition temperature of the i-ZnO being 200 and 400 °C. All the other deposition variables are based on the previous examination in Chapter 4. The four different combinations are presented in Table 5.1. The exact deposition plan can be found in Appendix E.1.

Samples	ICO thickness [nm]	ZnO T [°C]
S1	50	200
S2	50	400
S3	100	200
S4	100	400

Table 5.1: Deposition parameters for ICO/i- ZnO bilayer in flat glass substrate.

Experiment results

The first examination will be the thickness of the samples. Since we deal with bilayers the measurement of the thickness will be done by Scanning Electron Microscopy (SEM). Pictures taken by SEM are presented in Figure 5.1.

The different layers are clear in the image, thus the thickness measurement can be applied. Measurements were taken in multiple spots in order to have a well established value and avoid measurement errors. In the picture presented, the sample is S1 -with expected thicknesses of 50 nm for ICO and 1000 nm for i-ZnO. The thickness of i-ZnO is measured at 780 nm where the expected thickness was 1000 nm. What is more important is the thickness of the ICO. It is measured at 65 nm compared to the expected 50 nm. The accuracy of the deposition is acceptable. According to those results, it is safe to

assume that the deposition of samples S3 and S4 will provide results with ICO thicknesses of at least 100 nm since the deposition rate was doubled.

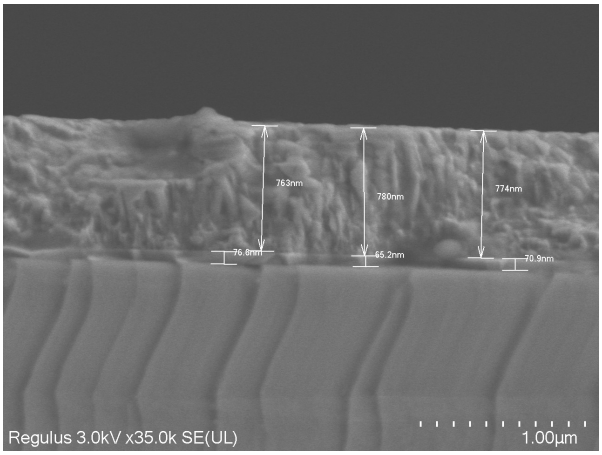

Figure 5.1: SEM picture of ICO/i-ZnO bilayer with thickness of each layer measured.

Mobility and free carriers concentration behaviours over PDA time are presented in Figures 5.2 and 5.3. In this experiment, PDA treatment was applied, and the value 10 minutes before and after the optimal annealing time -140 minutes- was also tested. This was done to verify whether 140 minutes is indeed the optimal annealing time, as well as to account for potential deviations and unexpected errors.

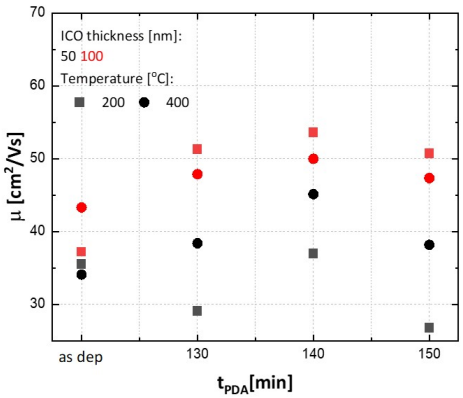

Figure 5.2: Mobility vs PDA time of ICO/i-ZnO bilayer with different thicknesses of ICO and different d.temperatures of i-ZnO. Depositions have been made in flat glass substrates.

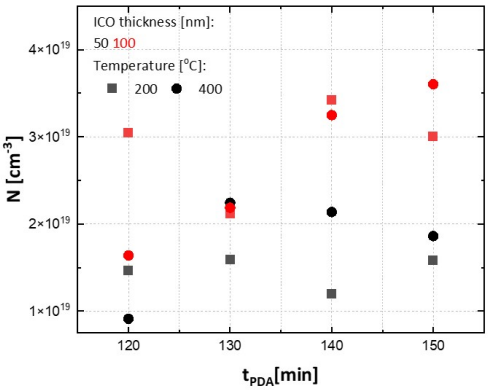

Figure 5.3: Free carriers concentration vs PDA time of ICO/i-ZnO bilayer with different thicknesses of ICO and different d.temperatures of i-ZnO. Depositions have been made in flat glass substrates.

The free carrier concentration in the bilayer is of the same order of magnitude as that of the more transparent material, i-ZnO, as indicated on the y-axis. However, a slight increase in free carriers concentration is observed across all samples as the annealing time increases. This increase remains within a relatively small range, indicating that the observed rise is not substantial enough to significantly impact the material's properties.

Figure 5.2 suggests that the excellent mobility property of ICO are effectively retained within the bilayer structure.n. In terms of PDA treatment, the results demonstrate that at 140 minutes, the highest mobility values are achieved. This confirms that PDA plays a significant role in enhancing the electrical properties and it is also reinforces that the 140-minute mark is optimal.

In Figure 5.2, samples in which the thickness of ICO is higher, present significantly higher mobility - 10 to 15 cm^2/Vs increased. As discussed in Chapter 2, mobility is a measure of the ability of electrons

to move through a material when an electric field is applied. Electrons tend to follow paths with the fewest obstacles and the least resistance. Grains, which form within the material, are responsible for disrupting electron movement, as they create regions in which the electrons cannot move easy. It is, therefore, assumed that electrons attempt to avoid these grains. As shown in Figure 5.4, it is suggested that electrons take advantage of the interface between the two materials, where grain boundaries are significantly fewer. This preferential pathway is presented by the red line.

To effectively take advantage of the interface, an adequate penetration depth must be present. If the depth is insufficient, electrons will be unable to utilize the interface between the two materials. Instead, they will primarily follow the path of least resistance, which corresponds to the more conductive material, in this case ICO. This is supported by the results shown in Figure 5.2. In samples where the ICO thickness is lower, the mobility values are closely aligned with those of the single-layer ICO material, as discussed in Chapter 4. In contrast, in samples with greater ICO thickness, the values are increased by 10-15 cm^2/Vs compared to the previous case, meaning that electrons are more likely to take advantage of the the interface, for more efficient movement of charge carriers. This interaction enhances mobility beyond the levels seen in single-layer ICO, demonstrating that the bilayer configuration can offer superior opto-electrical performance when the penetration depth is optimized.

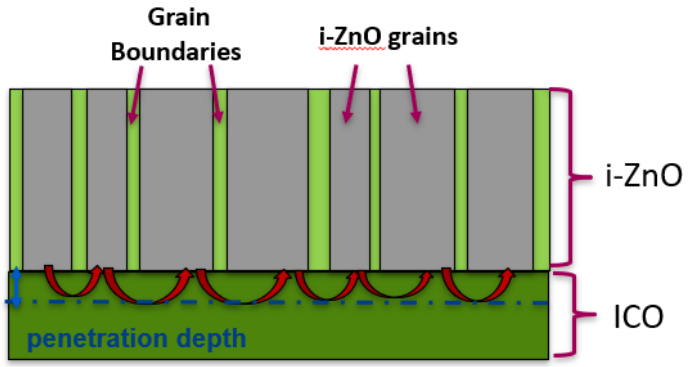

Figure 5.4: Electrons preferred path in a typical bilayer configuration.

Experiments in which the thickness of the conductive layer, ICO, reached 150 nm were also conducted. However, these experiments revealed no significant difference between samples with 150 nm and 100 nm ICO thickness. For more clarity, those results are not presented in the graphs above but can be found in Appendix E.1 and E.2. Based on these findings, it has been concluded that for all upcoming bilayer depositions, the thickness of the conductive material should be maintained at 100 nm or greater to ensure optimal performance.

Regarding the transmittance and reflectance of the bilayers, Figure 5.5 illustrates their behavior across the wavelength range of 300-1200 nm. Only samples S3 and S4, where the ICO thickness is higher, are presented, as they perform better in previous analysis. The behavior of both curves aligned with that of a single layer. However, higher fluctuation is observed across the wavelength range. This is attributed to the interface between the two materials, where increased constructive and destructive interference occurs.

i-ZnO T [°C]	As deposited		Annealed	
	Avg R [%]	Avg T [%]	Avg R [%]	Avg T [%]
200	14.6 ± 4.4	82.1 ± 8.2	14.5 ± 4.2	82.8 ± 7.2
400	13.7 ± 4.2	81.9 ± 6.5	13.7 ± 4.2	83.1 ± 6.4

Table 5.2: Average reflectance (R) and transmittance (T) across 400-1200 nm for ICO/i-ZnO samples, at different ZnO temperatures in as deposited and annealed conditions.

The high fluctuation is further confirmed by Table 5.2. The range around the mean values is higher than in the single layers, fluctuating between 6-7%, compared to 3-4% respectively. Despite this increase,

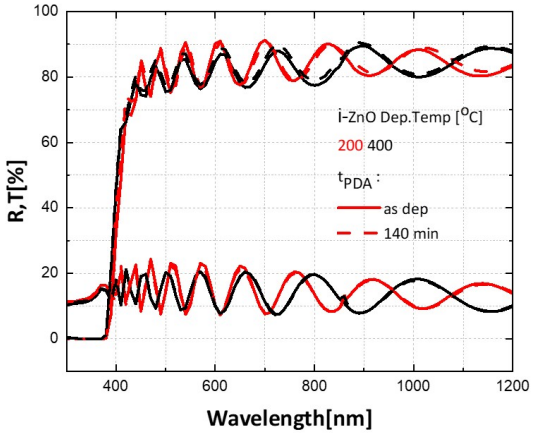

Figure 5.5: Reflectance and transmittance of ICO/i-ZnO bilayer with different thicknesses of ICO and different d.temperatures of i-ZnO. Depositions on flat glass substrates.

the average transmittance values remain consistently high, ranging from 82-83%, underlining the strong optical properties of the samples.

5.1.2. IOH/i-ZnO

The second configuration is the IOH/i-ZnO bilayer. IOH properties was chosen based on the examination in previous chapter. Thus, Power will be maintained at 150 W and partial water pressure will be set at 3 and 6e-5 mbar, since both pressures provided favorable results. Influenced from the work done in the previous configuration, the thickness of IOH was set 100 nm. For i-ZnO, as in previous deposition, only deposition temperature will be varied. The four different combinations are presented in Table 5.3 and the complete plan can be found in Appendix E.2.

Samples	IOH p.water [mbar]	ZnO T [°C]
S5	3e-5	200
S6	3e-5	400
S7	6e-5	200
S8	6e-5	400

Table 5.3: Deposition parameters for IOH/i-ZnO bilayer in flat glass substrate.

Experiment results

The thickness was measured again using SEM. The picture taken from SEM is presented in Figure 5.6. The thickness of i-ZnO is measured at 850 nm. As in the previous experiment, i-ZnO thickness is decreased from the expected value-1000 nm. This is normal since the same deposition rate was used. What is more important is that the thickness of IOH is fall down 10 nm from the expected thickness-100nm, since the benefit from the interface might be reduced.

Regarding mobility and free carriers concentration, results are presented in Figures 5.7 and 5.8.

The free carriers concentration follows the same order of magnitude as the transparent material, i-ZnO, with values around 10^{19} cm^{-3}. This indicates that the transparency of the i-ZnO layer is preserved also in this bilayer formation.

The mobility values of the bilayer are aligned with those of IOH single layer, meaning that the high conductivity is preserved. Specifically, under as-deposited conditions, the mobility values range from 28-38 cm^2/Vs.

With respect to PDA treatment, mobility increases across all four samples, emphasizing the benefits of this method. The 140-minute mark appears to be the optimal point, as values begin to decrease after

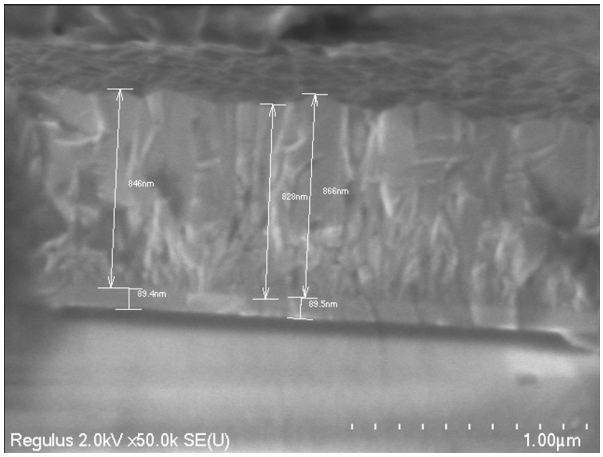

Figure 5.6: SEM picture of IOH/i-ZnO bilayer with thickness of each layer measured.

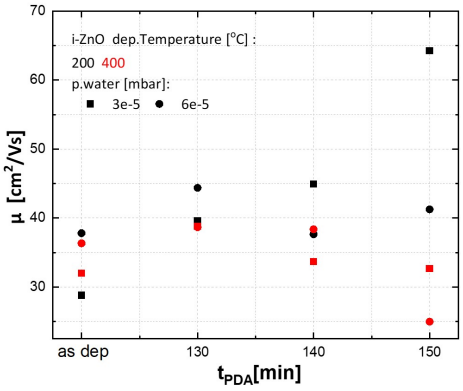

Figure 5.7: Mobility vs PDA time of IOH/i-ZnO bilayer with different p.water for IOH and different d.temperatures of i-ZnO. Depositions on flat glass substrates.

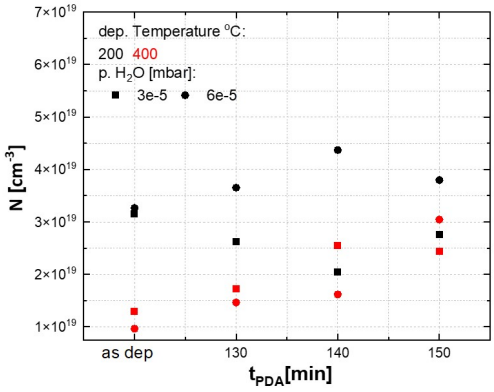

Figure 5.8: Free carriers concentration vs PDA time of IOH/i-ZnO bilayer with different p.water for IOH and different d.temperatures of i-ZnO. Depositions on flat glass substrates.

this duration. Sample S1 shows significantly higher mobility values than the other samples after 140 minutes. This behaviour is inconstant, as the trend for this sample, from as-deposited to 140 minutes of PDA treatment, follows the same behavior as the other samples.

Deposition temperature of 200°C consistently outperforms 400°C, as the mobility values are 10 cm^2/Vs higher. Although the free carriers concentration is higher at 200°C, the increase is not as high as the improvement in mobility, suggesting that 200°C is the better choice.

When comparing these results to ICO/i-ZnO configuration, the mobility values in this configuration are approximately 7-10 cm^2/Vs lower. Considering that the mobility values for single-layer IOH are even or higher than those for single-layer ICO, this decrease in the bilayer is unexpected. A potential factor contributing to this reduction could be the thinner IOH layer—89 nm. This decreased thickness may lead to a lower gain from the interface effect. However, the mobility values remain higher than those for single-layer IOH, which was 30 cm^2/Vs. This suggests that the interface theory is still valid, but a greater thickness could further enhance the overall mobility values.

For reflectance and transmittance, Figure 5.9 illustrates their behavior across the wavelength range of 300-1200 nm. For clarity, only samples S5 and S7 are presented due to their superior mobility values. Similar to the previous configuration, it can be observed that the behavior of the curves aligns with that of a single layer, with the exception of greater fluctuation across the wavelength range.This fluctuation is again attributed to the interface between the two materials.

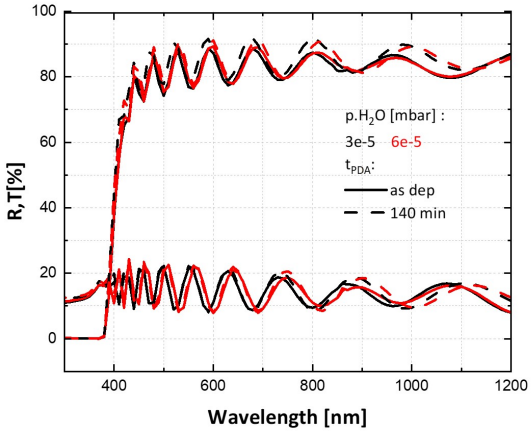

Figure 5.9: Reflectance and transmittance of IOH/i-ZnO bilayer with different d.temperatures of i-ZnO. For IOH: p.water=3e-5mbar. Depositions on flat glass substrates.

p.H_2O [mbar]	As deposited		Annealed	
	Avg R [%]	Avg T [%]	Avg R [%]	Avg T [%]
3×10^{-5}	14.1 ± 3.8	81.4 ± 7.1	14.6 ± 4.1	83.4 ± 6.5
6×10^{-5}	13.7 ± 4.3	83.2 ± 6.3	13.9 ± 4.3	83.1 ± 6.3

Table 5.4: Average reflectance (R) and transmittance (T) across 400-1200 nm for IOH/i-ZnO samples in as deposited and annealed conditions.

The fluctuation is confirmed by Table 5.4. Additionally, the high values of average transmittance are further emphasizing the excellent transparency of the materials.

5.1.3. IOH/SnOx

The final configuration involves a bilayer of IOH and SnOx. The deposition parameters for IOH were kept consistent with previous configurations, with the exception of the partial water pressure. The value of 3e-5 mbar for partial water pressure value was selected for the current configuration. For SnOx, the deposition conditions involved 130W power and a gas mixture of argon and argon/oxygen. The complete experimental plan is outlined in Table 5.5.

P [W]	T [°C]	thickness [nm]	p.p [mbar]	p. water [mbar]	Gas [sccm]
IOH					
150	25	100	5.7e-3	3e-5	Ar [40]
SnOx					
130	400	500	2.6e-3	-	Ar/Ar-O_2 [10/10]

Table 5.5: Deposition parameters for IOH and SnOx layers for bilayer configuration.

Experiment results

Regarding thickness, SEM picture is presented in Figure 5.10. For SnOx, the thickness is measured around 350 nm, again around 150 nm less than the expected thickness. For the conductive layer, IOH, thickness is measured at 85 nm, 15 nm less than the expected thickness. This decrease as in previous configurations, is more significant than the one of he transparent layer, since it might cause problems regarding the interface effect.

Mobility and free carriers concentration results are presented in Figures 5.11 and 5.12. Two samples with the same properties were examined for further accuracy. It is observed that both samples presented same behaviours, leading to the conclusion that indeed the values measured are verified.

For as deposited conditions, free carriers are in the same order of magnitude as this of SnOx single

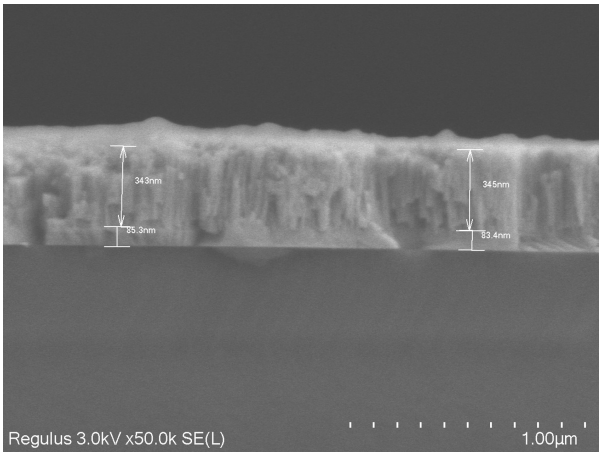

Figure 5.10: SEM picture of IOH/SnOx bilayer with thickness of each layer measured.

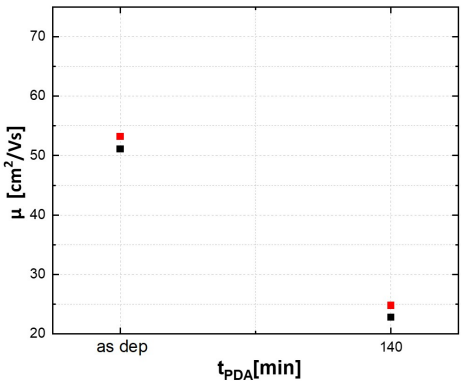

Figure 5.11: Mobility vs PDA time of IOH/SnOx bilayer. Depositions on flat glass substrates.

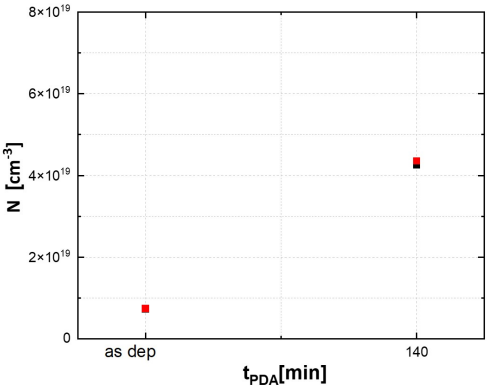

Figure 5.12: Free carriers concentration vs PDA time of IOH/SnOx bilayer. Depositions on flat glass substrates.

layers - 10^{19} cm^{-3}. This verifies that the advantage of the transparent layer is transferred also in this configuration. Regarding, mobility, it is observed that the values high- at 52 cm^2/Vs. Regarding PDA time, it can be seen that after the treatment, the values in mobility have significantly decreased. This means that these materials do not follow the same trend as before, leading to the fact that further investigation regarding this method need to be assessed.

For reflectance and transmittance, Figure 5.13 illustrates the behavior across 300-1200 nm in as deposited and after PDA treatment.

The behavior of this configuration aligns with that of a single TCO layer, but with high fluctuation across the wavelength. The high transmittance values, as well as the fluctuation are verified by Table 5.6. However, the fluctuation is not as high as in samples involving i-ZnO. The reason for this may rooted to the higher roughness of the SnOx compared to i-ZnO [62]. Higher roughness is responsible for scattering light in multiple directions, removing constructive and destructive interference. The roughness of the material is not that high to remove them completely, but a lower fluctuation is observed.

	As deposited	**Annealed**
Avg R [%]	13.6 ± 4.7	14.4 ± 4.6
Avg T [%]	84.9 ± 4.3	85.1 ± 4.4

Table 5.6: Average reflectance (R) and transmittance (T) across 400-1200 nm for IOH/SnOx samples in as deposited and annealed conditions.

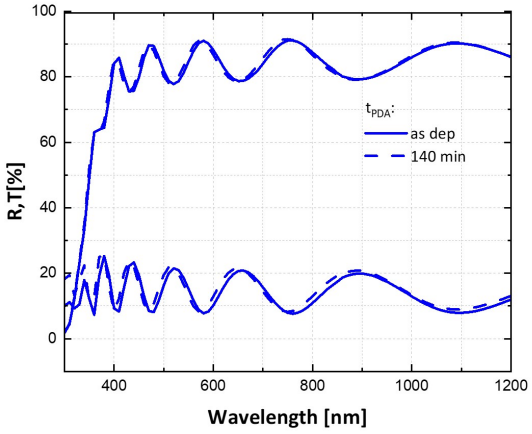

Figure 5.13: Reflectance and transmittance of IOH/SnOx bilayer. Depositions on flat glass substrates.

5.2. Textured glass substrates

Last thing that will be examined in this project is if the results of the previous bilayers can be transferred in textured glass substrates. In order to make a textured glass substrate, the method used was the modulated surface texture (MST), as described by H. Tan et al. [66]. First, a deposition of 100-200 nm ITO in a flat glass surface was made. ITO was used as a sacrificial layer for the texturing. After the deposition, the textures were generated by wet-etching of the samples in an aqueous solution composing of hydrogen fluoride (HF, 49 wt%) and hydrogen peroxide H_2O_2 (31 wt%). The volume ratio of water,hydrogen fluoride and hydrogen peroxide was 10:1:2. An example of a textured surface is presented in Figure 5.14.

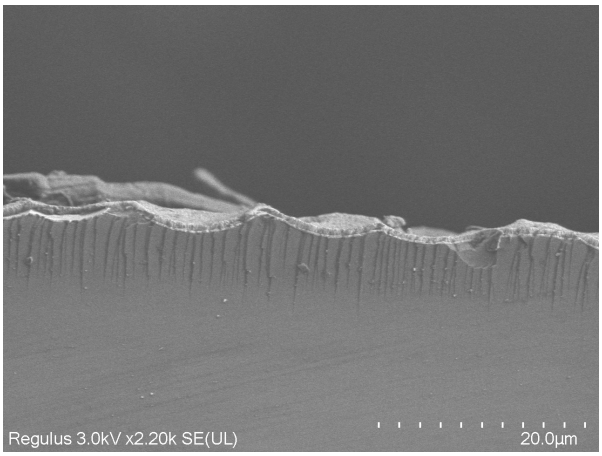

Figure 5.14: Example of textured surface. Picture taken using SEM.

5.2.1. ICO/i-ZnO

The first textured configuration is the ICO/i-ZnO bilayer. In this deposition, the thickness of the i-ZnO layer will be reduced to 750 nm, For the ICO layer, a thickness of 100 nm will be used, based on the findings from previous investigation. All other parameters will remain unchanged from those used on flat glass substrates to ensure accurate comparison. The deposition plan is presented in Table 5.7.

Experiment results

In Figure 5.15, the picture taken from SEM is presented. The thickness of i-ZnO is measured around 610 nm. As in flat glass depositions, the thickness is decreased -around 150 nm- compared to the expected one, meaning that an extra adjustment in the deposition rate has to be made. Regarding

Sample	P [W]	T [°C]	thickness [nm]	p.p [mbar]
ICO				
S1	60	25	100	3e-3
S2	60	25	100	3e-3
i-ZnO				
S1	200	200	750	2.6e-3
S2	200	400	750	2.6e-3

Table 5.7: Deposition parameters for ICO/i-ZnO bilayer in textured glass substrate.

ICO, its thickness is measured around 150 nm. Compared to the thickness measured in flat glass substrate-around 140 nm- the two measurements are accurately aligned. Furthermore, the thickness is sufficient enough for the interface effect.

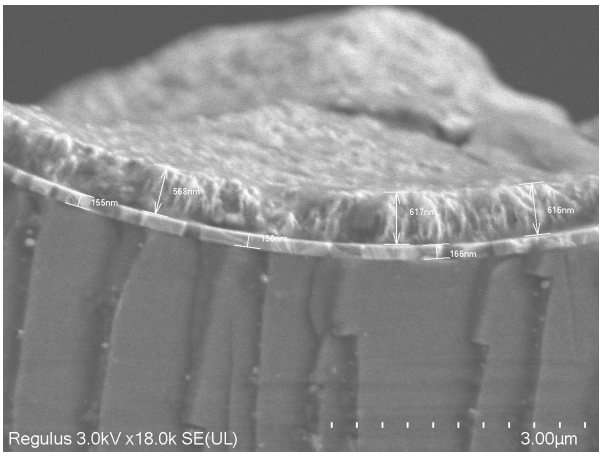

Figure 5.15: SEM picture of ICO/i-ZnO bilayer with thickness of each layer measured.

Mobility and free carriers concentration results are presented in Figures 5.16 and 5.17.

Due to a mistake during the experiment, as deposited values were not acquired. However, regarding the values after PDA, it is visible that the trend that is followed is perfectly aligned with that of the flat glass substrates. Specifically, the mobility values are between 30-50 cm^2/Vs with samples deposited at 200°C again performing better. On the other hand, results of free carrier concentration are increased compared to those of flat glass substrates- from 4 $\times 10^{19}$ cm^{-3} to 8$\times 10^{19}$ cm^{-3}. However, they are still clustered in the same order of magnitude.

For reflectance and transmittance, Figure 5.18 illustrates the behavior across 300-1200 nm in as deposited and after PDA treatment.

The behavior of the curves is aligned with this of a single layer, with the key difference being that the fluctuations are significantly reduced. This indicates that constructive and destructive interference have been largely eliminated. Referring to the IOH/SnOx configuration, where material roughness was responsible for reducing interference, a similar effect is observed here. However, in this case, it is not the material's inherent properties but the surface texturing that plays a crucial role. The high degree of texturing causes increased light scattering, which effectively removes interference patterns. This absence of fluctuations is also a clear indication of the success of the texturing method.

i-ZnO T [°C]	As deposited		Annealed	
	Avg R [%]	Avg T [%]	Avg R [%]	Avg T [%]
200	15.4 ± 2.2	82.4 ± 2.1	15.04 ± 1.9	82.7 ± 2.4
400	15.1 ± 1.6	83.6 ± 1.8	14.8 ± 1.7	83.6 ± 2.6

Table 5.8: Average reflectance (R) and transmittance (T) across 400-1200 nm for ICO/i-ZnO samples, in as deposited and annealed conditions.

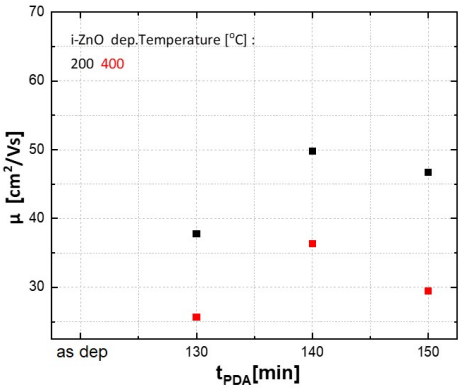

Figure 5.16: Mobility vs PDA time of ICO/i-ZnO bilayer with different d.temperatures of i-ZnO. Depositions on textured glass substrates.

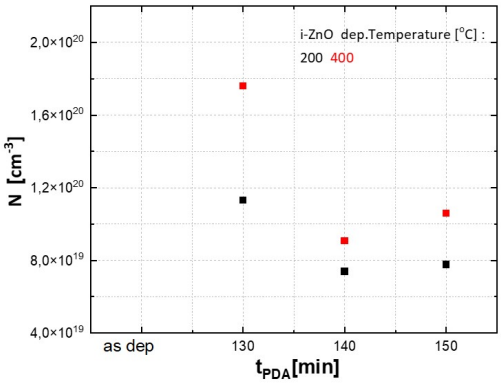

Figure 5.17: Free carriers concentration vs PDA time of ICO/i-ZnO bilayer with different d.temperatures of i-ZnO. Depositions on textured glass substrates.

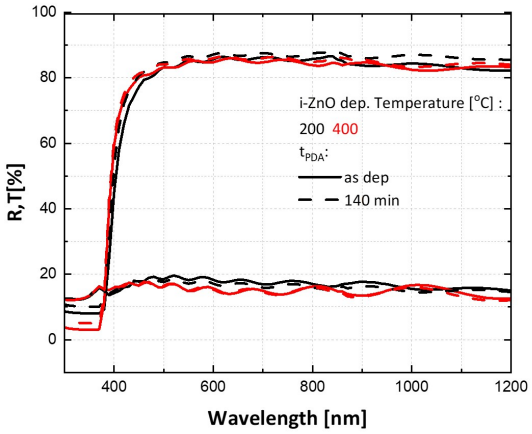

Figure 5.18: Reflectance and transmittance of ICO/i-ZnO bilayer with different d.temperatures of i-ZnO. Depositions on textured glass substrates.

Mean values and the fluctuations are presented in Table 5.8. It is clear also numerically that the fluctuations are indeed decreased. Furthermore, mean values are aligned with those in flat glass substrates, underlying the good optical properties.

5.2.2. IOH/i-ZnO

The second bilayer configuration is the IOH/i-ZnO. Again the thickness of i-ZnO is estimated at 750 nm, as in previous deposition, where for IOH it is estimated at 150 nm . Since the thickness is higher than 100 nm, it is assumed that the electrical properties will not be harmed.

Experiment results

In Figure 5.19, the picture taken from SEM is presented. Thickness of i-ZnO this time is measured at 850 nm, closer to the estimated value. Still there is a difference between the estimated and the experimental thickness which means further optimisation is needed. IOH thickness was measured at 150 nm, closely aligned with the estimated value.

Mobility and free carriers concentration are presented in Figures 5.20 and 5.21.

Regarding free carriers concentration, values are once more higher in the textured substrates compared to the flat ones. Free carriers concentration reaching values ranging around 8×10^{19} cm^{-3}, exactly as

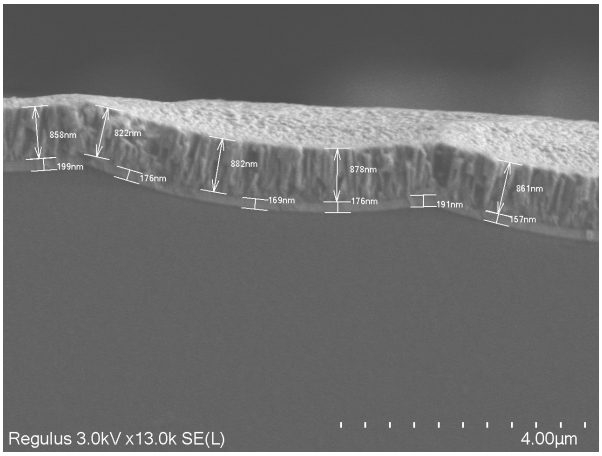

Figure 5.19: SEM picture of IOH/i-ZnO bilayer with thickness of each layer measured.

in the previous ICO/i-ZnO configuration.

For reflectance and transmittance, Figure 5.22 illustrates the behavior across 300-1200 nm in as deposited and after PDA treatment.

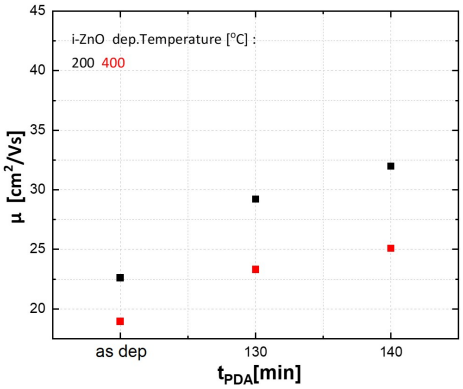

Figure 5.20: Mobility vs PDA time of IOH/i-ZnO bilayer with different d.temperatures of i-ZnO. Depositions 0n textured glass substrates.

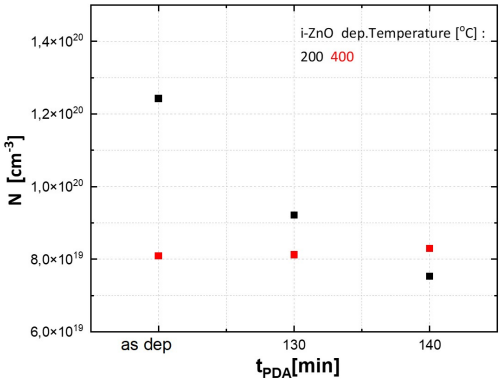

Figure 5.21: Free carriers concentration vs PDA time of IOH/i-ZnO bilayer with different d.temperatures of i-ZnO. Depositions on textured glass substrates.

i-ZnO T [°C]	As deposited		Annealed	
	Avg R [%]	Avg T [%]	Avg R [%]	Avg T [%]
200	12.9 ± 1.4	81.9 ± 3.4	13.9 ± 1.8	83.4 ± 3.8
400	13.7 ± 2.6	83.3 ± 2.5	13.9 ± 2.8	83.2 ± 2.7

Table 5.9: Average reflectance (R) and transmittance (T) across 400-1200 nm for IOH/i-ZnO samples, in as deposited and annealed conditions.

As in the previous textured configuration, the fluctuations are significantly reduced. This underlines again the effect of texturing, causing the significant elimination of constructive and destructive interference. Average values of transmittance maintained high, perfectly aligned with those of flat glass substrates, as it is shown in Table 5.4.

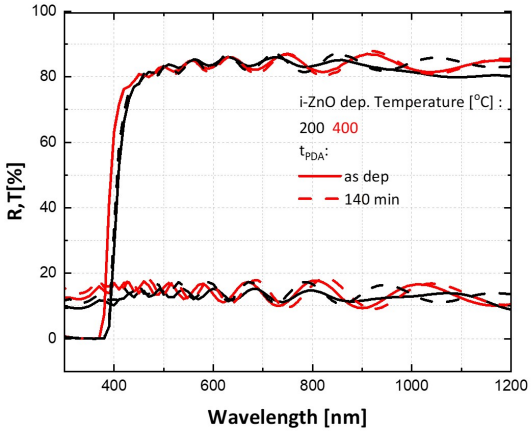

Figure 5.22: Reflectance and transmittance of IOH/i-ZnO bilayer with different d.temperatures of i-ZnO. Depositions on textured glass substrates.

5.2.3. IOH/SnOx

The last configuration of the project will be the IOH/SnOx bilayer in a textured surface. The same deposition plan that was shown in Table 5.5 and used for the flat glass substrate was performed also here. The complete plan can be found in Appendix E.3.

Experimental results

In Figure 5.23, the picture taken from SEM is presented. Thickness of i-SnOx is measured at around 550 nm, closely aligned with the expected value. Thickness of this bilayer was the closest to the expected one, meaning that this deposition rate was indeed the optimal one. Thickness of IOH was measured at 130 nm, slightly higher than the expected thickness, but still enough to get advantage of the interface effect.

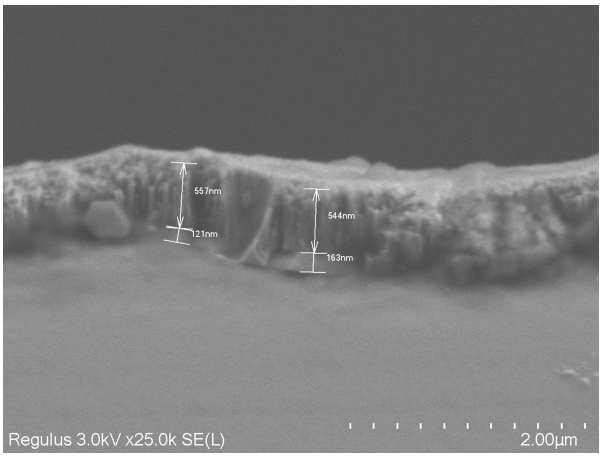

Figure 5.23: SEM picture of IOH/SnOx bilayer with thickness of each layer measured.

Mobility and free carriers concentration results are presented in Figures 5.24 and 5.25. To verify the accuracy of the measurements, 2 samples- both deposited at the same conditions- was measured. Both of them provided same results, underling the accuracy of the measurements.

Regarding as deposited conditions, free carriers are in the same order of magnitude as this of the flat glass substrates - 10^{19} cm^{-3}. Regarding, mobility, high values are reached again, going even at 60 cm^2/Vs which are the highest values obtained amongst all configurations. These high values are aligned with those of the flat glass substrates, leading to the fact that when this bilayer configuration is used, the best electrical properties are achieved. Regarding PDA time, again the values are decreased

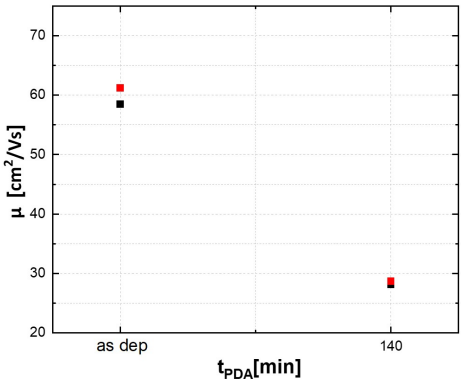

Figure 5.24: Mobility vs PDA time of IOH/SnOx bilayer. Depositions on textured glass substrates.

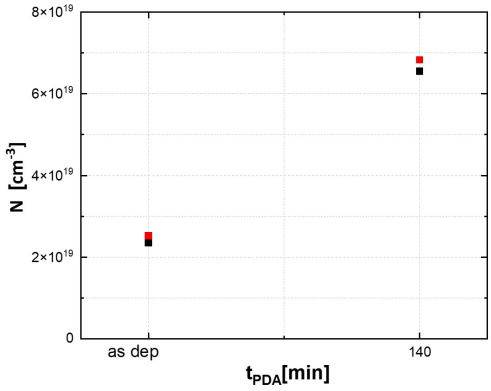

Figure 5.25: Free carriers concentration vs PDA time of IOH/SnOx bilayer. Depositions on Textured glass substrates.

significantly, addressing once more the need for further investigation when the new material- SnOx- is used.

For reflectance and transmittance, Figure 5.26 illustrates the behavior across 300-1200 nm in as deposited and after PDA treatment. The behavior of this curve is aligned with that of the flat glass substrate. However, it was expected that the fluctuations will be removed. The reason behind this expectation was based in the higher roughness of SnOx compared to i-ZnO. Adding also the textured surface of the examined samples, it was expected that the decrease of the fluctuations would have been high. Despite that, the mean values sustained high also in this configuration, as it can be seen from Table 5.10.

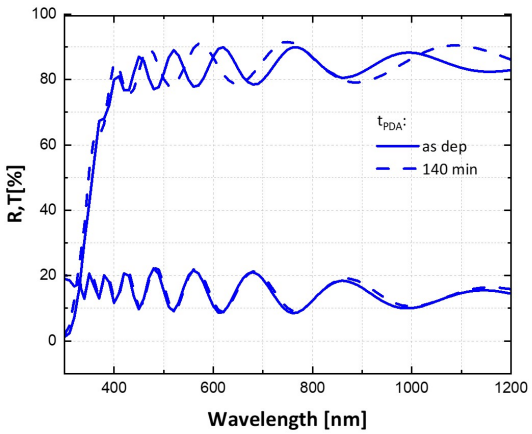

Figure 5.26: Reflectance and transmittance of IOH/SnOx bilayer. Depositions on textured glass substrates.

	As deposited	Annealed
Avg R [%]	14.4 ± 3.7	14.9 ± 3.7
Avg T [%]	83.9 ± 3.5	83.4 ± 2.7

Table 5.10: Average reflectance (R) and transmittance (T) for IOH/SnOx samples in textured substrate.

5.3. Bilayer Summary

In this section, following the same procedure as in the single layers investigation, a summary of the characteristics of the bilayer configurations will be presented. For each configuration, the properties of the best performing sample will be provided.

Regarding optical properties, the average transmittance across 400-1200 nm wavelength range of all bilayers are presented in Table 5.11. Furthermore, in this table also the average absorption of the bilayers across 1100-1200 nm was calculated. The calculation was based on equation 3.1. The choice of the wavelength range was based on 2.7, since this is the region where the high transmittance stops.

Flat glass substrates			
	ICO/i-ZnO	**IOH/i-ZnO**	**IOH/SnOx**
Avg T [%]	82.8 ± 7.2	83.9 ± 6.3	84.9 ± 4.3
Avg A [%]	1.78 ± 0.1	1.1 ± 0.2	2.41 ± 0.2
Textured glass substrates			
	ICO/i-ZnO	**IOH/i-ZnO**	**IOH/SnOx**
Avg T [%]	82.7 ± 2.4	83.4 ± 3.8	83.9 ± 3.5
Avg A [%]	1.09 ± 0.2	2.55 ± 0.4	2.11 ± 0.3

Table 5.11: Average transmittance (T) - across 400-1200 nm - and absorption (A) - across 1100-1200nm - for all bilayer configurations.

Regarding average transmittance values, the values across all bilayers are high. Having in mind that the thickness of those samples are significantly higher than single layers, the high values underling their good optical properties. In flat glass substrates, the fluctuations are high, an effect attributed to the interference between the layers. In textured surfaces fluctuations are significantly reduced, since the new surface structure removes the previous effect. This leads to smoother curves and better light utilization in the the whole wavelength range. Specifically, bilayers including SnOx have much lower fluctuations in flat glass substrates. As mentioned, this was attributed to the nature of the material. The higher roughness leads to surfaces which remove the aforementioned effect.

For the average absorption it can be seen that it is kept in really low levels. In order to have reference values, the absorption values of the single layers examined in Chapter 4 are presented in Table 5.12. It is reminded that, thickness of metal oxides are in the order of 100 nm where for SnOx around 500 nm. Thus, the values for ICO and IOH are much higher when compared with SnOx.

	ICO	**IOH**	**SnOx**
Avg A [%]	2.33$\pm$0.2	1.46$\pm$0.1	2.65$\pm$0.1

Table 5.12: Average ICO, IOH and SnOx absorption values across 1100-1200 nm.

Table 5.11 suggests that even if the thickness of the bilayers is significantly increased to this of a single layer, the absorption is decreased. The reason for this is the significant decrease of the free carriers concentration, which are mainly responsible for the absorption in this wavelength range. To have a better insight, Figure 5.27 is presented.

The performance results for both single layers and bilayers are presented. For bilayers deposited on flat glass substrates, data are reported for both the as-deposited and annealed conditions. For bilayers deposited on textured glass substrates, the optimal results for each configuration are provided.

Bilayers deposited on flat glass substrates demonstrate significantly superior performance compared to any single-layer configurations. These bilayers consistently cluster in the high mobility and low free carrier concentration range- 10^{19} cm^{-3}. Bilayer structures tend to combine the advantageous properties of each individual layer: the conductive layer contributes high mobility, while the transparent layer provides low free carriers concentration.

Furthermore, bilayers exhibit the ability to surpass the limitations imposed by grain boundaries. This behavior is attributed to the interface effect. The presence of the interface allows free carriers to bypass the grain boundaries in the transparent layer, enhancing charge transport.

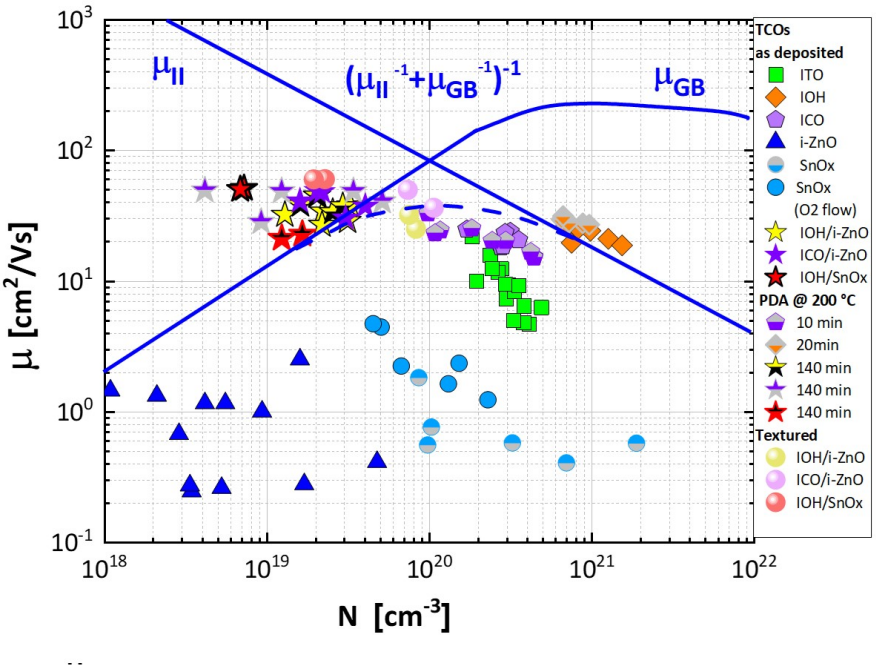

Figure 5.27: Mobility vs free carriers concentration for all TCOs

Regarding the PDA treatment, this method enhances the properties of layers involving ZnO, since an increase in mobility is observed. However, in the case of bilayers containing SnOx, the PDA process requires further optimization, as the post-treatment results are worse than those in as deposited conditions.

When comparing bilayers deposited on textured and flat substrates, the mobility remains within a similar range. This indicates that the interface effect is preserved even in textured configurations. However, a significant reduction in free carrier concentration is observed for the textured substrates, which may be attributed to the surface texture.

When light irradiates onto the textured surface, the optical path length of the light exceeds the physical thickness of the material. This phenomenon is explained by the geometry illustrated in Figure 5.28, where it is evident that the measured material thickness is less than the effective optical path length. As the light travels through a longer path in the textured material, it interacts more extensively with the material, potentially generating more free carriers in this manner.

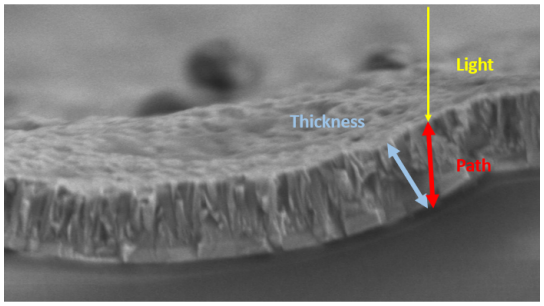

Figure 5.28: Difference between thickness and path of light in textured surface

However, the bilayers deposited on textured substrates still exhibit improved performance compared to single layers. The results for textured bilayers cluster in a more favorable region, further emphasizing the superior performance of the bilayer configurations.

6

Conclusions and Recommendations

This Chapter has been divided into two sections. Section 6.1 summarises the main outcomes obtained through the analysis of the experimental data. The effect of the deposition parameters while trying to achieve the best performing single layers are stated in 6.1.1. The effect of a bilayer configuration is presented in 6.1.2 where the results linked to textured surfaces are provided in 6.1.3. Section 6.2 provides recommendations on how the single layers can be further optimised. Then, further suggestions about enhancing the performance of bilayers deposited in texture glass in order to overcome challenges related to the higher absorption due to free carriers are provided.

6.1. Conclusions

6.1.1. Single layers

Both ICO and IOH materials demonstrate high electrical performance, indicating their suitability as conductive layers. SnOx, on the other hand, provides a good trade-off between optical and electrical properties, with its superior optical characteristics making it an appropriate candidate for the transparent layer.

In ICO, the experimental process involved varying both power and partial pressure. While higher power slightly improved the optical performance in the as-deposited samples, lower power levels resulted in a more significant enhancement in mobility, particularly after PDA treatment. This suggests that the optimal trade-off is achieved at lower power. The improvement in electrical properties at lower power is attributed to reduced sputtering damage during film formation, as higher power increases collisions in the plasma, leading to a decrease in mobility. Higher process pressure led to thinner films, requiring adjustments in the deposition rate. Process pressure did not significantly affect the optical properties. The lack of a clear trend in mobility and free carrier concentration suggests that further investigation is required.

In IOH, the experimental process involved varying both power and partial water pressure. Lower power levels enhanced the optical performance, particularly with increased gain in the UV region. The effect on the electrical properties was minimal, indicating that the lower power setting of 150 W produced the best overall samples. PDA treatment significantly increased the energy bandgap by 0.2 to 0.3 eV, while also enhancing mobility and reducing the free carriers concentration. This underscores the importance of PDA, as it improves the crystallinity of the material, leading to these enhanced properties. Partial water pressure had no measurable impact on the optical or electrical performance, as similar values were obtained across the range of conditions tested.

In SnOx, the experimental process involved varying both power and the gas mixture used during deposition. Depositions using gas mixtures containing oxygen yielded significantly better results, with a higher gain observed in the UV region and an increased bandgap. Additionally, the electrical properties, particularly mobility, were enhanced. This improvement is attributed to better stoichiometry in the SnOx films and a reduction in oxygen vacancies. However, the oxygen flow rate must be carefully

optimized, as excessively high oxygen flow leads to poorer results. Therefore, a combination of pure argon and argon-oxygen gases is recommended. Lower power levels produced superior optical and electrical performance, with the best results observed at a power of 130 W. PDA treatment did not lead to further improvements, as the material is already in a crystalline state.

6.1.2. Bilayers

All bilayer configurations outperformed single layers by combining the best attributes of both the transparent and conductive materials. Despite the greater thickness of the bilayers, the average transmittance values remained similar, highlighting the significant impact of reduced free carrier concentration. This reduction led to a marked absorption decrease in the NIR spectrum.

In terms of electrical properties, the mobility values were in the same range or even higher than those of the conductive materials (ICO and IOH), suggesting that free carriers in bilayers can bypass the grain boundaries of the transparent layer. This occurs as electrons utilize the interface between the layers to avoid obstacles.

Experiments with varying ICO thickness in the ICO/i-ZnO configuration underscored the importance of adequate conductive layer thickness. When the ICO thickness was lower, mobility values matched those of the conductive layer, but as thickness increased, mobility improved further. This indicates that with sufficient thickness, electron movement can exceed the limitations of even the conductive material.

On flat glass substrates, transmittance fluctuations are more pronounced due to constructive and destructive interference at the interface between the two materials. When SnOx is used, these fluctuations decrease, likely due to its higher surface roughness compared to i-ZnO.

Achieving the desired thickness in the bilayer configurations proved challenging, indicating that further investigation into the deposition process would be beneficial.

6.1.3. Textured surfaces

On textured substrates, the good electrical properties observed on flat substrates were maintained. However, an increase in free carriers concentration led to higher NIR absorption. The shape of the textured surface causes the optical path to exceed the layer thickness, increasing light-material interactions and, consequently, the number of free carriers. Despite this, the trade-off between optical and electrical characteristics remained superior to single layers, highlighting the potential of bilayers to significantly enhance solar cell performance.

On textured surfaces, the transmittance fluctuations were almost removed compared to flat glass substrates. This indicates that indeed texturing improved the light management along the wavelength since the reduced interference improved the overall transmittance.

6.2. Recommendations

The PDA method for ICO single layers could benefit from further optimization. XRD measurements indicated that the crystallinity of the material improved with this method, but the intensity was not as high as in SnOx, suggesting room for enhancement. Investigating the effect of temperature in the PDA treatment, rather than just time, could lead to further improvements in crystallinity.

Bilayers containing SnOx outperformed all other bilayer configurations in the as-deposited condition outperformed all other bilayer configurations. However, further optimization of those bilayers is necessary. The post-deposition annealing treatment has not been effective, as it led to a reduction in the electrical performance. Adjusting the PDA treatment, particularly the annealing time, may enhance the electrical properties and improve the overall performance of these layers.

All bilayers containing i-ZnO exhibited lower than expected thickness, indicating the need for further optimization of the deposition rate. This deviation may be attributed to the fact that i-ZnO was deposited onto another material rather than glass, potentially causing interactions that result in different deposition rates. Therefore, further investigation into the deposition process when using alternative substrates is recommended.

It was evident that when the thickness of the conductive material was sufficient, the electrical proper-

ties of the TCO improved due to the interface effect. Investigating the optimal thickness for samples containing IOH could provide valuable insights into the ideal thickness for this material, as it may differ from the optimal thickness for ICO.

On textured surfaces, an increase in free carrier concentration was observed compared to flat glass substrates, likely due to the shape of the texture. Creating smoother craters in the texture could reduce the difference between the physical thickness and the optical path length. Additionally, using materials with higher roughness, such as SnOx, may provide a similar benefit in terms of improving the transmittance curve. The native rough surface of SnOx could further enhance the optical and electrical properties, making it a promising candidate for improving overall performance.

References

[1] H. Lee Core Writing Team and J. Romero (eds.) *Summary for Policymakers. In: Climate Change 2023: Synthesis Report. Contribution of Working Groups I, II and III to the Sixth Assessment Report of the Intergovernmental Panel on Climate Change*. Geneva, Switzerland: IPCC, 2023, pp. 1–34.

[2] International Energy Agency. *CO2 Emissions in 2022*. Accessed: 2024-07-01. 2023. URL: https://www.iea.org/reports/co2-emissions-in-2022.

[3] Solar Energy Industries Association. *Solar Technologies*. Accessed: 2024-07-01. 2024. URL: https://www.seia.org/initiatives/solar-technologies#:~:text=There%20are%20three%20primary%20technologies,(SHC)%20systems%2C%20which%20collect..

[4] M. Victoria et al. "Solar photovoltaics is ready to power a sustainable future". In: *Joule* 5 (2021), pp. 1041–1056.

[5] International Energy Agency. *Solar PV*. Accessed: 2024-07-01. 2024. URL: https://www.iea.org/energy-system/renewables/solar-pv.

[6] W. W. S. Philipps. *Photovoltaics Report*. Accessed: February 2023. 2023. URL: https://www.ise.fraunhofer.de/content/dam/ise/de/documents/publications/studies/Photovoltaics-Report.pdf.

[7] Longi. *Longi, Nov 2022 [online]*. [Online; accessed 10-July-2023]. Nov. 2022. URL: https://www.longi.com/en.

[8] HyETSolar. *Thin film composition*. [Online; accessed 10-July-2023]. 2023. URL: https://www.hyetsolar.com/Thin-Film-Solar/thin-film-composition/.

[9] H. Solar. *LCOE Hyet Solar: Hyet solar*. [Online; accessed 10-July-2023]. 2023. URL: https://www.hyetsolar.com/cost-effective/.

[10] H. Solar. *Energy efficient*. [Online; accessed 10-July-2023]. 2023. URL: https://www.hyetsolar.com/news/energy-efficient/.

[11] M. Boccard et al. "High-stable-efficiency tandem thin-film silicon solar cell with low-refractive-index silicon-oxide interlay". In: *IEEE Journal of Photovoltaics* 4 (2014), pp. 1368–1373.

[12] T. D. Lee and A. U. Ebong. "A review of thin film solar cell technologies and challenges". In: *Renewable and Sustainable Energy Reviews* 70 (2017), pp. 1286–1297.

[13] F. Saitta. *Flexible, lightweight, silicon-based triple junction solar cell development*. 2021.

[14] Hao Lin, Mingyang Yang, Xia Ru, et al. "Silicon heterojunction solar cells with up to 26.81% efficiency achieved by electrically optimized nanocrystalline-silicon hole contact layers". In: *Nature Energy* 8 (2023), pp. 789–799. DOI: 10.1038/s41560-023-01255-2.

[15] H. Tan. "Highly transparent modulated surface textured front electrodes for high-efficiency multijunction thin-film silicon solar cells". In: *Progress in Photovoltaics: Research and Applications* 23.8 (2015), pp. 949–963.

[16] S. Calnan and A.N. Tiwari. "High mobility transparent conducting oxides for thin film solar cells". In: *Thin Solid Films* 518.7 (2010), pp. 1839–1849. DOI: 10.1016/j.tsf.2009.09.044.

[17] J. Zhang et al. "Recent progress on the electronic structure, defect, and doping properties of Ga_2O_3". In: *APL Materials* 8.2 (2020), p. 020906. DOI: 10.1063/1.5135307.

[18] E. Fortunato et al. "Transparent conducting oxides for photovoltaics". In: *MRS Bulletin* 32 (2011), p. 242.

[19] Prashand Kalpoe. “Transparent conductive oxide bi-layer as front contact for multijunction thin film silicon photovoltaic cells”. MA thesis. Delft University of Technology, 2023. URL: https://repository.tudelft.nl/islandora/object/uuid:f487531b-685f-4f2a-b59e-cd66ae7082ed/datastream/OBJ/download.

[20] M. “M. stage transistor amplifiers”. In: *ECE255 Electronic Circuit Analysis and Design*. 2013. Chap. signal 1, p. 8.

[21] A. Smets et al. *Solar Energy: The physics and engineering of PV conversion technologies and systems*. Delft, Netherlands: Delft University of Technology, 2015.

[22] Rosario Raciti et al. “Optical bandgap of semiconductor nanostructures: methods for experimental data analysis”. In: *Journal of Applied Physics* 121.23 (2017).

[23] V. A. Johnson and K. Lark-Horovitz. “Transition from classical to quantum statistics in germanium semiconductors at low temperature”. In: *Physical Review* 71 (1947), p. 374.

[24] M. I. Hossain et al. “Optics of perovskite solar cell front contacts”. In: *ACS Applied Materials & Interfaces* 11 (2019), p. 14693.

[25] O. Kluth. “Texturierte Zinkoxidschichten für Silizium-Dünnschichtsolarzellen”. Ph.D. thesis. Germany: RWTH Aachen, Forschungszentrum Jülich, 2001.

[26] J. E. Medvedeva. “Combining optical transparency with electrical conductivity: Challenges and prospects”. In: *Transparent Electronics* 1 (2010).

[27] J. E. Medvedeva. “Combining optical transparency with electrical conductivity: Challenges and prospects”. In: *Transparent Electronics* 1 (2010).

[28] T. Koida, Y. Ueno, and H. Shibata. “In2O3-based transparent conducting oxide films with high electron mobility fabricated at low process temperatures”. In: *physica status solidi (a)* 215.1700506 (2018).

[29] B. Macco, H.C.M. Knoops, and W.M.M. Kessels. “Electron scattering and doping mechanisms in solid-phase-crystallized In_2O_3:H prepared by atomic layer deposition”. In: *ACS Applied Materials & Interfaces* 7 (2015), p. 16723.

[30] N. Preissler et al. “Electrical transport, electrothermal transport, and effective electron mass in single-crystalline In_2O_3 films”. In: *Physical Review B* 88 (2013), p. 085305.

[31] D. H. Zhang. “Applied physics A”. In: *Applied Physics A* 62 (1996), pp. 487–492.

[32] C. Han. “High-Mobility TCO-Based Contacting Schemes for c-Si Solar Cells”. Unpublished. 2022.

[33] T. Minami. “MRS bulletin”. In: *MRS Bulletin* 25.8 (2000), pp. 38–44.

[34] T. Pisarkiewicz, K. Zakrzewska, and E. Leja. “Scattering of charge carriers in transparent and conducting thin oxide films with a non-parabolic conduction band”. In: *Thin Solid Films* 174 (1989), pp. 217–223. ISSN: 0040-6090. DOI: https://doi.org/10.1016/0040-6090(89)90892-4. URL: https://www.sciencedirect.com/science/article/pii/0040609089908924.

[35] Author(s). “Grain boundaries in polycrystalline materials for energy applications”. In: *AIP Publishing* 11.1 (2024), p. 011308. URL: https://pubs.aip.org/aip/apr/article/11/1/011308/3253559/Grain-boundaries-in-polycrystalline-materials-for.

[36] S. Kim et al. “On determining the height of the potential barrier at grain boundaries in ion-conducting oxides”. In: *Physical Chemistry Chemical Physics* 18 (2016), pp. 3023–3031. DOI: 10.1039/C5CP06387F. URL: https://doi.org/10.1039/C5CP06387F.

[37] Tadatsugu Minami. “New n-Type Transparent Conducting Oxides”. In: *MRS Bulletin* 25.8 (2000), pp. 38–44. DOI: 10.1557/mrs2000.149.

[38] P Babál. “Doped nanocrystalline silicon oxide for use as (intermediate) reflecting layers in thin-film silicon solar cells”. In: (2014).

[39] K. Ellmer, A. Klein, and B. Rech. *Transparent conductive zinc oxide: basics and applications in thin film solar cells*. Vol. 104. Springer Science & Business Media, 2007, pp. 59–66, 187–194.

[40] Can Han et al. “Realizing the potential of RF-sputtered hydrogenated fluorine-doped indium oxide as an electrode material for ultrathin SiO x/poly-Si passivating contacts”. In: *ACS Applied Energy Materials* 3.9 (2020), pp. 8606–8618.

[41] Hiroyuki Fujiwara and Robert W Collins. *Spectroscopic ellipsometry for photovoltaics*. Vol. 1. Springer, 2018.

[42] RA Synowicki. “Suppression of backside reflections from transparent substrates”. In: *physica status solidi c* 5.5 (2008), pp. 1085–1088.

[43] Designua. *Visible Spectroscopy. Spectrophotometry. Molecular Analysis Using UV*. Stock vector - illustration of emissions, chemistry. Dec. 2020. URL: https://www.dreamstime.com/visible-spectroscopyspectrophotometry-molecular-analysis-using-uv-visible-spectroscopyspectrophotometry-molecular-analysis-using-image205382843.

[44] A. Varanasi. “Deposition of hydrogen-doped indium oxide thin films using atmospheric-pressure plasma-enhanced spatial atomic layer deposition”. In: (2017).

[45] Jeon-Hong Kang et al. “Development of a thickness meter for conductive thin films using four-point probe method”. In: *Journal of Electrical Engineering & Technology* 16 (2021), pp. 2265–2273.

[46] FM Smits. “Measurement of sheet resistivities with the four-point probe”. In: *Bell System Technical Journal* 37.3 (1958), pp. 711–718.

[47] *What is X-ray Diffraction Analysis (XRD) and How Does it Work?* Accessed: 2023-06-26. 2023. URL: https://www.twi-global.com/technical-knowledge/faqs/xray-diffraction#:~:text=X%2Dray%20diffraction%20analysis%20(XRD)%20is%20a%20technique%20used,leave%20the%20material%20%5B1%5D.

[48] S. Bradbury, B. J. Ford, and D. C. Joy. “Scanning Electron Microscope”. In: *Encyclopedia Britannica* (Feb. 2023). URL: https://www.britannica.com/technology/scanning-electron-microscope.

[49] Leonard Tutsch et al. “The sputter deposition of broadband transparent and highly conductive cerium and hydrogen co-doped indium oxide and its transfer to silicon heterojunction solar cells”. In: *Progress in Photovoltaics: Research and Applications* 29.7 (2021), pp. 835–845.

[50] Hairen Tan. “Materials and Light Management for High-Efficiency Thin-Film Silicon Solar Cells”. PhD thesis. Delft University of Technology, 2015. URL: http://resolver.tudelft.nl/uuid:03ae8b9c-6d4d-4653-8071-4b667f559e52.

[51] O. Bierwagen. “Indium oxide—a transparent, wide-band gap semiconductor for (opto)electronic applications”. In: *Semiconductor Science and Technology* 30.2 (2015), p. 024001.

[52] J Nicholas Alexander. *Development of Enhanced Window layers for CIGS Photovoltaic Devices*. State University of New York at Albany, 2016.

[53] F Kurdesau et al. “Comparative study of ITO layers deposited by DC and RF magnetron sputtering at room temperature”. In: *Journal of non-crystalline solids* 352.9-20 (2006), pp. 1466–1470.

[54] Krishanu Dey et al. “Superior optoelectrical properties of magnetron sputter-deposited cerium-doped indium oxide thin films for solar cell applications”. In: *Ceramics International* 47.2 (2021), pp. 1798–1806. ISSN: 0272-8842. DOI: https://doi.org/10.1016/j.ceramint.2020.09.006. URL: https://www.sciencedirect.com/science/article/pii/S0272884220327024.

[55] Shichong An et al. “Cerium-doped indium oxide transparent electrode for semi-transparent perovskite and perovskite/silicon tandem solar cells”. In: *Solar Energy* 196 (2020), pp. 409–418. ISSN: 0038-092X. DOI: https://doi.org/10.1016/j.solener.2019.12.040. URL: https://www.sciencedirect.com/science/article/pii/S0038092X1931254X.

[56] S Ishibashi et al. “Low resistivity indium–tin oxide transparent conductive films. I. Effect of introducing H2O gas or H2 gas during direct current magnetron sputtering”. In: *Journal of Vacuum Science & Technology A: Vacuum, Surfaces, and Films* 8.3 (1990), pp. 1399–1402.

[57] MARIA MEIRELES RIBEIRO MAGALHÃES. “OPTIMIZATION OF RF MAGNETRON SPUTTERING OF CERIUM-DOPED INDIUM OXIDE FOR SILICON HETEROJUNCTION SOLAR CELLS”. In: (2023).

[58] Jan Keller et al. “Direct comparison of atomic layer deposition and sputtering of In2O3: H used as transparent conductive oxide layer in CuIn1- xGaxSe2 thin film solar cells”. In: *Solar Energy Materials and Solar Cells* 157 (2016), pp. 757–764.

[59] Ümit Özgür et al. “A comprehensive review of ZnO materials and devices”. In: *Journal of applied physics* 98.4 (2005).

[60] Kyu Ung Sim et al. “Effects of dopant (Al, Ga, and In) on the characteristics of ZnO thin films prepared by RF magnetron sputtering system”. In: *Current Applied Physics* 10.3 (2010), S463–S467.

[61] B. Selin Tosun et al. “Sputter deposition of semicrystalline tin dioxide films”. In: *Thin Solid Films* 520.7 (2012), pp. 2554–2561. ISSN: 0040-6090. DOI: https://doi.org/10.1016/j.tsf.2011.10.169. URL: https://www.sciencedirect.com/science/article/pii/S0040609011019092.

[62] B Selin Tosun et al. “Sputter deposition of semicrystalline tin dioxide films”. In: *Thin Solid Films* 520.7 (2012), pp. 2554–2561.

[63] M.A Gubbins, Vincent Casey, and S.B Newcomb. “M.A. Gubbins, V. Casey, S.B. Newcomb, nanostructural characterisation of SnO2 thin films prepared by reactive RF magnetron sputtering of tin. Thin Solid Films 405, 270-275”. In: *Thin Solid Films* 405 (Feb. 2002), pp. 270–275. DOI: 10.1016/S0040-6090(01)01728-X.

[64] MA Gubbins, V Casey, and SB Newcomb. “Nanostructural characterisation of SnO2 thin films prepared by reactive rf magnetron sputtering of tin”. In: *Thin solid films* 405.1-2 (2002), pp. 270–275.

[65] TW Kim. “Dependence of the structural, the electrical, and the optical properties on the Ar/O2 flow rate ratios for SnO2 thin films grown on p-InSb (111) substrates”. In: *Materials research bulletin* 36.1-2 (2001), pp. 349–353.

[66] H. Tan et al. “Highly transparent modulated surface textured front electrodes for high-efficiency multijunction thin-film silicon solar cells”. In: *Progress in Photovoltaics: Research and Applications* 23.8 (Aug. 2015), pp. 949–963. DOI: 10.1002/pip.2639.

A

ITO single layer

	P [W]	T [°C]	time [sec]	p.p [mbar]	Argon flow [sccm]
ITO1	130	25	3000	0.02	45
ITO2	130	206	1500	0.02	45

Table A.1: Deposition parameters for temperature series of ITO.

B

ICO single layer

Sample Name	P [W]	T [°C]	d.r. [nm/sec]	t [nm]	Time [sec]	99%Ar [sccm]	p.p [mbar]
11A	60	25	0.02	100	5000	3	3e-3
11B	60	25	0.02	100	5000	3	3e-3
11C	60	25	0.02	100	5000	3	3e-3
12A	100	25	0.04	100	2500	3	3e-3
12B	100	25	0.04	100	2500	3	3e-3
12C	100	25	0.04	100	2500	3	3e-3
13A	150	25	0.065	100	1538	3	3e-3
13B	150	25	0.065	100	1538	3	3e-3
13C	150	25	0.065	100	1538	3	3e-3
14A	200	25	0.095	100	1053	3	3e-3
14B	200	25	0.095	100	1053	3	3e-3
14C	200	25	0.095	100	1053	3	3e-3

Table B.1: Deposition parameters for power series experiment of ICO

Sample	P [W]	T [°C]	d.r. [nm/sec]	t [nm]	Time [sec]	99%Ar [sccm]	p.p [mbar]
F1	60	25	0.0170	100	5882	3	3e-3
F2	60	25	0.0170	100	5882	3	3e-3
F3	60	25	0.0170	100	5882	3	4e-3
F4	60	25	0.0170	100	5882	3	4e-3
F5	60	25	0.0170	100	5882	3	5e-3
F6	60	25	0.0170	100	5882	3	5e-3
F7	60	25	0.0170	100	5882	3	6e-3
F8	60	25	0.0170	100	5882	3	6e-3

Table B.2: Deposition parameters of ICO samples for process pressure series experiment

Power [W]	d. rate [nm/sec]
60	0.02
100	0.04
150	0.065
200	0.095

Table B.3: Deposition rate vs power, assuming lineal relation y=ax+b

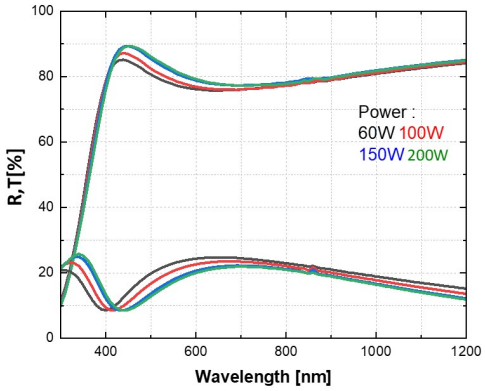

Figure B.1: Reflectance and transmittance of ICO samples at all power experimental series in as deposited conditions

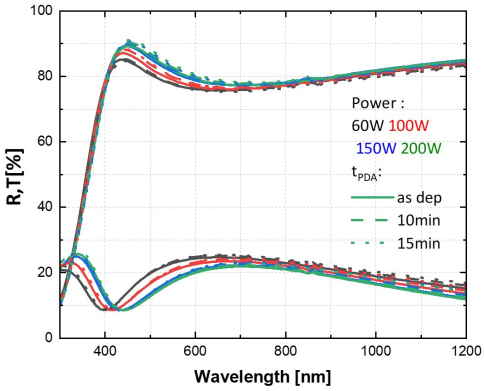

Figure B.2: Reflectance and transmittance of ICO samples at all power experimental series including with PDA treatment

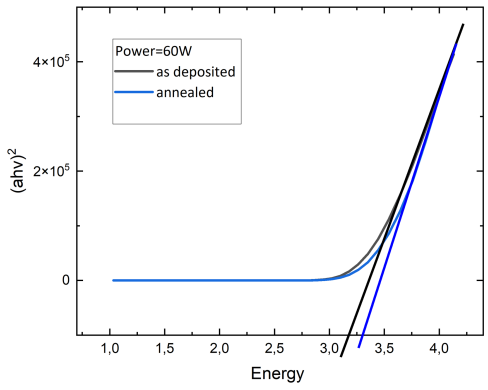

Figure B.3: Tauc plot of ICO samples deposited in 60W in as deposited and annealed conditions.

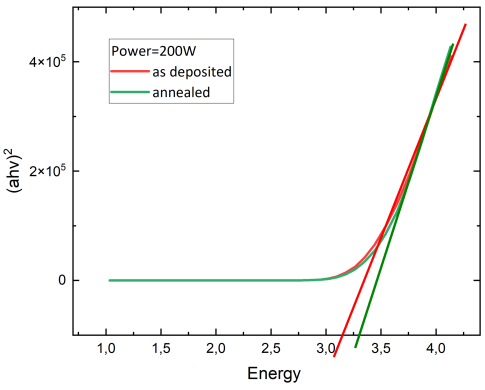

Figure B.4: Tauc plot for ICO samples deposited in 200W in as deposited and annealed conditions.

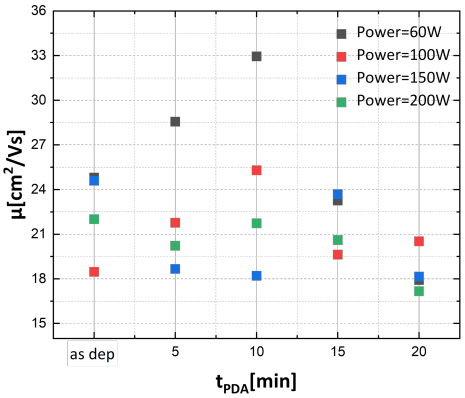

Figure B.5: Mobility vs PDA time of ICO samples at all power experimental series

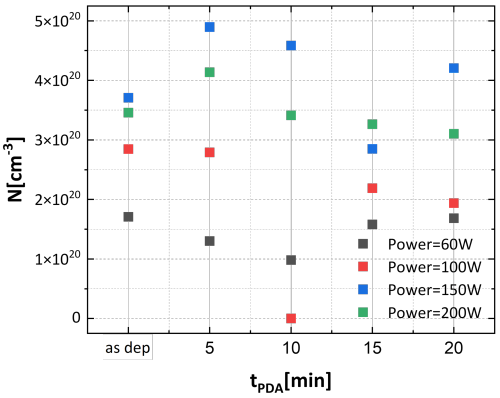

Figure B.6: Free carriers concentration vs PDA time of ICO samples at all power experimental series

C

IOH single layer

Sample name	P [W]	d.r. [nm/sec]	p.water [mbar]
17A	150	0.096	3e-5
18A	180	0.12	3e-5
19A	200	0.136	3e-5
20A	150	0.096	6e-5
21A	180	0.12	6e-5
22A	200	0.136	6e-5

Table C.1: Deposition parameters for IOH single layer samples. Additional sputtering conditions p.p = 5,7*10^{-3} mbar

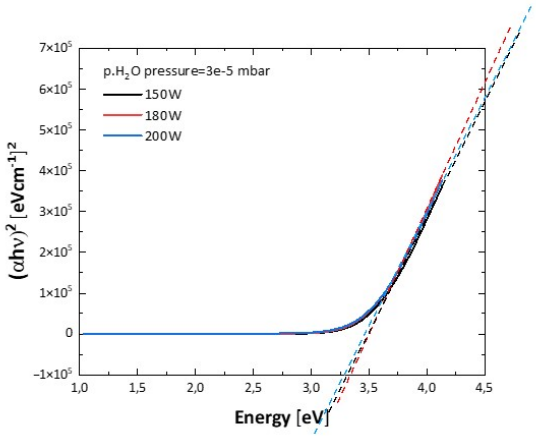

Figure C.1: Tauc plot of IOH samples for power experimental series in as deposited conditions, with p.water = 3*10^{-5} mbar in as deposited conditions

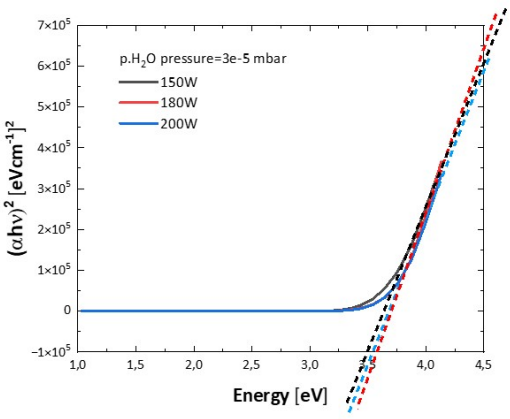

Figure C.2: Tauc plot of IOH samples for power experimental series in annealed conditions, with p.water = 3*10^{-5} mbar

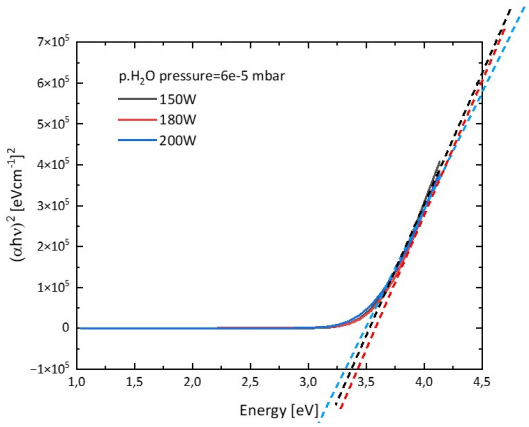

Figure C.3: Tauc plot of IOH samples for power experimental series in as deposited conditions, with p.water = 6*10^{-5} mbar

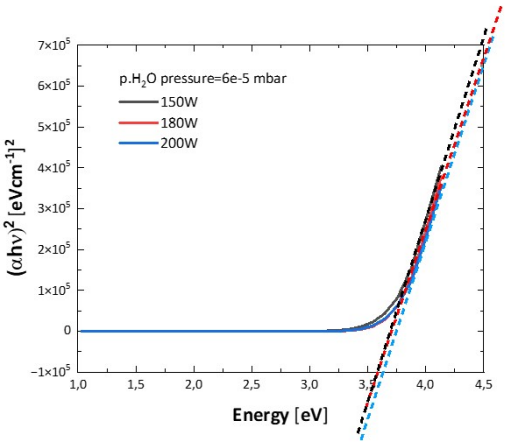

Figure C.4: Tauc plot of IOH samples for power experimental series in annealed conditions, with p.water = 6*10^{-5} mbar

D

SnOx single layer

Sample name	P [W]	T [°C]	d.r. [nm/sec]	t [nm]	Time [sec]	p.p [mbar]
A17	100	200	0.03	500	16667	2.6e-3
A19	100	400	0.03	500	16667	2.6e-3
A21	130	200	0.055	500	9091	2.6e-3
A23	130	400	0.055	500	9091	2.6e-3
A1	150	200	0.12	500	4167	2.6e-3
A3	150	400	0.12	500	4167	2.6e-3
A5	180	200	0.14	500	3571	2.6e-3
A7	180	400	0.14	500	3571	2.6e-3
A9	200	200	0.15	500	3333	2.6e-3
A11	200	400	0.15	500	3333	2.6e-3
A13	250	200	0.18	500	2778	2.6e-3
A15	250	400	0.18	500	2778	2.6e-3

Table D.1: Deposition parameters for SnOx power experimental series

Sample	P [W]	T [°C]	d.r. [nm/sec]	t [nm]	p.p [mbar]	Former gas	sccm
A25/26	130	400	0.06	500	2.6e-3	99% Ar	20
A27/28	150	400	0.08	500	2.6e-3	99% Ar	20
A29/30	170	400	0.10	500	2.6e-3	99% Ar	20
A31/32	130	400	0.06	500	2.6e-3	Ar - O_2	20
A33/34	150	400	0.08	500	2.6e-3	Ar - O_2	20
A35/36	170	400	0.10	500	2.6e-3	Ar - O_2	20
A37/38	130	400	0.06	500	2.6e-3	99% Ar / Ar - O_2	10 \10
A39/40	150	400	0.08	500	2.6e-3	99% Ar / Ar - O_2	10 \10
A41/42	170	400	0.10	500	2.6e-3	99% Ar / Ar - O_2	10 \10

Table D.2: Deposition parameters for SnOx power and gas series experiment

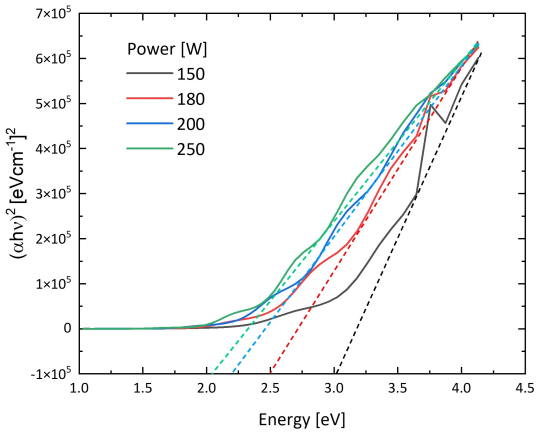

Figure D.1: Tauc plots of SnOx samples for power experimental series at 200°C deposition temperature

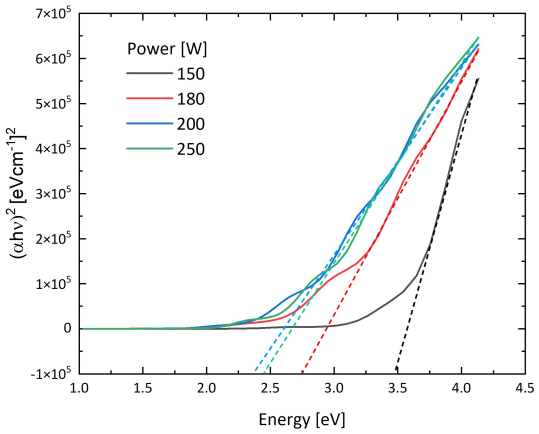

Figure D.2: Tauc plots of SnOx samples for power experimental series at 400°C deposition temperature

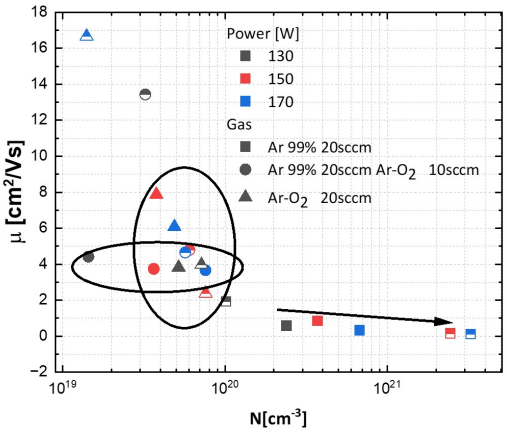

Figure D.3: Energy Bandgap of SnOx samples deposited at 130 W using different gasses

E

Bilayers

Sample name	P [W]	T [°C]	Expected t [nm]	99%Ar [sccm]	p.p[mbar]
ICO					
1A	60	25	50	3	3e-3
1C	60	25	50	3	3e-3
2A	60	25	100	3	3e-3
2C	60	25	100	3	3e-3
3A	60	25	150	3	3e-3
3C	60	25	150	3	3e-3
i-ZnO					
1A	60	200	1000	-	2.6e-3
1C	60	400	1000	-	2.6e-3
2A	60	200	1000	-	2.6e-3
2C	60	400	1000	-	2.6e-3
3A	60	200	1000	-	2.6e-3
3C	60	400	1000	-	2.6e-3

Table E.1: Deposition parameters for ICO/i-ZnO bilayers samples in flat glass substrates.

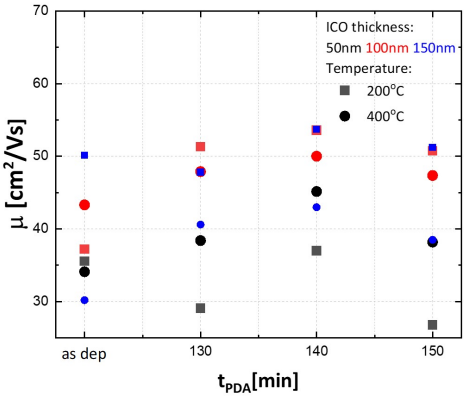

Figure E.1: mobility vs PDA time of ICO/i-ZnO bilayer with different thicknesses of ICO and different d.temperatures of i-ZnO. Depositions have been made in flat glass substrates.

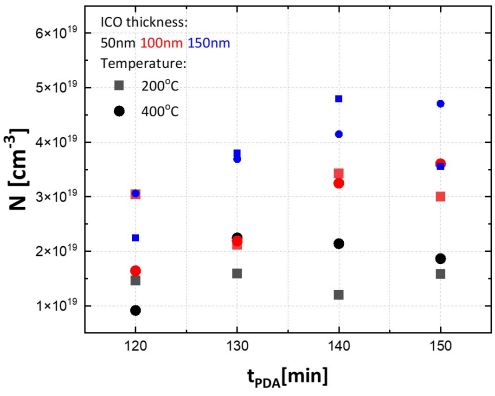

Figure E.2: free carriers vs PDA time of ICO/i-ZnO bilayer with different thicknesses of ICO and different d.temperatures of i-ZnO. Depositions have been made in flat glass substrates.

Sample Name	P [W]	T [°C]	Expected t [nm]	p.p [mbar]	p.water [mbar]
IOH					
17B	150	25	100	5.7e-3	3e-5
17C	150	25	100	5.7e-3	3e-5
20B	150	25	100	5.7e-3	6e-5
20C	150	25	100	5.7e-3	6e-5
i-ZnO					
17B	200	200	1000	2.6e-3	-
17C	200	400	1000	2.6e-3	-
20B	200	200	1000	2.6e-3	-
20C	200	400	1000	2.6e-3	-

Table E.2: Deposition parameters for IOH/i-ZnO bilayers in flat glass substrates

Sample	P [W]	T [°C]	Expected t [nm]	p.p [mbar]	p. water [mbar]
IOH					
J1	150	25	150	5.7e-3	3e-5
J3	150	25	150	5.7e-3	3e-5
ZnO					
J1	200	400	750	2.6e-3	-
J3	200	200	750	2.6e-3	-

Table E.3: Deposition parameters for IOH/i-ZnO bilayer in textured glass substrate.